The Numerical and Experimental Study of the Aeroacoustic Noise of Motor Vehicle Alternators

A thesis submitted in fulfilment of the requirements for the degree of Doctor of Philosophy

Matthew Wasko
B.Eng & B.Bus

School of Aerospace, Mechanical & Manufacturing Engineering
College of Science, Engineering and Health
RMIT University
November 2009

Declaration

I hereby declare that the work presented herein is my own, except where due reference and/or acknowledgement is made, with regard to both content in addition to editorial work. The work has not been submitted previously, in whole or in part, to qualify for any other academic reward. The content of this thesis comprises of work carried out since the official commencement date of the approved research program. Ethics procedures and guidelines have been followed throughout.

Matthew Wasko
School of Aerospace, Mechanical and Manufacturing Engineering

Acknowledgements

The work contained within the following pages would not have been possible without the much appreciated assistance and support of colleagues, friends and family. It is with these words that I would like to express my gratitude.

Firstly, to Professor Abanteriba, Michael Fischer, Martin Fischer and Hans-Joachim Lutz for making this project a reality. In doing so, a collaboration between the corporate research centre and alternator development at Robert Bosch GmbH was sparked that acknowledged the importance of aerodynamic noise in the development of motor vehicle alternators. It is my sincere hope that the work within these pages reflects this importance and supports future developments, which I am pleased to be currently a part of. The continual support of Martin Fischer throughout this work, acting as both supervisor and mentor, deserves many thanks.

I would also like to thank those colleagues which together provided both useful advice, in addition to much appreciated technical dialogue on acoustics and fluid dynamics. To only name a few, these include Marco Zucchini, Andre Gerlach and Siegbert Götz.

Also, my appreciation to the two students that worked under my supervision. Felix Bensing, for his patient help on mesh construction and programming, and Raja Sekhar Aduri, whose thesis project formed the basis of the Finite Element Method studies carried out within this work.

And finally, my sincerest thanks to my family, who in spite of the thousands of kilometres distance, supported me without fail, and to Angela Miller, for her patience and support during the last months of this work.

Contents

1 Introduction **2**

1.1 Motivation . . . 2
1.2 The alternator . . . 3
1.3 Aeroacoustics: a brief introduction . . . 4
1.4 Scope and objectives . . . 6
1.5 The geometry . . . 6
1.6 Structure of work . . . 7

2 Theory **9**

2.1 The homogeneous wave equation . . . 9
2.2 The aeroacoustic analogies . . . 12
2.3 Fan noise . . . 15
2.4 Lowson's formulation for rotating sources . . . 16
2.5 Case studies . . . 18
2.6 Summary . . . 20

3 Implementation of Lowson's theory **21**

3.1 Procedure and algorithm . . . 21
3.2 The half dipole approximation . . . 22
3.3 Implementation of an infinite, reflective plane . . . 25
3.4 Validation using a single stationary dipole source . . . 25
3.5 The effect of forcing on radial, tangential and axial sources . . . 25
3.6 Summary . . . 28

4 Experimental results **29**

4.1 Experimental setup . . . 29
4.2 Temperature and pressure correction . . . 32
4.3 Calculation of sound power level from microphone pressure data . . . 32
4.4 Repeatability of experimental results . . . 33
4.5 The A-weighting . . . 33
4.6 DIN/ISO 10 microphone sound power tests . . . 34
4.7 9 microphone sound pressure tests . . . 44
4.8 Summary . . . 52

5 Numerical results and experimental validation **53**

5.1 CFD simulation details . . . 53
5.2 CFD results and noise generation mechanisms . . . 57
5.3 Aeroacoustic results using Lowson's theory . . . 64

5.4 Experimental and numerical comparison 71
5.5 Asymmetrical influences of the reflective plate on sound propagation 77
5.6 Full model simulation in product development 78
5.7 Summary 80

6 Casing effects on sound propagation **82**
6.1 Boundary element methods 82
6.2 Finite element methods 86
6.3 Summary 102

7 Conclusions and recommendations **105**

List of Figures

1.1 Typical alternator assembly . . . 3
1.2 Simplified alternator . . . 7

2.1 Fundamental acoustic sources and their sound propagation in a free-field . . . 13
2.2 Relationship between the noise generated from steady and unsteady loading for the case of a typical alternator geometry . . . 18

3.1 Flow chart of CFD and acoustic calculation algorithm . . . 23
3.2 Half dipole source modelling . . . 24
3.3 Reflected source modelling . . . 26
3.4 Dipole sound propagation normal to oscillation . . . 26
3.5 Influences of the forcing frequency on a system with twelve equally spaced sources fluctuating in varying directions. . . . 27

4.1 ISO test bench . . . 31
4.2 Nine microphone test bench . . . 31
4.3 Upstream shield and various rib designs. (A) Shield design without ribs, (B) square rib design, (C) rounded rib design and (D) aerofoil-type design . . . 34
4.4 Effect of ribs on sound propagation at 10,000 rpm . . . 35
4.5 Clawpole designs (A) smooth cylindrical surface, (B) simplified clawpole design, (C) clawpole design with leading edge root chamfer and trailing edge chamfer . . . 37
4.6 Effect of clawpoles on sound propagation at 10,000 rpm . . . 37
4.7 Speed ramp of clawpole geometry without chamfers and without fan . . . 38
4.8 Cross section of tested rib designs . . . 39
4.9 Speed ramp of various rib geometries and the effects on total sound power level and particular orders . . . 39
4.10 Effect of varying shield rotation on sound propagation at 10,000 rpm . . . 41
4.11 Effect of rib count on sound spectra . . . 42
4.12 Fan blades tested; backward sweeped, low airflow fan (left) and forward sweeped, high airflow fan (right). Rotational direction is anti-clockwise . . . 42
4.13 Effect of fan geometry on sound production at 10,000 rpm . . . 43
4.14 Determination of source dominance . . . 44
4.15 Effect of blade number at 10,000 rpm . . . 45
4.16 Effect of hole number on the sound generated at 10,000 rpm . . . 46
4.17 Closure of several casing holes to excite lower orders; configuration E . . . 47
4.18 Effect of closing a number of holes in varying patterns . . . 48
4.19 Effect of closure of all casing holes at 10,000 rpm . . . 50
4.20 Effect of partial closure of the clawpole surfaces . . . 51

5.1 CFD mesh and geometry of reference model . . . 54
5.2 Periodic boundary condition mapping the two rotational ends of the alternator (blue and green) . . . 55
5.3 Pressure changes on fan blades over time . . . 58
5.4 Local flow effects due to inlet obstruction . . . 59
5.5 Pressure distributions on clawpoles and fan blades . . . 60
5.6 Pressure changes on clawpoles over time . . . 61
5.7 Flow stagnation at casing holes . . . 62
5.8 Pressure fluctuations on the stationary and rotating surfaces . . . 63
5.9 Full transient result of reference geometry, two full rotations, with individual surface forces shown for each source . . . 64
5.10 Comparison of Lowsons solution for varying 1/4 CFD results . . . 65
5.11 Source distribution for the 1000 source case . . . 66
5.12 Effect of source refinement on acoustic results . . . 66
5.13 Effect of source increase, rear clawpoles included . . . 67
5.14 Influence of microphone count on total SPL spectra in the plane of rotation $r = 0.6m$ . . . 68
5.15 Influence of microphone count on total SPL spectra in the plane perpendicular to rotation $r = 0.6m$ . . . 69
5.16 Influence of microphone count on total SPL spectra in a spherical plane $r = 1m$ . . . 69
5.17 Comparison of blade forces for different meshes . . . 70
5.18 Comparison of mesh quality and influence on the individual fan forces . . . 70
5.19 Comparison of numeric and experimental results, reference geometry . . . 73
5.20 Extracted forces from the 14 source resolution . . . 74
5.21 Comparison of individual microphone sound pressure levels . . . 75
5.22 Comparison of numeric and experimental results, geometry without fan . . . 75
5.23 Extracted forces from the main sources of the no fan geometry . . . 76
5.24 Comparison of individual sound pressure levels . . . 77
5.25 Asymmetrical sound propagation; 9 microphone configuration results . . . 78
5.26 Detailed plane analysis of asymmetrical sound propagation effects . . . 79
5.27 Comparison of numerical (dashed line) and experimental (solid line) results of a real alternator product . . . 80

6.1 Grid used as interface between Lowson's solution and BEM input . . . 85
6.2 BEM solution using a pressure boundary condition as the coupling surface . . . 86
6.3 BEM solution using a velocity boundary condition as the coupling surface . . . 87
6.4 Model used for the two-equation set validation . . . 89
6.5 Comparison between one-set and two-set wave equation along line at $t = 2.75 \times 10^{-3}$ . . . 89
6.6 Comparison between one-set and two-set wave equation at point over time . . . 90
6.7 Comparison of the two-set wave equation to the analytical spatial pressure drop of the 2D and 3D wave equation. . . . 90
6.8 Two models used to test surface source boundary condition. Model (a), as a single source panel with hard wall at the right most of the domain and model (b), as a source at right with obstruction at left of the domain . . . 92
6.9 Source surface boundary condition using a sine pressure forcing . . . 93
6.10 Source surface boundary condition using a cosine pressure forcing . . . 94
6.11 Influence of hard wall boundary condition ($\frac{\partial p}{\partial n} = 0$) on sound propagation and reflection in the domain . . . 95

6.12 Influence of non-reflective boundary condition ($\frac{\partial p}{\partial t} + a_0 \frac{\partial p}{\partial n} = 0$) on sound propagation and reflection in the domain 96
6.13 Geometry used for validating the interface boundary condition 97
6.14 Pressure distribution from a wave in a coupled two-domain problem using a convection-type domain interface 98
6.15 Geometry used for the modelling of rotating fan blades and rotating clawpole surfaces, whereby the direction of rotation is anti-clockwise 99
6.16 Comparison of pressure distributions from the two fan-blade solutions at a single time-step 100
6.17 Comparison of pressure spectra of the fan-blade solution between the FEM solution and Lowson's code 101
6.18 Comparison of pressure distributions from the two clawpole solutions at a single time-step 101
6.19 Comparison of pressure spectra for the clawpole solution between the FEM solution and Lowson's code 102
6.20 Stator casing geometry 103
6.21 Comparison of pressure spectra with and without casing 103

List of Tables

4.1 Sound Pressure Level [dB(Pa^2]) of reference geometry on different days 33
4.2 Difference between the first two blade passing frequencies (12th and 24th order) with a change in upstream rib count 41
4.3 Influence of stator openings on the main clawpole order and sidebands; the order number is shown in brackets 46

5.1 Sound Pressure Level at the first 4 harmonics 71
5.2 Comparison of the 12th harmonic with loading considered identical on all blades 71

6.1 Model data for Neumann with surface pressure condition 92
6.2 Source boundary condition with surface pressure condition 92
6.3 Model data for test case A 95

Summary

The aeroacoustics of a simplified alternator are analysed within the framework of this thesis, with the objective being the development of a tool capable of numerically predicting aeroacoustic noise. Focus has been placed on tonal noise and only dipole, rotating noise sources have been modelled. Input for these dipole sources are calculated using instationary CFD computations using the SST turbulence model. The acoustic tool developed is based on Lowson's equation, derived from the Ffowcs-Williams and Hawkings equation. Modifications to the formulation are included in order to model the reflective plane present during measurements and to ensure that sound propagates solely away from source surfaces (a half-dipole propagation). Numerical results are compared with experimental measurements, and show discrepancies in total sound power level. This is due to the inability of the methods used to model broadband noise sources that produce energy between the main orders (harmonics) of the alternator. Determining the total energetic content of the sound orders numerically calculated and comparing this to the energetic content of the measured orders yielded positive results; sound power level results were within 2 dB(A) of measurement. Dominant frequencies/orders were calculated generally within an accuracy of 6 dB(A); issues with the periodic boundary conditions and the rotor/stator interface produced spurious fluctuations that, for one tested case, produced strong 8th order noise. The developed tool was used successfully in a real alternator model, and once again showed very promising results. Fan orders were calculated within very good accuracy, while clawpole orders showed too much energy at higher orders due to the simplified CFD modelling of the casing holes. Total sound power level was computed too low due, once again, to the lack of broadband noise computation. Total energy from the computed orders was however calculated well within the range of the measured samples. The modelling of the casing using the BEM LMS Sysnoise was not possible due to the inability within the software to specify both pressure gradient and pressure boundary conditions, however models simulated using the FEM tool COMSOL Multiphysics showed that the influence of the casing on most orders, with the exception of the 40th and those above the 60th, was low, in addition to a low effect on the total sound energy.

The Numerical and Experimental Study of the Aeroacoustic Noise of Motor Vehicle Alternators

A thesis submitted in fulfilment of the requirements for the degree of Doctor of Philosophy

Matthew Wasko
B.Eng & B.Bus

School of Aerospace, Mechanical & Manufacturing Engineering
College of Science, Engineering and Health
RMIT University
November 2009

Declaration

I hereby declare that the work presented herein is my own, except where due reference and/or acknowledgement is made, with regard to both content in addition to editorial work. The work has not been submitted previously, in whole or in part, to qualify for any other academic reward. The content of this thesis comprises of work carried out since the official commencement date of the approved research program. Ethics procedures and guidelines have been followed throughout.

Matthew Wasko
School of Aerospace, Mechanical and Manufacturing Engineering

Acknowledgements

The work contained within the following pages would not have been possible without the much appreciated assistance and support of colleagues, friends and family. It is with these words that I would like to express my gratitude.

Firstly, to Professor Abanteriba, Michael Fischer, Martin Fischer and Hans-Joachim Lutz for making this project a reality. In doing so, a collaboration between the corporate research centre and alternator development at Robert Bosch GmbH was sparked that acknowledged the importance of aerodynamic noise in the development of motor vehicle alternators. It is my sincere hope that the work within these pages reflects this importance and supports future developments, which I am pleased to be currently a part of. The continual support of Martin Fischer throughout this work, acting as both supervisor and mentor, deserves many thanks.

I would also like to thank those colleagues which together provided both useful advice, in addition to much appreciated technical dialogue on acoustics and fluid dynamics. To only name a few, these include Marco Zucchini, Andre Gerlach and Siegbert Götz.

Also, my appreciation to the two students that worked under my supervision. Felix Bensing, for his patient help on mesh construction and programming, and Raja Sekhar Aduri, whose thesis project formed the basis of the Finite Element Method studies carried out within this work.

And finally, my sincerest thanks to my family, who in spite of the thousands of kilometres distance, supported me without fail, and to Angela Miller, for her patience and support during the last months of this work.

Contents

1 Introduction **2**

1.1 Motivation . . . 2
1.2 The alternator . . . 3
1.3 Aeroacoustics: a brief introduction . . . 4
1.4 Scope and objectives . . . 6
1.5 The geometry . . . 6
1.6 Structure of work . . . 7

2 Theory **9**

2.1 The homogeneous wave equation . . . 9
2.2 The aeroacoustic analogies . . . 12
2.3 Fan noise . . . 15
2.4 Lowson's formulation for rotating sources . . . 16
2.5 Case studies . . . 18
2.6 Summary . . . 20

3 Implementation of Lowson's theory **21**

3.1 Procedure and algorithm . . . 21
3.2 The half dipole approximation . . . 22
3.3 Implementation of an infinite, reflective plane . . . 25
3.4 Validation using a single stationary dipole source . . . 25
3.5 The effect of forcing on radial, tangential and axial sources . . . 25
3.6 Summary . . . 28

4 Experimental results **29**

4.1 Experimental setup . . . 29
4.2 Temperature and pressure correction . . . 32
4.3 Calculation of sound power level from microphone pressure data . . . 32
4.4 Repeatability of experimental results . . . 33
4.5 The A-weighting . . . 33
4.6 DIN/ISO 10 microphone sound power tests . . . 34
4.7 9 microphone sound pressure tests . . . 44
4.8 Summary . . . 52

5 Numerical results and experimental validation **53**

5.1 CFD simulation details . . . 53
5.2 CFD results and noise generation mechanisms . . . 57
5.3 Aeroacoustic results using Lowson's theory . . . 64

5.4 Experimental and numerical comparison 71
5.5 Asymmetrical influences of the reflective plate on sound propagation 77
5.6 Full model simulation in product development 78
5.7 Summary 80

6 Casing effects on sound propagation **82**
6.1 Boundary element methods 82
6.2 Finite element methods 86
6.3 Summary 102

7 Conclusions and recommendations **105**

List of Figures

1.1 Typical alternator assembly . . . 3
1.2 Simplified alternator . . . 7

2.1 Fundamental acoustic sources and their sound propagation in a free-field . . . 13
2.2 Relationship between the noise generated from steady and unsteady loading for the case of a typical alternator geometry . . . 18

3.1 Flow chart of CFD and acoustic calculation algorithm . . . 23
3.2 Half dipole source modelling . . . 24
3.3 Reflected source modelling . . . 26
3.4 Dipole sound propagation normal to oscillation . . . 26
3.5 Influences of the forcing frequency on a system with twelve equally spaced sources fluctuating in varying directions. . . . 27

4.1 ISO test bench . . . 31
4.2 Nine microphone test bench . . . 31
4.3 Upstream shield and various rib designs. (A) Shield design without ribs, (B) square rib design, (C) rounded rib design and (D) aerofoil-type design . . . 34
4.4 Effect of ribs on sound propagation at 10,000 rpm . . . 35
4.5 Clawpole designs (A) smooth cylindrical surface, (B) simplified clawpole design, (C) clawpole design with leading edge root chamfer and trailing edge chamfer . . . 37
4.6 Effect of clawpoles on sound propagation at 10,000 rpm . . . 37
4.7 Speed ramp of clawpole geometry without chamfers and without fan . . . 38
4.8 Cross section of tested rib designs . . . 39
4.9 Speed ramp of various rib geometries and the effects on total sound power level and particular orders . . . 39
4.10 Effect of varying shield rotation on sound propagation at 10,000 rpm . . . 41
4.11 Effect of rib count on sound spectra . . . 42
4.12 Fan blades tested; backward sweeped, low airflow fan (left) and forward sweeped, high airflow fan (right). Rotational direction is anti-clockwise . . . 42
4.13 Effect of fan geometry on sound production at 10,000 rpm . . . 43
4.14 Determination of source dominance . . . 44
4.15 Effect of blade number at 10,000 rpm . . . 45
4.16 Effect of hole number on the sound generated at 10,000 rpm . . . 46
4.17 Closure of several casing holes to excite lower orders; configuration E . . . 47
4.18 Effect of closing a number of holes in varying patterns . . . 48
4.19 Effect of closure of all casing holes at 10,000 rpm . . . 50
4.20 Effect of partial closure of the clawpole surfaces . . . 51

5.1 CFD mesh and geometry of reference model . . . 54
5.2 Periodic boundary condition mapping the two rotational ends of the alternator (blue and green) . . . 55
5.3 Pressure changes on fan blades over time . . . 58
5.4 Local flow effects due to inlet obstruction . . . 59
5.5 Pressure distributions on clawpoles and fan blades . . . 60
5.6 Pressure changes on clawpoles over time . . . 61
5.7 Flow stagnation at casing holes . . . 62
5.8 Pressure fluctuations on the stationary and rotating surfaces . . . 63
5.9 Full transient result of reference geometry, two full rotations, with individual surface forces shown for each source . . . 64
5.10 Comparison of Lowsons solution for varying 1/4 CFD results . . . 65
5.11 Source distribution for the 1000 source case . . . 66
5.12 Effect of source refinement on acoustic results . . . 66
5.13 Effect of source increase, rear clawpoles included . . . 67
5.14 Influence of microphone count on total SPL spectra in the plane of rotation $r = 0.6m$ . . . 68
5.15 Influence of microphone count on total SPL spectra in the plane perpendicular to rotation $r = 0.6m$ . . . 69
5.16 Influence of microphone count on total SPL spectra in a spherical plane $r = 1m$ . . . 69
5.17 Comparison of blade forces for different meshes . . . 70
5.18 Comparison of mesh quality and influence on the individual fan forces . . . 70
5.19 Comparison of numeric and experimental results, reference geometry . . . 73
5.20 Extracted forces from the 14 source resolution . . . 74
5.21 Comparison of individual microphone sound pressure levels . . . 75
5.22 Comparison of numeric and experimental results, geometry without fan . . . 75
5.23 Extracted forces from the main sources of the no fan geometry . . . 76
5.24 Comparison of individual sound pressure levels . . . 77
5.25 Asymmetrical sound propagation; 9 microphone configuration results . . . 78
5.26 Detailed plane analysis of asymmetrical sound propagation effects . . . 79
5.27 Comparison of numerical (dashed line) and experimental (solid line) results of a real alternator product . . . 80

6.1 Grid used as interface between Lowson's solution and BEM input . . . 85
6.2 BEM solution using a pressure boundary condition as the coupling surface . . . 86
6.3 BEM solution using a velocity boundary condition as the coupling surface . . . 87
6.4 Model used for the two-equation set validation . . . 89
6.5 Comparison between one-set and two-set wave equation along line at $t = 2.75 \times 10^{-3}$ . . . 89
6.6 Comparison between one-set and two-set wave equation at point over time . . . 90
6.7 Comparison of the two-set wave equation to the analytical spatial pressure drop of the 2D and 3D wave equation. . . . 90
6.8 Two models used to test surface source boundary condition. Model (a), as a single source panel with hard wall at the right most of the domain and model (b), as a source at right with obstruction at left of the domain . . . 92
6.9 Source surface boundary condition using a sine pressure forcing . . . 93
6.10 Source surface boundary condition using a cosine pressure forcing . . . 94
6.11 Influence of hard wall boundary condition ($\frac{\partial p}{\partial n} = 0$) on sound propagation and reflection in the domain . . . 95

6.12 Influence of non-reflective boundary condition ($\frac{\partial p}{\partial t} + a_0 \frac{\partial p}{\partial n} = 0$) on sound propagation and reflection in the domain 96
6.13 Geometry used for validating the interface boundary condition 97
6.14 Pressure distribution from a wave in a coupled two-domain problem using a convection-type domain interface 98
6.15 Geometry used for the modelling of rotating fan blades and rotating clawpole surfaces, whereby the direction of rotation is anti-clockwise 99
6.16 Comparison of pressure distributions from the two fan-blade solutions at a single time-step 100
6.17 Comparison of pressure spectra of the fan-blade solution between the FEM solution and Lowson's code 101
6.18 Comparison of pressure distributions from the two clawpole solutions at a single time-step 101
6.19 Comparison of pressure spectra for the clawpole solution between the FEM solution and Lowson's code 102
6.20 Stator casing geometry 103
6.21 Comparison of pressure spectra with and without casing 103

List of Tables

4.1 Sound Pressure Level [dB(Pa^2]) of reference geometry on different days 33
4.2 Difference between the first two blade passing frequencies (12th and 24th order) with a change in upstream rib count 41
4.3 Influence of stator openings on the main clawpole order and sidebands; the order number is shown in brackets 46

5.1 Sound Pressure Level at the first 4 harmonics 71
5.2 Comparison of the 12th harmonic with loading considered identical on all blades 71

6.1 Model data for Neumann with surface pressure condition 92
6.2 Source boundary condition with surface pressure condition 92
6.3 Model data for test case A 95

Summary

The aeroacoustics of a simplified alternator are analysed within the framework of this thesis, with the objective being the development of a tool capable of numerically predicting aeroacoustic noise. Focus has been placed on tonal noise and only dipole, rotating noise sources have been modelled. Input for these dipole sources are calculated using instationary CFD computations using the SST turbulence model. The acoustic tool developed is based on Lowson's equation, derived from the Ffowcs-Williams and Hawkings equation. Modifications to the formulation are included in order to model the reflective plane present during measurements and to ensure that sound propagates solely away from source surfaces (a half-dipole propagation). Numerical results are compared with experimental measurements, and show discrepancies in total sound power level. This is due to the inability of the methods used to model broadband noise sources that produce energy between the main orders (harmonics) of the alternator. Determining the total energetic content of the sound orders numerically calculated and comparing this to the energetic content of the measured orders yielded positive results; sound power level results were within 2 dB(A) of measurement. Dominant frequencies/orders were calculated generally within an accuracy of 6 dB(A); issues with the periodic boundary conditions and the rotor/stator interface produced spurious fluctuations that, for one tested case, produced strong 8th order noise. The developed tool was used successfully in a real alternator model, and once again showed very promising results. Fan orders were calculated within very good accuracy, while clawpole orders showed too much energy at higher orders due to the simplified CFD modelling of the casing holes. Total sound power level was computed too low due, once again, to the lack of broadband noise computation. Total energy from the computed orders was however calculated well within the range of the measured samples. The modelling of the casing using the BEM LMS Sysnoise was not possible due to the inability within the software to specify both pressure gradient and pressure boundary conditions, however models simulated using the FEM tool COMSOL Multiphysics showed that the influence of the casing on most orders, with the exception of the 40th and those above the 60th, was low, in addition to a low effect on the total sound energy.

Chapter 1

Introduction

The following sections introduce the work carried out in the scope of this research. The motivation of the work will initially be laid out, indicating the importance of the work from both a research, as well as practical, perspective. An introduction of the principles of alternator operation will be followed by an overview of the main noise generating mechanisms that exist. Finally, the structure of the work will be outlined.

1.1 Motivation

Sound, it's generation, it's propagation, and it's perception has become such an important factor in the design of products, products where sound is, at first, not the primary function, and secondly, generally an undesirable byproduct of the intended product function, that it has spawned it's own field; the NVH (Noise, Vibration and Harshness) field.

Reasons for this increasing importance can be traced to, but not restricted to, the following:

1. The introduction of legislative regulations in many industrial fields generally limits the allowable noise generation of machines. Although no such restrictions exist that are strictly applicable to alternators, the demands imposed by consistent reduction of the maximum allowable drive by noise from vehicles, such as the regulations outlined by the European Union [2, 12], yields subsequently the need to reduce the noise emitted from individual components of vehicles.

2. These legislative requirements impact OEMs (Original Equipment Manufacturers), such as Robert Bosch GmbH, through the stringent requirements placed by customers, in this case the automotive manufacturers. In the alternator industry, requirements from customers are far reaching, including at foremost, performance (electrical power delivery), efficiency (an increasingly important factor given the current climate debate), life time, cost, size, ability to operate in high temperatures and of course, the noise emissions of the alternator. These requirements are frequently conflicting; the need to deliver ever increasing electrical power to vehicles, due to increasing power requirements from modern vehicles, and the need to operate at high temperatures, due to the tendency of vehicle manufacturers to seal engine bays (generally for the purpose of reducing sound propagation from engines), yields the need to use large fans for the cooling of generators; a major byproduct being the production of aeroacoustic noise.

3. These stringent requirements imposed both by legislation, and in turn customers, drive the industry to develop alternators that satisfy the needs of customers; thus in turn driving competition in the market. The ability of a company to deliver a product that is competitive, both functionally

and from a cost perspective, can very much dictate the success of that company's product in the marketplace.

The need to address these concerns requires a sound knowledge of the physics that govern the primary functions of the generator (power delivery) in addition to secondary functions, both desired (such as cooling) and unwanted (e.g. noise). From this, the development cycle must include the ability to predict the severity of the unwanted function, perhaps optimising the system in order to avoid it, such that the influence of geometrical optimisation on the primary function is either positive or minimal.

The work herein focuses on only one of the secondary functions of alternators, noise, and in particular only a subset of that function: aerodynamically generated noise. In order to achieve an understanding of the underlying physics of aerodynamic noise, the development of techniques that may aid in the prediction of noise sources, in addition to the localisation of the sources of noise, has been carried out in this work. In achieving the goals of aerodynamic sound localisation and prediction, concerted efforts may consequently be applied in order to improve sound quality to levels that satisfy both the legislation, consumer demands in addition to offering a competitive advantage.

1.2 The alternator

Figure 1.1(a) illustrates the main components that constitute a conventional alternator design. The system consists of (a) the rotating pulley mechanism, (b) the stationary A-shield, (c) the rotating claw pole mechanism, (d) the A and B side fans, (e) the stator (shown also in greater detail in Figure 1.1(b)), (f) the B-side shield and (g) the electronics. It is convention in alternator development, and thus will be where necessary herein used, to name the pulley driven side of the alternator the A-side, the other side consisting of the electronics the B-side.

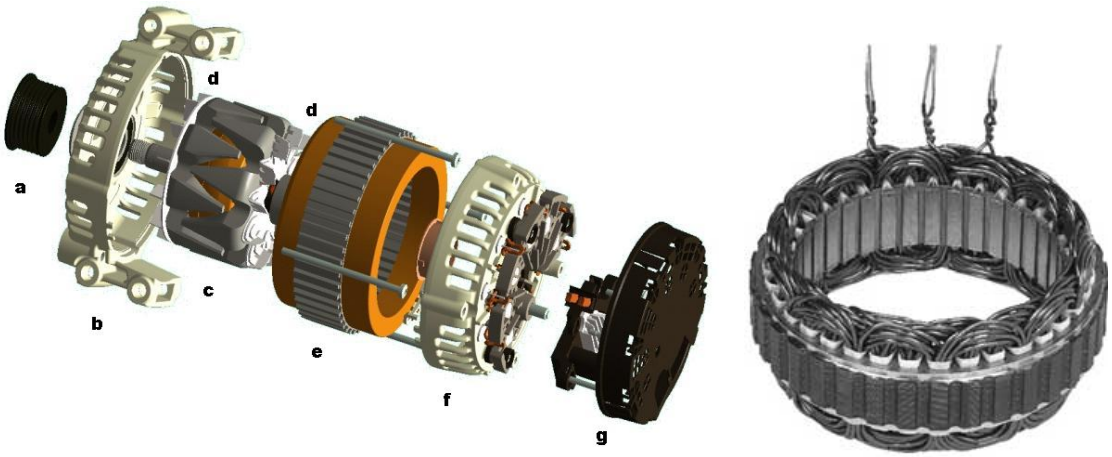

(a) Cut-away view of alternator components (b) Stator winding head [32]

Figure 1.1: Typical alternator assembly

The claw pole and fan blades undergo a rotating motion due to the rotation at the pulley, driven by the engine. The regulator, part of the electronics assembly, supplies current to the claw-shaped electromagnets within the rotor through the slip ring system. This produces a magnetic flux across the claw poles which, due to the rotating motion, has a certain relative speed with respect to the outer stator. The stator itself comprises of copper windings within an iron core. As there is a relative motion between the magnetic field and the copper windings, an electric current is induced in the copper windings. This current passes through a rectifier, also part of the electronics subsystem, which converts the generated alternating current into a useable direct current. The generation of an electric current produces heat in

both the copper windings and the electronic subsystem. In order to suppress heat build-up, a fan system is used to cool the internal components. The current generation of alternators use a twin fan assembly for this purpose, whereby fans are installed at both the A and B side of the claw poles (such alternators are commonly referred to as compact alternators).

There are two general sources of noise that can be directly attributed to modern alternators, these being the aerodynamically generated noise and the magnetically induced noise [11]. To a lesser degree, mechanical noise from bearings in addition to noise from the pulley can also occur; these noise sources however are generally of a much lower magnitude and generally occur during non-standard operation of the alternator or due to faults of the respective components. The aerodynamically generated noise is due to the time-instationary airflow in the system interacting with the structure, thus giving rise to sound-causing fluctuations in the flow-field.

Sources of aerodynamic sound in the alternator, as will be discussed in further detail in subsequent chapters, are generally those that induce an unsteadiness in the airflow within the system. In small industrial systems such as alternators, this unsteadiness is generally due to interactions occurring between rotating and stationary surfaces (rotor-stator interaction). Such interactions induce fluctuating pressures on surfaces which in turn produce noise. In systems where interactions between rotor and stator are not as significant, unsteadiness may arise due simply to boundary layer unsteadiness and the shedding of vortices. A large source of aerodynamically generated sound in alternators is due to the fan blades used to induce a cooling mass flow through the system. Not only does the fluid motion generated by the fan systems themselves induce flow interactions between the stator and rotor, but they induce a larger mass flow which generally increases the overall pressures and pressure fluctuations within the system. Common techniques used to optimise the induced noise include the use of asymmetric blade spacing, which prevents sound energy being focused at particular orders, in addition to careful forming of the blades in order to avoid regions that may be sensitive to rotor-stator interactions. Further techniques focus on modifications to the clawpole surfaces in order to reduce the interactions with the adjacent stator.

Magnetically generated noise stems from the magnetic fluxes generated at the claw poles. As the generated magnetic fields rotate in the system, they create fluctuating forces that act to vibrate the casing, in addition to initiating vibration of the rotor. The source of this magnetically induced noise, unlike aerodynamic noise, is more traditional with respect to the fundamental theories of acoustics; a vibrating structure induces pressures changes in the propagating medium (air) adjacent to the structure, which in turn induces a propagating wave. Contrast this to aerodynamically generated sound, which occurs due to pressure changes at the surfaces, and does not necessarily connote a structural vibration (unless the problem is an aeroelastic one). Influencing factors of the magnetically generated noise are far reaching due to it's structural nature: the connection of the alternator to the test bench/vehicle, the application of a torque from the pulley, the structural rigidity of the system as well as the configuration of the electrical subsystem all exert a considerable influence on magnetically induced structural noise and vibration. As such, measures are also far reaching, and may focus on the source itself by modifying the intensity of magnetic field fluctuations, or changing the structure in order to specifically design the operating conditions that lead to resonance, or the response of the system to forces.

1.3 Aeroacoustics: a brief introduction

The study of aeroacoustics and its prediction has been at the forefront of numerical research since the pioneering work of Lighthill [22, 23] in the 1960s. The studies were largely motivated by the growing concerns regarding the aerospace industry, in particular that of jet noise from aircraft engines. Only in recent years have technological advances given mathematicians and engineers the ability to numerically

solve the equations governing both fluid dynamics, in addition to the generation and propagation of sound. In most cases, accurate, comprehensive calculations have only been possible using fairly fundamental problems. The implementation of such sophisticated techniques to industrial problems has been limited.

The approach taken to solving the aeroacoustic numerical problem can be, in the broadest sense, defined into two categories. On the one hand, the solution of the compressible Navier Stokes equations leads to a solution of both the aerodynamic variables of interest in addition to the acoustic density and pressure fluctuations. On the other hand, solution of the incompressible Navier Stokes equations leads to a distinct separation of the acoustic and aerodynamic variables, given that the assumption of incompressibility removes the density fluctuations in the medium required for wave propagation. In this case, the solution to the aerodynamic problem yields variables which may be used as source terms in a separate acoustics calculation. The two approaches are respectively called the direct approach and the hybrid approach.

The direct approach has the attractive advantage of solving both the aerodynamic and acoustic problem in the one calculation. The advantage of this however is arguably only relevant for the simplest of problems. The fact that the acoustic pressure fluctuations are of a much lower order than the aerodynamic fluctuations can lead to the acoustic waves being damped out by numerical error; an issue which can be somewhat abated with the use of higher order numerics. Secondly, the domain for such an approach needs to extend to the observer location (the location of acoustic interest), unless variables from a near-field solution are propagated outwards by a second, linear solver. Such a domain is usually much greater than would otherwise be required for a purely fluid dynamic calculation; it extends further out than the region of aerodynamic interest. This naturally has an implication on the problem complexity and solution time. This is further compounded by the fact that the two physical problems have widely different characteristic length scales; whereas the aerodynamic problem has a wide range of scales, all the way to the smallest eddies, the acoustic problem length scales are generally much larger, dictated by the wave lengths of the sound of interest. At 20,000 Hz, the upper extreme of the audible range, wave lengths are no smaller than 1.7 cm, significantly larger than typical eddies at moderate Reynold's numbers, while at the lower extreme, 20 Hz, wavelengths are up to 17 meters in length. These scales are generally much larger than the size of typical alternators, which are up to 20 cm in diameter.

Conversely, taking a hybrid approach allows the procedures used to be tailored to the particular physics at hand. The fluid dynamics calculations can be carried out in a limited space using a mesh accurately resolved to capture the much finer scales prevalent in fluid dynamics (when compared to the acoustic scales). Physics that are only relevant to the aerodynamic problem need be calculated, valid assumptions such as incompressibility at low Mach numbers allowing a reduction in the number of equations being solved. The simplification of the aerodynamic problem becomes all the more important given that temporal-transients are required for acoustic calculations; compressible calculations over time require significant computational power. The use of the aerodynamic variables in a second, separate acoustic solver then allows prediction of the sound generation and propagation. The fact that several solvers are used somewhat increases the complexity of the problem, given that appropriate interfaces need to be designed. Furthermore, such hybrid methods restrict the coupling between the two solvers (for example, the inability of acoustic propagation to influence the aerodynamic solution). The ability of the solver also dictates how much of the physics remains intact. The inability of an acoustic analogy to model surface interactions such as diffraction and reflection yields a poor ability of modelling sound directivity well, while the inability of Boundary Element Methods to model multiple frames of reference does not allow the modelling of a stator/rotor acoustical coupling.

1.4 Scope and objectives

Sections 1.1 to 1.3 have indicated some of the factors to be considered throughout this work, and thus outline the important objectives which are to be achieved by this work. These key objectives are highlighted below.

1. The prediction of the far-field aeroacoustic noise generated by the operation of a motor vehicle alternator. Importance here is placed on the far-field noise prediction of the alternator, rather than near field, given that, as described in the motivation of the work, it is the far field acoustic properties of the alternator which are generally of interest in the industry. Focus will be placed on the tonal noise components produced by the system; tonal noise is generally considered to be the main source of annoyance in such systems, and thus it's importance in this work is stressed. Importance will also be placed on the prediction of total sound power levels, essentially the ability to determine the total sound energy generated by the system. The ability to predict accurately the directivity of the sound will also be analysed through sound power and pressure calculations at multiple microphones.

2. The use of numerical techniques capable of assessing the effect of geometrical variations. The ability to affect the strength of the sources through geometrical alternations, confirm the effect of these alterations in aerodynamic calculations and observe their effects on sound creation and propagation will ensure the techniques usefulness in product development.

3. The ability to physically understand the sound generating mechanisms, and in turn determine the location of predominant sound generating mechanisms. The techniques must be such that localisation of problem areas is possible.

4. The ability to apply the developed tools in the sound prediction and assessment of real products. Overly complex methods are to be avoided in favour of methods that offer a good turn-around time of results, while maintaining sufficient physical accuracy as to satisfy points 1 through to 3.

The work throughout is thus numerical in nature, with both semi-analytical in addition to numerical methods, such as CFD, FEM and BEM, used extensively. The third objective encroaches both the experimental and numerical domain. In this work, the purpose of experimental work will be two-fold. Firstly, as a validation method for the numerical work, and secondly to understand how geometrical variations to the system influence the sound generated, and to use the theory in a general sense as a tool to explain why certain phenomena occur. The reader will come to realise that the sheer amount of geometrical changes made during experimental investigations outweighs the geometries tested with numerical methods, due mainly to the complex nature of the three-dimensional models and mesh preparation in addition to computational time. However, the experimental study of all these geometrical variations yields nevertheless fruitful findings.

1.5 The geometry

The typical alternator geometry shown in Figure 1.1(a) is somewhat too complex for research purposes, in particular the complex details associated with the stator winding heads, shown in Figure 1.1(b). In simplifying the geometry for this thesis, the main sound generating mechanisms are considered that are relevant to alternator applications. From the stator side, these include the holes in the stator winding heads (Figure 1.1(b)), in addition to the upstream ribs of the castings. On the rotor side, a symmetrical 12 bladed fan geometry is modelled, in addition to 8 clawpole surfaces. In order to further reduce complexity, only one axial half of the alternator system is considered. The geometry is shown in Figure 1.2(a), with

the physical alternator shown on the test bench in Figure 1.2(b). Further details will be discussed in the experimental analysis, Section 4, in addition to the numerical results, Section 5. In addition to this model, henceforth called the reference model, geometrical modifications will also be analysed in subsequent sections in order to establish their influence on sound.

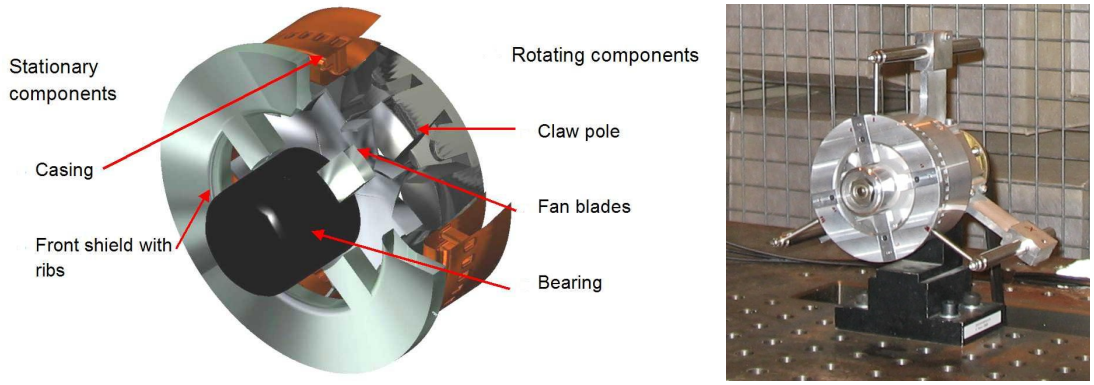

(a) Simplified alternator design

(b) Alternator on test bench

Figure 1.2: Simplified alternator

1.6 Structure of work

Firstly, fundamental theories of acoustics and aeroacoustics will be outlined in Section 2. The discussion of acoustic fundamentals in light of the applied aerodynamic subsets will highlight similarities between many of the theories, and describe the origins of some of the initial theories that have to this date been documented. Case studies will also be outlined in order to determine the relevance and practicality of the theories in the industry. This will highlight the multifaceted nature of this work; the use of fundamental models based on theory to develop tools for the calculation of sound propagation from aerodynamic sources, and the application of those tools in an industrial related problem. The case study section should thus outline which theories have been applied to various industrial problems, once a sound description of the theories has been laid out.

Section 3 will outline the implementation of Lowson's equation into the numerical chain, highlighting how the method is integrated, validated with simple sources, and several modifications carried out.

Section 4 will cover results from the experimental work. Although the work covered in this thesis is numerical in nature, a separate section is devoted to the analysis of experimental results which serve to validate the theoretical models. The experimental work has been carried out at two facilities: a facility custom built for alternator testing and satisfying ISO standards at the alternator development facility, in addition to a second test facility used at the corporate research centre.

Sections 5 and 6 will delve deeper into the tools developed and used, with particular focus on the acoustic tools, in addition to comparison to measurements. A detailed discussion of the CFD tool used, CFX, will not be carried out, given that it is a well documented tool in computational fluid dynamics. Having said this, discussion of the CFD models will be nevertheless carried out where necessary.

The tools that will be discussed in detail are the semi-analytic method from Lowson, Boundary Element Methods and Finite Element Methods. The dipole sources modelled using Lowson's formulation disregard the influence of surfaces on sound propagation, but provide nevertheless an efficient method of calculating source strength, and dependant on the frequencies of interest and the size of the system, propagation. BEM tools have the added advantage of modelling reflection from surfaces upstream of the sources, but are incapable of modelling moving sources. Finally, FEM tools have the potential of modelling

rotating and stationary surfaces, and their full interaction, at the cost of high resource demands, whereby full three-dimensional transient simulations were not carried out due to insufficient computational power. The need for transient modelling in order to model the system stems from the changing relative position between the rotor and stator.

Conclusions will be made based on the analysis conducted throughout the work. The ability of the semi-analytical and numerical methods in the prediction of aerodynamic sound from alternators will be discussed, as too their applicability in development. Suggestions for future work will be outlined at the conclusion of the work.

Chapter 2

Theory

The following section will outline the major theories in the field of aeroacoustics, branching off into more focused theories relevant to aeroacoustics of fan-type problems (rotating machines). Starting with a broad introduction into acoustics, theories from Lighthill and Ffowcs-Williams and Hawkings will be discussed, in addition to the specialised theories of Lowson. A general discussion on fan noise will also be carried out, which will justify the direction taken in the numerical procedure used, to be discussed in subsequent chapters.

2.1 The homogeneous wave equation

A short introduction to the classical wave equation is given in the following section. The inhomogenous wave equation is first derived, thereby giving the solution of the wave equation in a free field, free of source terms. Following this, a point source term is introduced into the fluid dynamics equation of momentum. Solution of the flow variables yields the fundamental solution for the wave equation, commonly known as the Green's solution. The fundamental solution is an important solution for the further derivation of methods based on the wave equation, including the Ffowcs-Williams Hawkings equation and subsequently Lowson's equation. In addition, it lays the groundwork for comprehensive numerical methods such as the Boundary Element Method in acoustics.

2.1.1 Derivation of the classical wave equation

The solution of the homogeneous wave equation begins with the formulation of the well known conservation of mass (Equation 2.1) and momentum equations (Equation 2.2, for each of the spatial i coordinates), where ρ is the acoustic density, $\mathbf{V} = (u_x, u_y, u_z)$ is the air particle velocity vector, p is a fluid pressure and τ_{ij} is a viscous shear stress tensor. Both forms shown below assume there is no injection of fluid (for the case of the conservation of mass equation) and that there are no external body forces (momentum equation). For a derivation of the governing fluid dynamics equations, the reader is referred to introductory fluid dynamics texts [39, 5].

$$\frac{\partial \rho}{\partial t} + \nabla . (\rho \mathbf{V}) = 0 \tag{2.1}$$

The conservation of momentum equation below is derived in the x, y and z coordinate directions.

$$\frac{\partial (\rho u_i)}{\partial t} + \nabla . (\rho u_i \mathbf{V}) = -\frac{\partial p}{\partial x_i} + \sum_{j=1}^{3} \frac{\partial \tau_{ij}}{\partial x_j} \tag{2.2}$$

The influence of viscosity on the propagating acoustic waves is often considered negligible. This is generally held true when the disturbances do not propagate over excessively large distances [17]. The viscous stress terms can thus be ignored, and, rewriting Equation 2.2 yields, where the ∂_i term denotes a spatial partial derivative in the corresponding direction, where $i = x, y, z$. This form of the momentum equation is commonly known as the Euler equations (Equation 2.3).

$$\frac{\partial (\rho v_i)}{\partial t} + \nabla . (\rho v_i \mathbf{V}) = -\frac{\partial p}{\partial x_i} \tag{2.3}$$

The formal derivation of the wave equation begins with the inherent assumption that the pressure and density perturbations are small perturbations to some ambient state [35]. Further, the medium is assumed to be both homogeneous as well as quiescent. A homogeneous medium is one where all ambient quantities are constant throughout space, while a quiescent medium is one where the ambient values are constant in time and the ambient velocity (the medium velocity) is at rest. The equations are thus linearised (e.g. $\phi = \phi_0 + \tilde{\phi}$), giving the linearised conservation of mass (Equation 2.4) and momentum equation (Equation 2.4), where zero subscripts denote the ambient quantities and the tilde values denote the perturbations.

$$\frac{\partial \tilde{\rho}}{\partial t} + \rho_0 \nabla . \tilde{\mathbf{V}} = 0 \tag{2.4}$$

$$\rho_0 \frac{\partial \tilde{\mathbf{V}}}{\partial t} = -\nabla \tilde{p} \tag{2.5}$$

Multiplying Equation 2.4 by $\frac{\partial}{\partial t}$ and Equation 2.5 by the gradient operator, ∇, and eliminating the velocity quantities yields Equation 2.6.

$$\frac{\partial^2 \tilde{\rho}}{\partial t^2} - \nabla^2 \tilde{p} = 0 \tag{2.6}$$

The equation of state dictates that the density of the medium is a function of the pressure in the medium, proportional to the speed of sound, a_0. Expanding the function using a Taylor series, and assuming that only first orders are significant (once again an assumption of linearity), one obtains the relationship in Equation 2.7.

$$\tilde{p} - p_0 = a_0^2 (\tilde{\rho} - \rho_0) \tag{2.7}$$

Substituting Equation 2.7 into 2.6 yields the classical wave equation (Equation 2.8) for sound in an inviscid, homogeneous and quiescent medium, void of any sources. In this instance, and from hereon in, the variable perturbations are written without a tilde for clarity. The variables being solved for in acoustics problems are seldom absolute values, but rather perturbations around an ambient constant.

$$\nabla^2 p - \frac{1}{a_0^2} \frac{\partial^2 p}{\partial t^2} = 0 \tag{2.8}$$

The form of the classical wave equation may be also solved in the frequency domain. Assuming that the pressure (or density) can be approximated by a harmonic, $p = \Re \left(p_n (\mathbf{x}) \exp^{i\omega t} \right)$, where $\mathbf{x}$ is the spatial coordinates, p_n the Fourier coefficients and ω the frequency, the Helmholtz equation (Equation 2.9) is formed for the solution of the Fourier coefficients at various wave numbers, $k = \frac{\omega}{a_0}$.

$$\nabla^2 p + k^2 p = 0 \tag{2.9}$$

2.1.2 The fundamental solution to the classical wave equation

The fundamental solution to the wave equation is obtained by solving the Green's function for the Helmholtz equation [43, 16]. The Green's function is essentially an integral kernel used to solve an inhomogenous partial differential equation [41]. The dependant variables are shown here to highlight that the variables, including the source term, are dependant on space and time, where G is the fundamental pressure solution. The unit impulse delta function implies that the source is only active at it's location, $\mathbf{y}$. The solution will show that it's effects are felt throughout the domain given the convective nature of the wave equation.

$$\nabla^2 G\left(\mathbf{x}-\mathbf{y}\right) + k^2 G\left(\mathbf{x}-\mathbf{y}\right) = \delta\left(\mathbf{x}-\mathbf{y}\right) \tag{2.10}$$

Letting r be the scalar distance between the source and observer and assuming that the source is located at the origin of a spherical coordinate system yields Equation 2.11. This equation assumes additionally that the fundamental solution is symmetrical; i.e. it only varies with respect to the radial direction, r. The equation and subsequent solution is valid everywhere except at the point source, where a singularity exists.

$$\frac{\mathrm{d}^2 G}{\mathrm{d}r^2} + \frac{2\mathrm{d}G}{r\mathrm{d}r} + k^2 G = 0 \tag{2.11}$$

It can be shown that a solution to this equation for a point source (that is, an outgoing wave) is as in Equation 2.12, where A is an arbitrary constant.

$$G = A\frac{\mathrm{e}^{-ikr}}{r} \tag{2.12}$$

The solution with the point source is determined by integrating the Helmholtz equation around a small volume surrounding the point source and letting the radius of the spherical volume, ϵ, approach zero, as shown in Equation 2.13. The integral of the dirac delta function at it's location is unity.

$$\lim_{\epsilon\to\infty}\int_{V_\epsilon}\left(\nabla^2 G + k^2 G\right)\mathrm{d}V = 1 \tag{2.13}$$

The limits of the integrals of the two terms are treated separately. The second term of the integral in Equation 2.13 is removed given that the volume integral goes to zero quicker than the Green's function goes to infinity. Application of the divergence theorem to the first term yields the solution in Equation 2.14, where n is the normal vector to the source.

$$\lim_{\epsilon\to\infty}\int_{V_\epsilon}\nabla^2 G\mathrm{d}V = \lim_{\epsilon\to\infty}\int_{V_\epsilon}\frac{\mathrm{d}G}{\mathrm{d}n}\mathrm{d}S = 1 \tag{2.14}$$

By substituting Equation 2.12 into 2.14, solving for A leads to the definition of the three dimensional Green's solution for sound propagation in a homogeneous, undisturbed medium, shown in Equation2.15.

$$G_{3D} = \frac{\mathrm{e}^{-ikr}}{4\pi r} \tag{2.15}$$

The solution of the 2D Green's solution follows a similar process whereby a point source is placed in a two-dimensional medium. For the 2D case, it is convenient to define the wave equation using polar coordinates. Whereas with the 3D solution an infinitesimal spherical volume was isolated and integrated around the source, for the 2D solution the integration takes place around the circumference of an infinitesimal circle positioned around the source, with limits dictating that once again it's radius,

ϵ, approaches zero. Full derivation of the solution is not presented here, as the 2D case has limited use in the scope of this work, however the reader is referred to [44] for derivations. The two-dimensional Green's function is given in Equation 2.16, where H is a Henkel function.

$$G_{2D} = \frac{\mathrm{i}}{4}\mathrm{H}_0^1\left(\frac{\omega r}{a_0}\right) \tag{2.16}$$

The derivation of the two and three-dimensional Green's functions paves the way for a discussion on the techniques used in modern acoustics and it's aerodynamically based subset. In particular, solution of the Ffowcs-Williams Hawkings equation and Lowson's equation, a technique heavily used throughout this work, has foundations set in the fundamental acoustical solutions. This too can be said of the Boundary Element Method technique, a commonly used technique in acoustics used to solve the Helmholtz equation for bounded and unbounded problems.

2.1.3 Sound propagation from the fundamental sources

The sound distribution of the source defined by Green's function, Equation 2.15, is inversely proportional to the distance to the observer, $\frac{1}{r}$. The shape of the time averaged pressure distribution is that typical of a monopole source, and appears as shown in Figure 2.1(a), with the source positioned in the middle of the numerical domain.

Further fundamental sources can be determined by observing the effects of monopole interactions. In Figure 2.1(b), by placing two monopoles with opposing phase next to one another (shown here as red and black sources), and ensuring that the distance between the two is much smaller compared to the wavelength of the emitting source, a typical dipole sound distribution ensues. The characteristic shape of the dipole source is a figure eight; perpendicular to the acting dipoles (in the y-direction), a maxima occurs, whereas parallel to the dipole (in the x-direction), the opposing phase of the emitted pressure from the two dipoles cancels causing a minima.

Similarly, the quadrupole distribution can be reproduced by using two dipoles (equivalent to four monopoles), once again 180 degrees out of phase. Two types of general distributions are possible, shown in Figures 2.1(c) to 2.1(d). The lateral quadrupole, similarly to the dipole distribution, shows strong regions of minima, in this case four. Four main lobes are noted acting in-line with sources that are in phase. The linear quadrupole on the other hand, bears at least in the far-field a resemblance to the dipole, the main difference being two weaker lobes acting in the x-direction.

2.2 The aeroacoustic analogies

The aeroacoustic analogies form a connection with the wave equation in that they offer source terms directly related to aerodynamic mechanics. The following section will highlight the major aeroacoustic analogies from Lighthill, Curle and Ffowcs-Williams and Hawkings. These analogies form the basis of the theory of Lowson, which describes the propagation of sound due to rotating sources, discussed in Section 2.4.

2.2.1 Lighthill's analogy on turbulence induced sound

The theory of Lighthill [22, 23] is derived analog to the wave equation in that the fundamental equations of aerodynamics, the momentum and the conservation of mass equations, are solved for an inviscid case. As with much of the acoustic analogies, a backward coupling of the aerodynamic-acoustic interactions is ignored. Essentially, this implies that the acoustic waves can have no affect on the aerodynamic flow

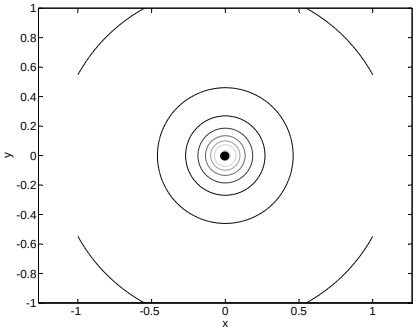

(a) Sound propagation of a monopole

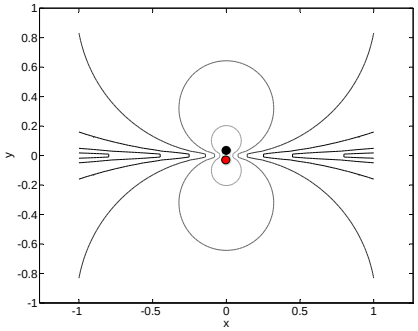

(b) Sound propagation of a dipole

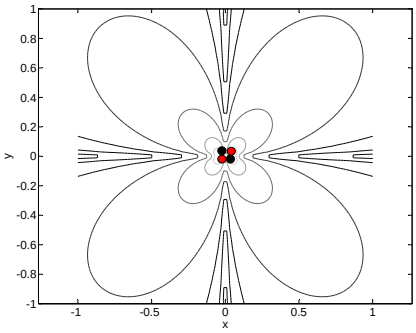

(c) Sound propagation of a lateral quadrupole

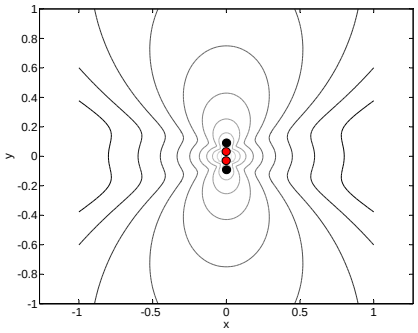

(d) Sound propagation of a linear quadrupole

Figure 2.1: Fundamental acoustic sources and their sound propagation in a free-field

field. This, notes Lighthill, is a fair assumption in flow fields devoid of a resonator given the significance of the energy difference between the aerodynamic flow field and the sound.

Lighthill proceeds by considering two separate regions; 1) the fluid source region containing the sound sources which is surrounded by 2) a large volume of fluid at rest, a propagating medium which itself consists of no sources. By comparing the sets of equations defining density fluctuations in the two regions, it is possible to solve an equivalent set of equations describing the outer, propagating medium, being acted upon by an external force field.

Lighthill's source terms are so derived by considering the stresses acting on a fluid in both the forced case and the unforced case, with the sum of the source terms being the difference between the two. With respect to the forced region, Lighthill considers the source terms to be the Reynolds Stress terms, $\rho u_i u_j$, and a set of real stresses, p_{ij}, both acting respectively in a shearing direction to an element and normal to it's surfaces. The uniform acoustic medium on the other hand undergoes stresses that are proportional to variations in it's density. This yields the Lighthill stress terms, shown in Equation 2.17.

$$T_{ij} = \rho v_i v_j + p_{ij} - a_0^2 \rho \delta_{ij} \tag{2.17}$$

Given that the term is a stress term, and the knowledge that a dipole represents the effects of a concentrated force (as will be discussed in Section 2.2.2), of which two equal and opposing forces can represent a stress, the stress term represents a quadrupole. This is analog to the field descriptions of the dipole and quadrupole sources discussed in Section 2.1.3. Here, Lighthill argues that in the presence of other noise sources such as those causing dipole and monopole like propagation, the quadrupole term becomes less important. This will be discussed in detail in Section 2.3.

Rewriting the continuity and momentum equations, and using the relation in Equation 2.17, Lighthill

produces the wave equation (analog to that shown in Section 2.1), with the Lighthill stress tensor used to define the quadrupole source, shown in Equation 2.18.

$$\frac{\partial^2 \rho}{\partial t^2} - a_0^2 \nabla^2 \rho = \frac{\partial^2 T_{ij}}{\partial x_i \partial x_j} \tag{2.18}$$

2.2.2 Sound influenced by solid boundaries

Curle [15] extended the work of Lighthill by considering the effects of solid surfaces on aerodynamic sound in two ways. Firstly, he considered that the sound waves generated by the quadrupole Lighthill sources could be reflected and diffracted by solid surfaces in their path. Secondly, he considered that surfaces could themselves be a source, in that they act as a boundary to the fluid, and may apply an external force onto the fluid that may be mathematically modelled as a dipole.

Curle begins by considering the general solution to the wave equation with Lighthill term, Equation 2.18, which contains the Lighthill volume sources in addition to a surface integral, shown in Equation 2.19. The integrals, both volume and surface, are with respect to $\mathbf{y}$, a variable representing the source volumes and surfaces. The variable $\mathbf{x}$ in this instance represents the observer. Quite clearly, the surface terms are active in their normal directions, as all components incur a $\frac{\partial}{\partial n}$ term.

$$\rho = \frac{1}{4\pi a_0^2} \int_V \frac{\partial^2 T_{ij}}{\partial y_i \partial y_j} \frac{\mathrm{d}\mathbf{y}}{|\mathbf{x} - \mathbf{y}|} + \frac{1}{4\pi} \int_S \left(\frac{1}{r} \frac{\partial \rho}{\partial n} + \frac{1}{r^2} \frac{\partial r}{\partial n} \rho + \frac{1}{a_0 r} \frac{\partial r}{\partial n} \frac{\partial \rho}{\partial t} \right) \mathrm{d}S(\mathbf{y}) \tag{2.19}$$

Curle continues by focusing on the surface integrals and applying the divergence theorem, and finally substituting Lighthill's stress tensor from Equation 2.17. This gives a solution to the wave equation with both the Lighthill quadrupole sources and dipole sources related to pressures acting on a surface. This is given in Equation 2.20, where in this case, p_i is a normal component of the pressure acting on a surface.

$$\rho = \frac{1}{4\pi a_0^2} \frac{\partial^2}{\partial x_i \partial x_j} \int_V \frac{T_{ij}\left(\mathbf{y}, t - \frac{r}{a_0}\right)}{r} \mathrm{d}\mathbf{y} - \frac{1}{4\pi a_0^2} \frac{\partial}{\partial x_i} \int_S \frac{p_i\left(\mathbf{y}, t - \frac{r}{a_0}\right)}{r} \mathrm{d}S(\mathbf{y}) \tag{2.20}$$

Curle goes on to show that the total acoustical power output of dipole sources is proportional to the sixth power of a typical velocity of the flow (for example, the tip speed of a fan blade). In comparison, Lighthill [22] shows that the quadrupole source is proportional to the eighth power of a velocity. These power laws of the fundamental sources are summarised in Section 2.3.

2.2.3 Ffowcs Williams and Hawkings generalised theory of aeroacoustics

Ffowcs Williams and Hawkings [42] attempted to generalise the solution to the mass and momentum equations, those derived by Lighthill and Curle, by not restricting the solution's validity to the region external to the solid surfaces, but rather also applying the solution inside the solid surfaces. This was done through the use of generalised theory, whereby the location of the sources was dictated through the use of dirac functions. The analysis assumed that the wave equation was valid in the entire, unbounded domain; also inside the surfaces, albeit as an arbitrary solution. Through the use of source placement on solid surfaces, the required mass and momentum is injected into the domain. This is shown in Equation 2.21. Here, $H(f)$ indicates the Heaviside function acting on the surface f, in that $H(f) = 1$ outside of the surface and $H(f) = 0$ inside of the surface. This is applied to the Lighthill source (the quadrupole source), which as already discussed, represents the acoustic sources due to fluid stresses. This implies that the Lighthill sources act only inside the fluid domain. The other sources act only on the surface (the monopole thickness noise and the dipole loading noise), in that the dirac delta function, $\delta(f) = 1$ only on the surface, and zero elsewhere. A modification to the Ffowcs Williams and Hawkings equations also

arises when the surface represented by f is permeable; i.e. does not represent a solid surface, but rather a virtual, data surface.

$$\frac{\partial^2 \rho}{\partial t^2} - a_0^2 \frac{\partial^2 \rho}{\partial x_i^2} = \frac{\partial^2 T_{ij}}{\partial x_i \partial x_j} H(f) - \frac{\partial}{\partial x_i}\left(p_{ij}\delta(f)\frac{\partial f}{\partial x_j}\right) + \frac{\partial}{\partial t}\left(\rho_0 v_i \delta(f)\frac{\partial f}{\partial x_i}\right) \tag{2.21}$$

Ffowcs Williams and Hawkings also showed a further derivation using an alternate method, the Kirchhoff method, in that the field variable ρ is assumed to only exist outside of the surfaces (as opposed to the restriction being placed on the source terms). Essentially, the Heaviside terms are applied to the field variables. As demonstrated by Ffowcs Williams and Hawkings [42] as well as Brentner and Farassat [9, 10], the solution when compared to the Ffowcs Williams and Hawkings equation was devoid of volume sources. Given that the surfaces of these methods could be treated as permeable (the surface terms do no necessarily need to represent a solid surface, but rather can represnt a generalised computational surface), Brentner and Farassat show how the positioning of the permeable data surface influences results. In the case of the Ffowcs Williams and Hawkings formulation, the location of the data surface has no significant effect. When positioned close to the source, or on a solid sound generating surface, the volume terms outside of the surface (Lighthill source terms) take into account the sound sources outside of the surface. When the data surface is placed further from the surface, the effects of the volume terms within the permeable surface are calculated through the compressible equations of fluid dynamics, with their effects calculated on the permeable surface and propagated outwards through means of the surface source terms. In the case of the Kirchhoff formulation, given that volume terms are not included, the data surface must enclose all potential volume sources.

The ability to calculate the effects of the quadrupole sources on a permeable data surface enclosing said sources depends on the ability to compute the wave propagation from these quadrupole surfaces to the permeable data surface. This requires generally higher order, compressible CFD techniques, in order to avoid numerical dissipation of the low amplitude sound waves (in comparison to the aerodynamic pressure scales).

2.3 Fan noise

Neise [29, 30, 31] developed a framework for classifying noise sources of low to medium speed fans used for applications such as heating, ventilation and other industrial purposes. Making reference to the acoustical analogy of Ffowcs-Williams and Hawkings, detailed in Section 2.2.3, Neise discusses which of the source terms of the analogy are most relevant to industrial low to mid speed fan systems, this for both discrete noise components (harmonic components), in addition to 'random' components (broadband noise).

From the outset, Neise argues that for industrial low to mid speed applications, the quadrupole and monopole source terms from the Ffowcs-Williams and Hawkings equation are of smaller significance than the dipole term. The monopole term represents displacement of fluid mass, but Neise argues that this term is of small consequence for industrial applications given that the azimuthal phase velocity of the pressure fluctuations is well below sonic. The quadrupole source only become significant at blade tip Mach numbers of over 0.8, and is due to turbulent stresses, as shown in the Lighthill formulation in Section 2.2.1. Only the dipole source term, argues Neise, has the potential of creating significant noise sources for industrial low to mid speed systems. This source is due to the forces acting on the surfaces.

The earlier experimental work of Chanaud [13] showed how total sound power of a Sirocco centrifugal fan is dependant predominantly on the similarity laws of the dipole, which he too derived from the earlier expressions of Powell [36]. He had shown that the sound power of fans, L_W, is proportional to the atmospheric air density ρ_0, the rotational speed N and the diameter of the fan blade D in the form shown in Equations 2.22-2.24, where the sound power level is in Pa^2. Assuming constant air density and

diameter, the Mach number M dependency of sound generation may also be shown.

$$\text{Monopole: } L_{W(m)} \propto \rho_0 N^4 D^6 \propto M^4 \tag{2.22}$$

$$\text{Dipole: } L_{W(d)} \propto \rho_0 N^6 D^8 \propto M^6 \tag{2.23}$$

$$\text{Quadrupole: } L_{W(q)} \propto \rho_0 N^8 D^{10} \propto M^8 \tag{2.24}$$

Clearly, the quadrupole source terms play a greater role at Mach speeds above unity, while for lower speeds, the monopole and dipole source terms are more efficient sound producers.

Neise then further classifies the dipole source terms into those occurring due to stationary rotating forces and those due to instationary rotating forces. Sound production due to stationary rotating forces (the temporally constant lift and, to a lesser extent, drag) occurs due to the relative movement of the source to the observer, and was first studied by Gutin [18]. Given the non-turbulent nature of this noise (constant surface pressures in the time domain), it arises at only discrete harmonics of the rotating frequency.

Conversely, sound due to instationary forces on blade surfaces has many potential causes, of which Neise notes five. Firstly, a non-uniform albeit stationary flow field may develop at the inlet of the fan. This may occur due to local blockages at the inlet, such as structural ribs. In this instance, although in the stationary domain there exists no temporal change in flow and subsequent forces, a changing force develops on the rotating blade as the blade passes through the local irregularities. This too causes discrete frequencies that are multiples of the rotating frequency, as the process is repeated for every rotation and is thus periodic. If, over time, the inlet flow varies due to atmospheric turbulence, the sound spectrum will contain broadband noise, which produces sound energy between the rotating frequency and harmonics due to it's generally non-periodic nature. Neise names this second mechanism a non-uniform unsteady flow.

Neise's third mechanism is due to vortex shedding, whereby he also notes a particular aerodynamic/acoustic feedback that may occur. Instability waves generated in the laminar boundary layer generate a pressure disturbance when passing the trailing edge. This pressure disturbances may also then travel to the leading edge, thus reinforcing the instability wave. Given the nature of the mechanism, contributions to both discrete frequencies and broadband components may ensue, depending on how the individual fan blades are affected and whether the mechanism is periodic.

Neise's final two mechanism are related to a turbulent boundary layer, which will create local pressure fluctuations on individual fan blades, not necessarily correlated with one another. Due to this weak correlation, broadband sound components will be affected. Finally, secondary influences such as tip clearance mechanisms and noise due to stall are mentioned by Neise.

2.4 Lowson's formulation for rotating sources

Lighthill's formulation [23] for the sound generated by a point force in uniform rectilinear motion had assumed that the source was travelling at a constant velocity. In the formulation, shown in Equation 2.25, a source with a time-invariant strength ($\frac{\partial F_i}{\partial t} = 0$) would generate no sound. Lowson [25] argues that this is quite clearly not the case for propellers operating in a uniform flow field. It could clearly be expected that, even a constant force, when moving relative to an observer, would generate sound due to the relative motion between observer and the surface undergoing a loading (and thus generating a pressure distribution).

$$\rho - \rho_0 = \left(\frac{x_i - y_i}{4\pi a_0^3 r^2 \left(1 - M_r\right)^2} \frac{\partial F_i}{\partial t} \right) \tag{2.25}$$

This was numerically shown to be the case much earlier in the work of Gutin [18]. The need to consider the fluctuating forces, as opposed to a temporal average, is strongly dependant on the velocities experienced by the body, the magnitude of the disturbed flow (which in turn influences the pressure fluctuations), and also the frequencies of interest in the analysis. An analysis of these requirements was conducted by Roger [37] and is carried out in Section 2.4.1.

Using a process similar to that of Lighthill's, Lowson derived an inhomogenous wave equation of the form shown in Equation 2.26. The source terms in the equation consisted of the familiar Lighthill stress tensor, T_{ij}, in addition to source terms representative of surface force fluctuations, F_i, and mass injection, Q, added respectively into the momentum and conservation fluid equations.

$$\frac{\partial^2 \rho}{\partial t^2} - a_0^2 \frac{\partial^2 \rho}{\partial x_i^2} = \frac{\partial^2 T_{ij}}{\partial x_i \partial x_j} - \frac{\partial F_i}{\partial x_i} + \frac{\partial Q}{\partial t} \tag{2.26}$$

Using the fundamental solution (the Green's function) of the wave equation in an unbounded medium, only the $\frac{\partial F_i}{\partial x_i}$ term was considered as a source, this being akin to a distribution of surface forces. The problem was analysed with respect to retarded time ($\tau = t - \frac{r}{a_0}$, the time difference between source emission and observer reception), while assuming that the forces are point sources using the dirac delta function, $\delta = \delta(\mathbf{y} - \mathbf{y_0})$, where $\mathbf{y_0}$ is the vector defining the source location and $\mathbf{y}$ the location of the observer. The basic results of Lowson's paper is shown in Equation 2.27. For a non accelerating source, $\frac{\partial M_r}{\partial t} = 0$ the solution becomes that of Lighthill, as in Equation 2.25. This additional term accounts for the noise due to an accelerating source, such as that encountered due to circular motion.

$$\rho - \rho_0 = \left(\frac{x_i - y_i}{4\pi a_0^3 r^2 \left(1 - M_r\right)^2} \left(\frac{\partial F_i}{\partial t} + \frac{F_i}{1 - M_r} \frac{\partial M_r}{\partial t} \right) \right) \tag{2.27}$$

Lowson [26] further developed the theory in order to tackle the sound propagation due to both the stator and rotor components. The theory contained parameters that allowed rotational speed, blade/vane numbers, multistage radiation and compressor hub velocity to be taken into account. Being in essence an integral solution of Green's equation and thus a free-field solution, the theory was incapable of capturing effects due to ducts and other obstructions, in addition to local flow irregularities (for instance, flow velocities) and their effect on sound propagation. What's more, the theory only took into account sound generation due to dipole producing surface pressure fluctuations, rather than considering the fluid domain itself as a potential source of sound (as was considered in Lighthill's theory).

The work herein will use the frequency domain solution derived by Lowson, and shown here in Equation 2.28. Here, c_n is the complex magnitude of the nth order for any given rotating speed ω. The force acting at the source point and the local Mach number speed are specified either in the direction of the $\mathbf{r} = \mathbf{x} - \mathbf{y}$ vector, which is the vector between the observer, $\mathbf{x}$, and source, $\mathbf{y}$, or in the individual Cartesian components, i.

$$c_n = -\frac{\omega}{4\pi^2 r} \int_0^{\frac{2\pi}{\omega}} \left(\frac{in\omega F_r}{a_0} + \frac{F_i}{1 - M_r} \left(\frac{-M_i}{r} + \frac{x_i - y_i}{r^2} M_r \right) \right) \exp\left(in\omega \left(\tau + \frac{r}{a_0} \right) \right) \mathrm{d}\tau \tag{2.28}$$

2.4.1 Stationary versus instationary analysis

In order to determine whether a transient analysis is necessary, an analysis similar to that carried out by Roger [37] is hereby presented which mathematically shows the necessary conditions required in order for steadiness, or non-transient effects, to be the significant sound generating mechanism, as opposed to transient, fluctuating effects.. The derived relationship, shown in Equation 2.29, assumes that the

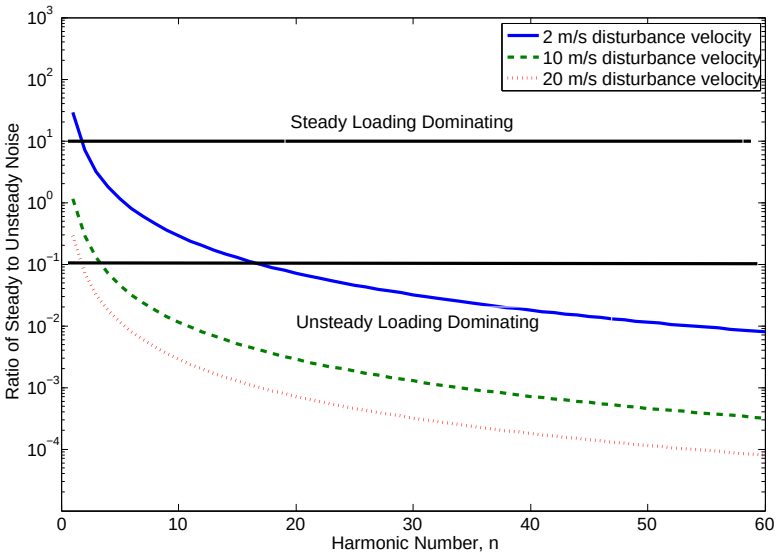

Figure 2.2: Relationship between the noise generated from steady and unsteady loading for the case of a typical alternator geometry

sources are undergoing a constant rotation, with the pressure variations acting on the blades derived from unsteady linear aerofoil theory, with variations in upwash influencing the pressures occurring on the blades. Here, n refers to the harmonic number of interest, a multiple of the rotating frequency (the sound frequency, in Herz, being $f = 2\pi\omega n$), U being a disturbance upwash velocity, ω being the rotating speed, and M the tip Mach number.

$$\frac{\text{Steady Loading Noise}}{\text{Unsteady Loading Noise}} = \frac{1}{n^2}\left(\frac{U}{w}\right)^2\left(\frac{M}{1-M}\right) \tag{2.29}$$

From the relationship, it is clear that the importance of the unsteady loading terms becomes significant when the system operates at a relatively low speed or is small (dictated by the tip speed and Mach number), or when the frequencies of interest are high. It also dictates that the fluctuations occurring in the flow (here represented by an upwash velocity) must be relatively high. Substituting typical values of an alternator, as shown by Wasko and Fischer [40], it is clear from Figure 2.2 that, even with a relatively weak upwash, the noise due to an unsteady pressure fluctuation dominates at the orders higher than the fundamental. This dictates the need for a theory that takes into account temporal variations of the pressures, in addition to time dependant aerodynamic source data.

2.5 Case studies

The theoretical concepts outlined in the previous sections will now be discussed within a practical context, highlighting several case studies in the field of aeroacoustics of rotating machines. Particular focus will be placed on case studies that have used Lowson's formulation from Section 2.4, given it's applicability to the case study studied in this work.

Much work has been conducted in the past with focus on the reduction of tonal noise in fan systems through the use of asymmetrical blade spacing. Mellin and Sovran [28], in defining annoyance as either excessive intensity or a tonal characteristic (which may be present in the absence of a high overall noise), set out to determine optimal blade spacing arrangements given a particular fan blade loading. In the theory, they do not take into account what they call interaction noise; essentially, they assume the

loading on the blades to be constant and not varying, as the case may be when upstream stationary obstructions are present (such as structural ribs). They also incorrectly state that it is this constant loading that produces the significant tonal annoyance, although this can be shown to be incorrect both experimentally, as in Section 4.6.1, and theoretically, as already demonstrated in Section 2.4.1.

They continue with the requirement that the spatial distribution of the pressure waves emitted from the fan can be determined through the measurement of an equivalent fan system with symmetrical spacing, and a subsequent iterative process to ensure the shape of the spectral function is consistent with that of measured data. The spatial shape of the sound wave is then assumed to be constant, regardless of the blade spacing itself (essentially implying that the blade loading is not influenced by the blade spacing). In order to determine the sound generated by a fan system with asymmetrical spacing, the characteristic sound wave shapes are stretched or shrunk to represent the change between blades. For example, if the characteristic sound shape for a blade is a sinusoid, and there are 6 equally spaced blades, the simulated sound curve over one rotation would be a sinusoid with 6 full periods. This, again, is known not to be the case from more recent theory in addition to experimental work. In any case, for an accurate description of the sound field, these fundamental shapes need to be accurately known.

Boltezar, Mesaric and Kuhelj [8] used Lowson's equation in order to show the influences of uneven blade spacing on sound pressure levels with direct application to alternators. In their work, the forces acting on the fan blades were estimated through knowledge of the casing geometry; essentialy, a square shaped sinusoid with four peaks was used for the calculations. The four peaks appear to model the four ribs, much like in this work, whereas the square like shape is used to introduce harmonic components. The blades were modelled as point dipole sources. The work compared several geometries with uneven spaced fan blades to a geometry with 12 symmetrically placed blades. It was shown experimentally, and confirmed through the current body of knowledge, that introducing asymmetrically spaced fan blades shifts the sound energy away from the main blade passing frequencies and on to the neighbouring orders, thus reducing the concentration of sound at particular orders. This was also shown with the numerical implementation of Lowson's equation.

Jeon and Lee [21] use a hybrid approach to examine the sound field generated from a centrifugal impeller operating in the wake of a wedge. Their research examines not only the fluid flow around the impeller, but also the sound generation, its propagation in addition to its reflection from local disturbances. The fluid dynamics calculation is carried out using an incompressible, inviscid vortex method. The forces generated at the blades over time are then used to generate the source terms in Lowson's equation. The sound propagated from Lowson's equation is then calculated across a surface enclosing all sources, and propagated outwards using a Kirchhoff-Helmholtz method, with the necessary assumption that the enclosing surface contains all dominant sources, as discussed in Section 2.2.3. The Kirchhoff method they use draws many parallels to the BEM equation, discussed in Section 6.1.1, in that it is an integral equation consisting of the Green's function and it's gradient, in addition to surface pressures and surface pressure gradients. In doing so, they are capable of modelling moving sources (otherwise impossible with BEM alone) and propagating them outwards while taking into account obstructions (otherwise impossible with Lowson's equation alone). The solution however does not allow the outgoing waves to re-enter the region enclosing the sources, thus preventing true rotor-stator acoustic interactions from being calculated. In comparing the results to both a pure Lowson's approach and experiment, they find that the results are some 2-6 dB higher than those from Lowson's due to the reflections from the wedge. Comparison to experiment yields a favourable improvement over the approach utilising only Lowson's equation.

Choi and Lee [14] continue the work of Jeon and Lee, with the fundamental difference being an analytical derivation of the pressure gradients required in the Kirchhoff-Helmholtz BEM. The analytical derivation is from Lowson's equation itself, thus offering the possibility of quicker solution times in

addition to less sensitivity to the Kirchhoff mesh. This is in comparison to the method of Jeon and Lee, who calculate the pressure gradients by formulating two additional Kirchhoff surfaces some distance apart from the basis surface used for the pressure calculation.

Jeon and Cho [20] and Park, Kwon and Ahn [34] followed with results from an inhouse designed package; their CFD solver SC/Tetra with their aeroacoustic noise solver FlowNoise. The aeroacoustic solver used the Ffowcs-Williams and Hawkings equation, specifically using only the dipole solution for a point force in arbitrary motion and solving for the acoustic pressure in the time domain. Two cases are analysed; firstly, wake interaction noise acting on an airfoil due to the wake from a cylinder, in addition to a Sirocco fan. The aeroacoustic noise spectra due to the impinging wake on the airfoil is predicted accurately, with a strong peak occurring at the frequency related to the generated vortices from the cylinder. For the second case, the spectra is also well predicted, particularly at the blade passing frequency.

2.6 Summary

The theory of acoustics has been discussed by beginning with the fundamental equations of acoustics; the wave equation. Source terms used specific to aeroacoustics were introduced, with several aeroacoustic analogies having similar source terms. The three source terms that form the basis of fundamental aeroacoustic theory are known as the monopole source term, due to displacement of air (or injection of air), the dipole, due to pressures and pressure fluctuations on surfaces, in addition to the quadrupole term, due to velocity fluctuations in the flow itself (flow turbulence). The general consensus in aeroacoustic theory is that for industrial rotating machines operating at subsonic speeds, the dipole term is the dominant noise source. Whether the dipole is the dominant source for the alternator application will be confirmed through experimental work by determining the sound power dependency on rotational speed.

Given this, Lowson's formulation for rotating dipoles will be investigated in the context of the alternator. The method allows the use of incompressible, lower order solvers for rapid transient CFD computations; as a hybrid method, only the acoustic source inputs are required, rather than full calculation of propagating sound waves. The need to calculate transients has been demonstrated; experimental investigations will be carried out to confirm this. Rather than using the formulation to determine only the noise due to the fan loading, the entire rotor of the alternator will be modelled using the acoustic analogy.

Comparison to experimental work will be carried out to determine the ability of the analogy to calculate the sound energy emitted from the alternator. Consideration will be given to not only total sound energy, but also the ability of the analogy to determine frequency content of the sound. Given that the hybrid approach will limit the ability to calculate sound diffraction and reflection from solid surfaces, investigations will follow that will determine the magnitude of this effect through the use of BEM and FEM tools.

Chapter 3

Implementation of Lowson's theory

The following section describes the code developed based on Lowson's method, described in Section 2.4. Additions to the code not standard from the theory are highlighted and demonstrated. These additions are two fold; firstly, a modification is made whereby the dipole source acts only in one direction (in the direction of the fluid domain), thus preventing sound generation into a solid surface. This is particularly required when the clawpole structure is being modelled. Secondly, the implementation of the test stand is discussed, which considers the reflection of the sources from the stand. Trials using simple sources are further carried out for validation purposes.

3.1 Procedure and algorithm

The procedure used for the calculation of aerodynamic sources will be highlighted in this section. Reference should be made to Figure 3.1, which shows the procedure for the process carried out, in addition to details of the functioning of the algorithm based on Lowson's equation.

1. Calculation of instationary CFD data for a given geometry and mesh. The details of the CFD calculation procedure and the mesh will be discussed in Section 5. The mesh is created using ICEM 5.0, the CFD calculations are carried out using the Ansys CFX Version 10.0 solver.

2. Extraction of CFD data over time. For the case where individual surfaces are to be considered, these surfaces are specified and the integrated pressure on those surfaces are extracted over time. Additionally, surface normals are extracted at the first time step, and later computed for successive time steps. The computation uses the transformation matrix shown in Equation 3.1, whereby the vector $\mathbf{y}'$ indicates the transformed coordinates after an angle change $\Delta\theta$ that occurs over a time step Δt. In the case that a finer acoustic resolution is required, an algorithm has been developed which splits up defined surfaces in a post-processing step in the CFD package Ansys CFX.

$$\mathbf{y}' = \begin{bmatrix} \cos(\Delta\theta) & \sin(\Delta\theta) \\ -\sin(\Delta\theta) & \cos(\Delta\theta) \end{bmatrix} \mathbf{y} \tag{3.1}$$

3. The surface forces over time are imported into the Lowson's code, written in Matlab. The details of the nested algorithm are in Figure 3.1. Computational points (or microphone points) are initially defined. Computation can also be defined as a Matlab generated grid (either a plane or sphere), in addition to a grid generated in the meshing program ICEM. Through this technique, an interface can be constructed, which will be later used for the BEM interface (Section 6.1).

4. The program proceeds through the nested segment, in which case computations are carried out for each microphone point, from each surface/source imported from the CFD computation, and for

each of the orders that have been requested and/or are relevant. CFD models used throughout are symmetrical models with periodic boundary conditions. For the example of the quarter model, the four way symmetry means that only every fourth sound order produces noise. Thus, only every fourth sound order is in this case relevant.

5. If requested, the program applies the half-dipole approximation in order to ensure sound propagation in only the direction of the fluid. Details of the half-dipole approximation are discussed in Section 3.2.

6. A further modification of the Lowson's method is carried out by assuming a reflective plate, which models the reflective surface of the test bench. The addition of the reflective plate is discussed in Section 3.3.

7. Once the solution is calculated at all microphone points, for all surfaces and at all the requested and relevant orders, sound power levels can be calculated through the use of the sound power level calculation highlighted in ISO 3745 [3, 4], as shown in Equations 4.3 to 4.5. These can then be further filtered using the A-weighting filter (Equation 4.6) and/or the results can also be exported into a file readable in LMS Sysnoise for BEM calculations.

The algorithm used in the analysis is based on Lowson's solution in the frequency domain, repeated once again here in Equation 3.2. Additional terms to be calculated in the equation include the force in the direction of the observer, $F_r = F_i.\mathbf{n}$, where $\mathbf{n}$ is the surface normal. The Mach number in the direction of the observer is calculated similarly, $M_r = M_i.\mathbf{n}$, where the speed of sound, $a_0 = 343$ m/s.

$$c_n = -\frac{\omega}{4\pi^2 r}\int_0^{\frac{2\pi}{\omega}}\left(\frac{in\omega F_r}{a_0}+\frac{F_i}{1-M_r}\left(\frac{-M_i}{r}+\frac{x_i-y_i}{r^2}M_r\right)\right)\exp\left(in\omega\left(\tau+\frac{r}{a_0}\right)\right)\mathrm{d}\tau \tag{3.2}$$

3.2 The half dipole approximation

The standard formulation of Lowson's equation assumes that the dipole sources act on a surface such that a sound propagation ensues in the direction of both the positive normal and the negative normal direction; this is the figure 8 distribution discussed in Section 2.1.3. This assumption is valid for thin surfaces, such as fan blades, when the total force is taken into account. This is invalid when top and bottom surfaces are modelled using separate sources, much like in this work, in addition to larger structures, such as the clawpole surfaces.

In the formulation carried out in this work, the blade and surfaces are separated into their individual constituents; fan blade surfaces are split into top (high pressure) and bottom (low pressure) surfaces, while the clawpole surfaces are split into their individual root, side and top surfaces. In doing so, care must be taken in modelling the direction of sound generation.

A simplified test case is shown here, where 8 sources acting radially with a 4th order sinusoid fluctuation are modelled. Figure 3.2(a) shows the clawpole geometry to be modelled, with the sources acting on the top surfaces in a radial direction away from the structure. Calculating the resulting sound pressure distribution in the plane of rotation containing the sources, the sound distribution of Figure 3.2(b) is obtained. Quite clearly, with both sides of the dipole forcing active, sound is propagated into the surface in addition to away from the surface. In order to avoid this effect, the effects of the forcing into the surface are switched off, giving the distribution shown in Figure 3.2(c). Here, there is no sound propagated into the centre of the rotor. In both instances, the sound produced in the near-field has 8 main lobes. These are due to the correlated fourth order sinusoid acting on all surfaces, which is in phase for all surfaces.

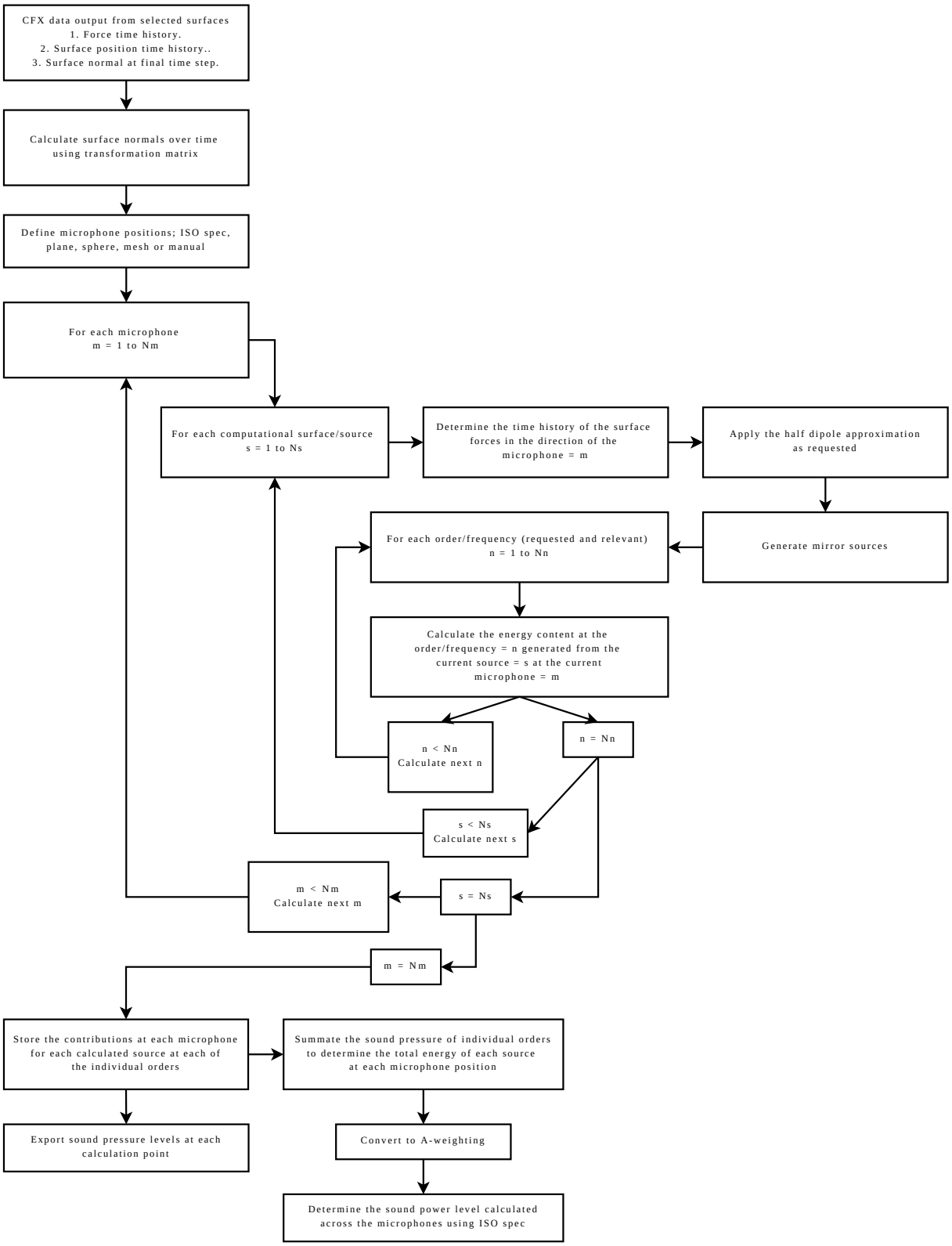

Figure 3.1: Flow chart of CFD and acoustic calculation algorithm

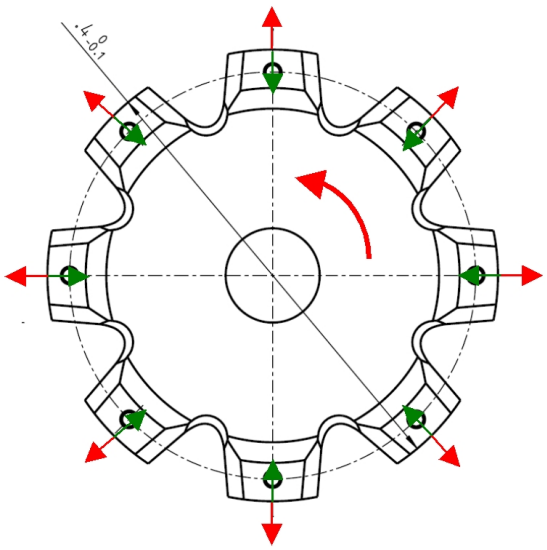

(a) The modelling of 8 clawpole top surfaces

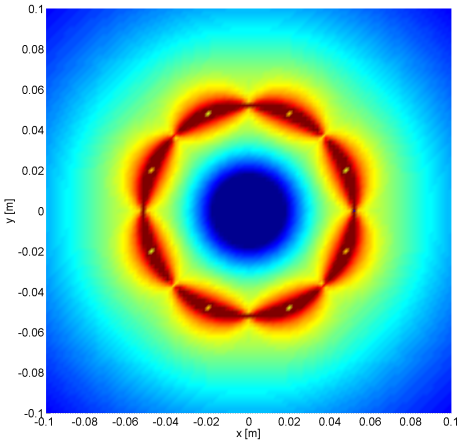

(b) Half dipole modification switched off

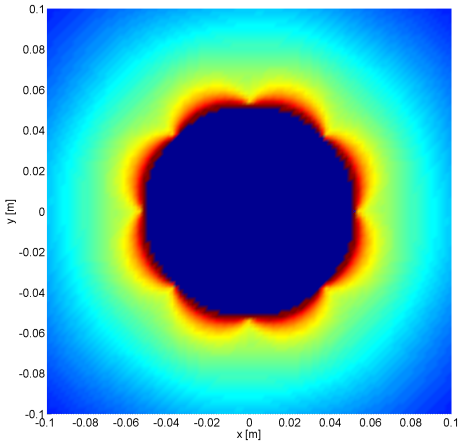

(c) Half dipole modification switched on

Figure 3.2: Half dipole source modelling

There exists a lobe for both the maxima and minima of the forcing, hence eight lobes for the in-phase 4th order fluctuation.

The switch used applies a Heaviside function to the forcing terms of Lowson's equation. The Heaviside function dictates that the forcing terms are multiplied by zero when the dot product between the surface normal and the vector between the observer/microphone location is negative. In this instance, the active surface is facing away from the observer, and thus there is no direct influence of the source on the observer. The modified equation is shown in Equation 3.3, where $\mathbf{r} = \mathbf{x} - \mathbf{y}$ is the vector between observer/microphone and source, and $\mathbf{n}$ is the surface normal of the source/surface.

$$c_n = -\frac{\omega}{4\pi^2 r}\int_0^{\frac{2\pi}{\omega}} \left(\frac{in\omega F_r H\left(\mathbf{r}.\mathbf{n}\right)}{a_0} + \frac{F_i H\left(\mathbf{r}.\mathbf{n}\right)}{1-M_r}\left(\frac{-M_i}{r} + \frac{x_i - y_i}{r^2}M_r\right)\right)\exp\left(in\omega\left(\tau + \frac{r}{a_0}\right)\right)\mathrm{d}\tau \qquad (3.3)$$

3.3 Implementation of an infinite, reflective plane

The implementation of a reflective plane is carried out using the fundamental technique of mirroring sources. This technique essentially ensures that the fundamental Green's solution is valid in the fluid (given that both original and reflected sources are modelled using the Green's function), in addition to ensuring that the normal gradient to the wall is zero, a fundamental boundary condition in acoustic theory, that will be discussed in further detail in Section 6. Essentially, for every source that is considered in the calculation, a 'mirrored copy' is constructed normal to the reflective plane, it's movement also being mirrored. All source properties need to be mirrored to allow the calculation to be carried out; force histories, location histories, velocities and surface vectors. Clearly, the implementation of a reflective plane doubles the source count, and roughly doubles the calculation time.

The surface of the reflective plane is assumed to be at a position $y = 0.16$ m, equivalent to the vertical distance between the alternator axis and the reflective plane on the test bench. This yields the need to transform location, surface vectors, forcing and speed properties, in the form shown in Equation 3.4, where the variable R can be the location, surface vector, velocity and force.

$$R_y^{mirror} = -R_y^{original} \tag{3.4}$$

In order to validate the implementation, a comparison is carried out between a calculation with reflective sources implemented, and one without. The calculation uses a unit strength dipole acting perpendicular to the wall. The dipole is placed 0.3 meters away from the wall. Two sets of calculations are carried out: the first, Figures 3.3(a) to 3.3(b), show the propagation of a dipole, in the plane of the dipole, with the mirror switched off and on respectively. Figures 3.3(c) to 3.3(d) show the sound pressure level acting on the line $x = 0$.

For the non-reflected dipole (Figures 3.3(a) and 3.3(c)), the typical figure 8 distribution is noted, where perpendicular to the dipole's forcing direction at it's origin, there is a low pressure region. Figures 3.3(b) and 3.3(d) show the distributions when the dipole is reflected from a wall at $y = 0$. Clearly, the distribution is accurately mirrored across the wall, with $\frac{\delta p}{\delta n} = 0$, agreeing well with the standard reflecting hard wall boundary condition.

3.4 Validation using a single stationary dipole source

The results of the unit strength dipole are shown in Figure 3.4. The result is compared to an analytical solution of the equation $P = \frac{k}{r}$, where r is the distance from the dipole and k is a factor determined from one solution point from the numerical result and P is an absolute pressure value. The pressure result in the numerical solution is the magnitude of the calculated Fourier coefficients. It is known from the literature that this pressure is proportional to the inverse of the distance, thus the comparison to the aforementioned analytical solution. In this case, the numerical solution at $r = 0.02$ is taken, which is equal to $P = 49.02$. To scale the analytical solution correctly, $k = 0.9804$. The correspondence to numerical results thus shows that the sound propagation from the dipole follows the well known $P \propto \frac{1}{r}$ rule. The numerical solution was calculated at 101 microphone points spread between -1 and 1 meter in the direction of the acting dipole.

3.5 The effect of forcing on radial, tangential and axial sources

The following trials will examine the effects on radial, tangential and axial sources, and their effect on the sound power level for a set of microphones located on a hemisphere above the reflection plane of radius one meter from the source. 66 microphones are used for the integral to determine sound power level. The

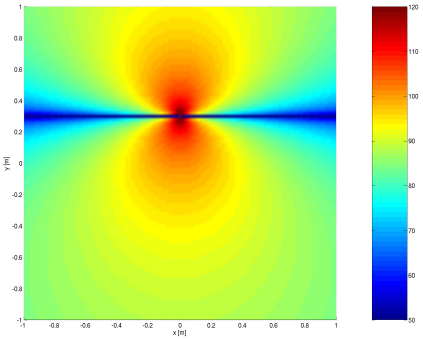

(a) Sound propagation of dipole

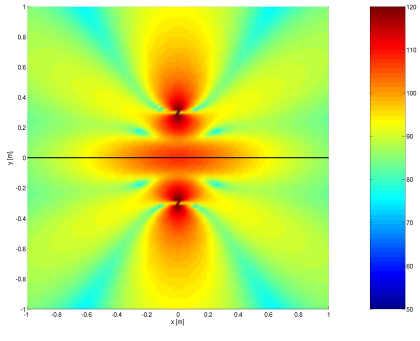

(b) Sound propagation of reflected dipole

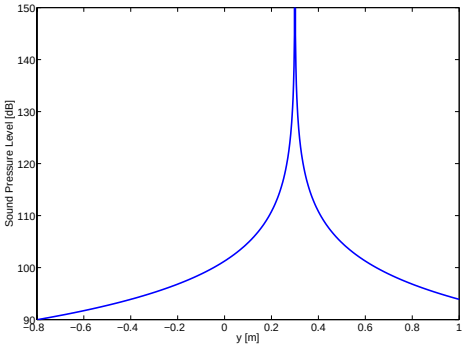

(c) Sound propagation of dipole along $x = 0$

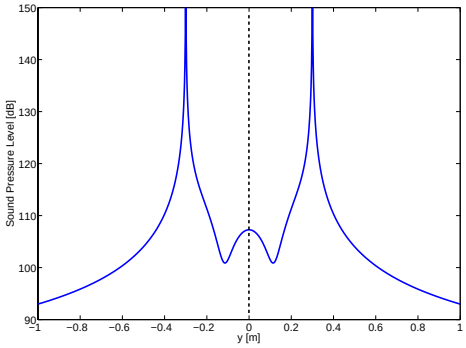

(d) Sound propagation of reflected dipole along $x = 0$

Figure 3.3: Reflected source modelling

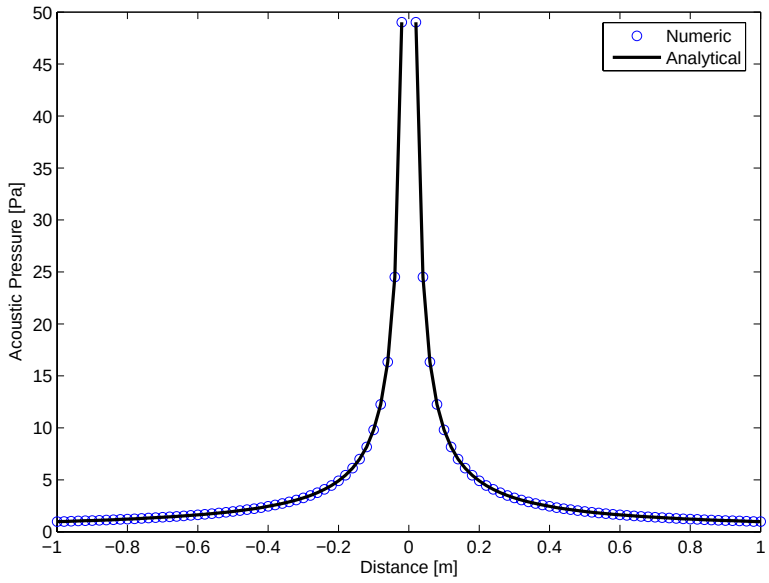

Figure 3.4: Dipole sound propagation normal to oscillation

12 sources used are of unit strength, located at a radius of 0.05 meters and rotating in the z direction (the x-y plane is the rotation plane) at a speed of 10,000 rpm. 1000 time steps are used for the trials. The sources are equally spaced, having equal forcing (unit force), albeit phase shifted. The effects of a 6th order, 12th order, 18th order and 24th order fluctuation will be examined. The choice of the orders is such that an order is examined which corresponds to the number of sources, a multiple thereof, and orders that are in between multiples of the source count. The existence of a reflective plane is assumed in order to identify effects which may be present in the real generator model. The half dipole approximation is turned on in order to focus the effects on a surface propagating sound in only one direction.

It is shown in these cases that, regardless of which direction the sources are acting, there is similarity in that the sound distribution is generally centred around the forcing frequency (Figure 3.5(a) to 3.5(c). Note that although the results are displayed as lines for the sake of clarity, only the points define the calculated orders. Given that the system consist of 12 sources spaced equally with equal, albeit phase shifted forcing, only every 12th order has a corresponding sound.

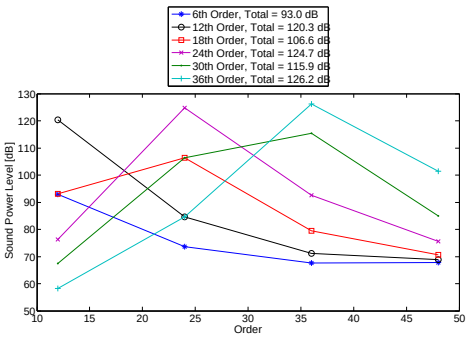

(a) Dipoles acting radial to rotation

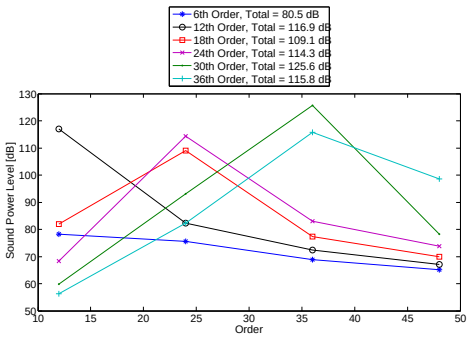

(b) Dipoles acting tangential to rotation

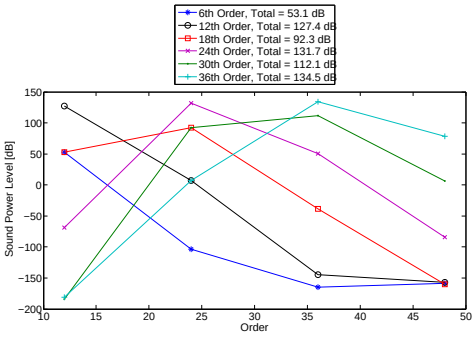

(c) Dipoles acting axial to rotation

Figure 3.5: Influences of the forcing frequency on a system with twelve equally spaced sources fluctuating in varying directions.

For the forcing frequencies that occur at a multiple of 12, it is evident that the maximum peak occurs at the forcing frequency, with the respective ± 12 orders gradually tapering off. The effect here is due to the Doppler shift for rotating sources, and is strongly dependant on the local Mach number.

Also of note is that the sources acting axially are dominated strongly by only one or two orders, with a very strong reduction in the sound power level away from the forcing frequency. This is due to due the half dipole modification. Even with the half dipole approximation switched on, the dipoles acting in the radial and tangential directions produce sound across generally the entire calculated surface, except along the rotor axis for the tangential case. This is because of the direction vector of the sources changes over time with the rotation. For the axial case however, the vector does not change, only the position of

the source, as the vector is parallel to the rotation vector. Due to this, no sound is propagated rearward.

3.6 Summary

The implementation of Lowson's equation into the calculation process has been demonstrated. Computational calculations from Ansys CFX are used as inputs into the Lowson's equation, modelled using Matlab. The software has been made such that acoustic calculations can be carried out on user defined microphone configurations, be it for the purpose of similarity with experimental work, or for the further integration with external software, such as LMS Sysnoise.

Two main modifications to Lowson's standard solution have been integrated, namely the half-dipole model and the reflective surface (for modelling of the test stand). The effects these have on the sound field have been demonstrated. In addition, validation with the analytical dipole solution has been carried out in order to numerically test the program. Simple investigations were also carried out to determine the sound generation of several rotating dipoles, and the way that the sound spectra is distributed in these simple cases. This knowledge will be required when analysing the experimentally measured effects that certain geometrical changes have on the sound propagation.

Chapter 4

Experimental results

The following section will outline the experimental results obtained in the framework of this thesis. The chapter will begin by discussing the two measurement chambers used during the work; the ISO sound power test chamber used at the product development department solely for the purpose of testing alternators, in addition to the 9 microphone sound pressure test facility at the research and development centre. The effects of geometrical modifications on the aerodynamic sound generated will be discussed in detail.

4.1 Experimental setup

Two test facilities are used for experimental studies due predominantly to resource availability. The ISO test chamber, used to measure production alternators, follows strict guidelines for the measurement of sound power levels from alternators over a speed ramp. Given it's purpose built nature, it can provide a wealth of information over a large speed range, with direct analysis of individual sound power orders. Being built and first used in 1997, the test bench offers the possibility of testing alternators using both an internationally recognised testing method, in addition to a well standardised one.

The 9 microphone test bench on the other hand offers the possibility of measuring noise at specific speeds, while also changing microphone positions manually. The analysis software is also somewhat more flexible, allowing separate analysis of microphone spectra in addition to setting measurement duration, sampling frequencies and windowing. This is in contrast to the ISO bench, which is specifically designed for the measurement of sound power levels, with some possibility of determining directional noise characteristics. In addition, the ISO test bench provides little opportunity for changing measurement settings.

4.1.1 ISO test facility

The ISO test facility conforms to the DIN 45635 test standards, the German equivalent to the ISO 3745 standard [1, 3]. Although a more recent version of the standard exists [4], the test bench has not to this stage been updated to reflect these new standards. Comparison of the two standards yields two main differences; the pressure and temperature correction (discussed in Section 4.2) is slightly different, as are the microphone positions, whereby the newer standard contains 20 microphones instead of 10, all of which have different positions compared to the older, 10 microphone specification.

The test chamber is semi-anechoic, whereby all walls (except the ground) are covered in sound absorbing wedges that absorb outgoing sound waves and prevent reflection back into the test chamber. This, in effect, approximates sound propagation in a free-field. The size of the room is 7.8 meters by 5.5 meters

by 3.5 meters, ensuring that the shortest distance from the generator to a wall is 1.8 meters. The plate that the generator sits on has a diameter of 2.4 meters.

The test bench and the analysis procedure is unique in that it reflects the needs of the alternator development division at Bosch [27]. Aerodynamic tests are conducted such that the alternator is accelerated from 1,000 rpm to approximately 18,000 rpm. The rotation speed of the alternator is measured optically with an optical light and receiver; the light measures impulses given off by a mark on the pulley. Given that the speed range of interest of the alternator model in this work is smaller, and that the ability of the generator to operate at very high speeds is uncertain, speed runs were conducted up to a maximum speed of 12,000 rpm. The alternator is accelerated to this speed at a rate of 100 rpm/s while the pressure signals from the microphones are recorded at a sample rate of 40 kHz. The fact that the sample rate is 40 kHz ensures that, at a speed of 10,000 rpm, all orders up to the 120th are measurable (the system however only calculates up to the 60th order). Results are obtained for each 10 rpm speed increment, meaning that at each speed increment an FFT is carried out over a time signal of 0.1 ms. Over this time increment, a Hanning window is used in order to remove effects due to a non-periodic time sample.

During this measurement time, the alternator undergoes a certain number of full rotations. These N full rotations are averaged and re-sampled at a rate with which a subsequent FFT produces data points at the first order and multiples thereof up to the maximum measurable order, the 60th; the spectral lines are in 1 order increments. Thus, the energy content is captured at every order and multiples thereof, and there is no need to integrate the orders.

The fact that the system utilises a constant measurement time over the entire speed range leads to more sample points per rotation at lower speeds and consequently less sample points at the higher speeds. An optimal solution would be to sample n full rotations, where n is an integer. In such a case, the time signal will be more likely to be fully periodic, given that n full rotations are measured, while also providing the ability to be consistent with the number of samples per rotation. This has the benefit of ensuring that the resolution of the data is identical at all speed ranges. Unfortunately, such a solution is not available at the ISO test facility.

At each 10 rpm speed interval (0.1 second time measurement interval), the total sound pressure level and orders at each of the ten microphones are determined. The pressure levels calculated are corrected for local ambient conditions (pressure and temperature) using the correction factor discussed in Section 4.2. An average of the sound pressure is then determined by calculating the average energetic value, weighted with the A weighting filter, discussed in Section 4.5. This value is then converted to sound power (to eliminate the dependence on microphone to source distance) by integrating the pressures across the surface forming the microphones.

The alternator is placed on a fully reflective test bench (Figure 4.1). Ten Brüel & Kjær microphones of type 4165 are used to measure the sound pressures. In this work, the orders analysed were restricted to orders 1-16, 18, 20, 24, 30, 32, 36, 40, 42, 46, 48, 50 and 56 due to constraints in the measuring system. Total sound power level is determined as the rms values of the time signal; this ensures that the total sound power level contains all sound (including broadband components), and not only the sound components calculated in the order analysis. The sound power levels from the ISO test bench are given only in A-weighting. The signal processing is carried out using custom built software from Additive GmbH.

4.1.2 Nine-microphone test facility

The nine-microphone test facility, rather than conforming to the ISO standards outlined above, allows flexibility in the positioning of microphones. The test bench used is similar to the ISO test facility, in that the alternator is mounted on a fully reflective plane. For the microphone positioning, a mount was

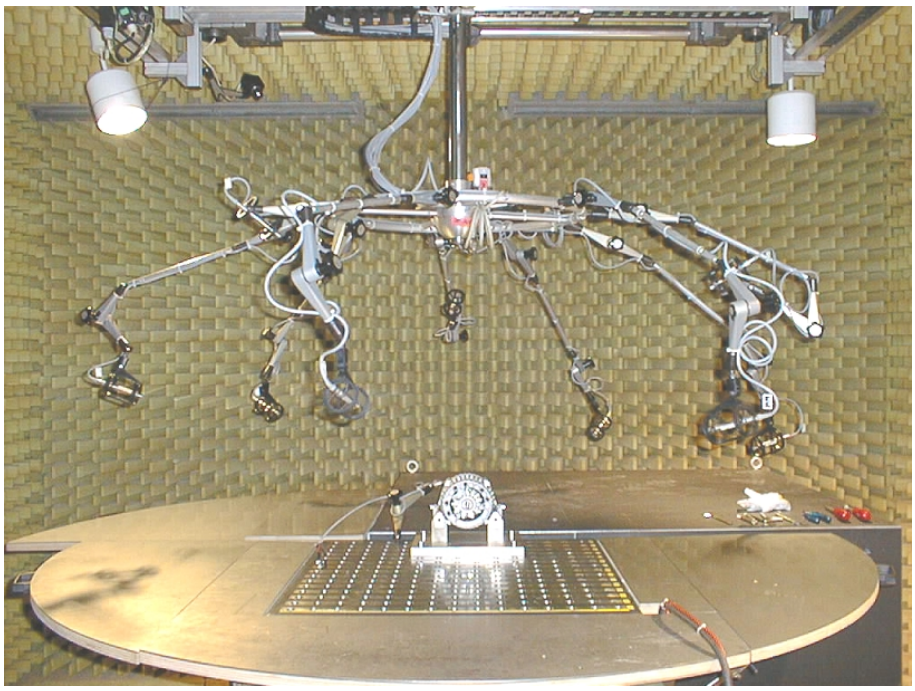

Figure 4.1: ISO test bench

constructed which allowed nine microphones to be placed in a semi-circle either parallel to or perpendicular to the alternator (Figure 4.2). Unlike the system at the ISO test bench, a detailed analysis of each microphone is possible through the data acquisition system. 9 Brüel & Kjær ICP 1/4 ” microphones were used during the tests. The microphones were calibrated at 1000 Hz within a tolerance of 0.6 dB. The Dactron data acquisition software was used in the testing, capable of accepting up to sixteen channels. Data rate acquisition was conducted at up to 33 kHz, with a frequency resolution of 4 Hz for spectral line analysis. Sample averaging using 100 spectra was carried out. Unlike the DIN/ISO test bench, measurements at the 9 microphone test bench were carried out at constant speed (10,000 and 12,000 rpm), rather than taking measurements over a predefined measurement ramp.

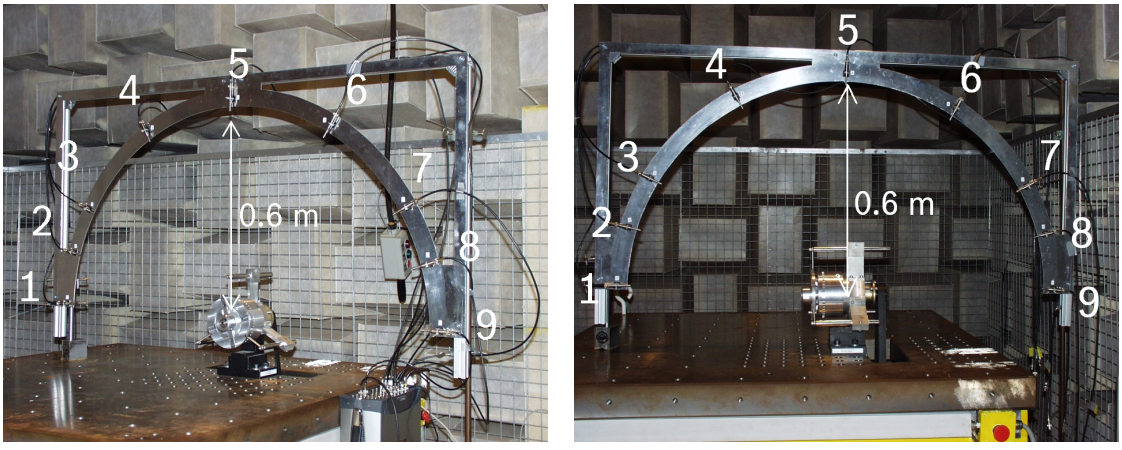

(a) Lateral configuration

(b) Longitudinal configuration

Figure 4.2: Nine microphone test bench

4.2 Temperature and pressure correction

As discussed by Hübner [19], differences in atmospheric pressure, temperature and humidity have the effect of altering sound propagation characteristics. These differences can be related to the differences in the characteristic impedance of the medium in comparison to some standard impedance, where the impedance is $\rho_0 c_0$. Hübner's findings were adopted in the ISO and DIN standards [4, 1], with Equation 4.1 showing the pressure correction from the older ISO 3745-77 [1] and Equation 4.2 from the newer ISO 3745-2003 standard [4]. The ISO system automatically accounts for the temperature and pressure differences using the older DIN standard; although the standard is not up to date, given that the atmospheric conditions (atmospheric temperature, t_0, and pressure, P_0) at the test locations are close to that at sea level, and thus in both instances the correction close to zero, a large difference between the two corrections does not result.

$$K_0 = 20 \lg \left(\sqrt{\frac{293}{273 + t_0}} \frac{P_0}{1000} \right) \tag{4.1}$$

$$K_0 = 10 \lg \left(\sqrt{\frac{313.15}{273.15 + t_0}} \frac{P_0}{1013.25} \right) + 15 \lg \left(\left(\frac{296.15}{273.15 + t_0} \right) \frac{P_0}{1013.25} \right) \tag{4.2}$$

4.3 Calculation of sound power level from microphone pressure data

The calculation of the sound power level from the sound pressure values obtained from the microphones is calculated as per the standards in [1] and as outlined in the internal Bosch report [27]. These calculations are carried out automatically by the ISO test system; the results from the 9 microphone test bench were left as sound pressure results given that the test planes used for those microphone experiments were not conductive to accurate sound power level measurements; sound power measurements generally require that microphones surround the sound emitter at an equal distance from the sound emitter in order to capture sound propagation in all directions.

The sound power level is calculated from the sound pressure values by obtaining the average of the energetic value of the sound pressures at each of the n microphones and multiplying them by the representative surface area across which they act. For microphones positioned one meter away from the measured source and located along a hemisphere, this is equivalent to 6.28 m^2 total area. The microphone positions at the ISO test facility are positioned such that it may be assumed that each microphone represents a pressure distribution across an equal surface, thus no particular microphone is unequally weighted. Equations 4.3 to 4.5 show this formulation, where L_{WA} is the A-weighted sound power level, L_{PA} the A-weighted microphone averaged sound pressure level, L_S the measurement area constant, K_0 the ambient pressure and temperature correction from Section 4.2, n the number of microphones, L_{PAi} the A-weighted sound pressure level at the ith microphone, and A_s the measurement surface area enclosed by the microphones.

$$L_{WA} = L_{PA} + L_S - K_0 \tag{4.3}$$

$$L_{PA} = 10 \lg \left(\frac{1}{n} \sum_{i}^{n} 10^{0.1 L_{PAi}} \right) \tag{4.4}$$

$$L_s = 10 \lg \frac{A_s}{1} \tag{4.5}$$

Test	Orders									Total
	4	8	12	24	32	36	40	48	56	
1	78.5	68.4	83.3	75.6	73.9	75.0	94.0	88.3	90.7	97.6
2	75.1	72.2	82.9	71.8	73.3	76.6	91.7	84.8	83.4	95.1
3	77.3	70.3	82.2	75.0	74.3	76.9	93.0	85.5	85.2	96.0
4	78.9	69.4	83.7	75.1	73.0	74.3	91.1	85.9	89.9	95.9
5	78.5	68.4	83.5	75.0	73.7	74.9	91.0	86.2	89.8	95.9
Std. Dev.	1.53	1.58	0.556	1.54	0.504	1.14	1.31	1.32	3.29	0.916
95% Confidence.	1.34	1.38	0.487	1.35	0.441	1.00	1.15	1.16	2.88	0.803

Table 4.1: Sound Pressure Level [dB(Pa^2)] of reference geometry on different days

4.4 Repeatability of experimental results

In order to validate the numerical results, the measurement of a reference geometry is repeated over a period of time to determine repeatability of measurements. A sensitivity study was conducted to determine how these results varied on a day to day basis, shown in Table 4.1. These results were from experiments conducted at the 9 microphone test facility, as those facilities were used throughout a period of several weeks, and thus results obtained could show the sensitivity expected. Clearly, individual harmonic results were noted to have a 95% confidence interval of up to approximately 3 dB for the 12,000 rpm reference geometry case. The 95% confidence level of the total sound pressure level was approximately 1 dB. Being conducted on different days, several reasons for variations are possible; the installation and re-installation of test microphones and stands, microphone recalibration and atmospheric conditions all have a bearing on repeatability (note that atmospheric pressure and temperature corrections were not carried out during the 9 microphone tests).

Given that the 9 microphone system does not automatically output order data, the spectra are integrated over a band of 200 Hz (at 12000 rpm, this equates to 1 order; half an order to the left of the frequency of interest, half an order to the right). The integral is so sized in order to ensure that energy leaked away from the exact frequency corresponding to the orders (due to, for example, small inconsistencies in the symmetry, fluctuations in the speed or windowing of data) is contained within the energetic calculation. Examples of these spectra will be shown in more detail in Section 4.7.

4.5 The A-weighting

The ISO system at the product development division, given the customer focus placed there, uses the A-weighted filter for the analysis of sound data. This filter modifies power levels across the frequency spectra with respect to the varying sensitivity of the human ear to different frequencies, based on the sensitivity curves at 40 phons. The adjustment to the sound pressure and sound power levels to the corresponding A-weighted values is carried out using Equation 4.6, where f is the sound frequency in Herz, and $\Delta L_A(f)$ is the delta to the unweighted sound power level.

$$\begin{aligned} A(f) &= \frac{12200^2 f^4}{(f^2+20.6^2)(f^2+12200^2)\sqrt{f^2+107.7^2}\sqrt{f^2+737.9^2}} \\ \Delta L_A(f) &= 20\lg\left(\frac{A(f)}{A(1000)}\right) \end{aligned} \tag{4.6}$$

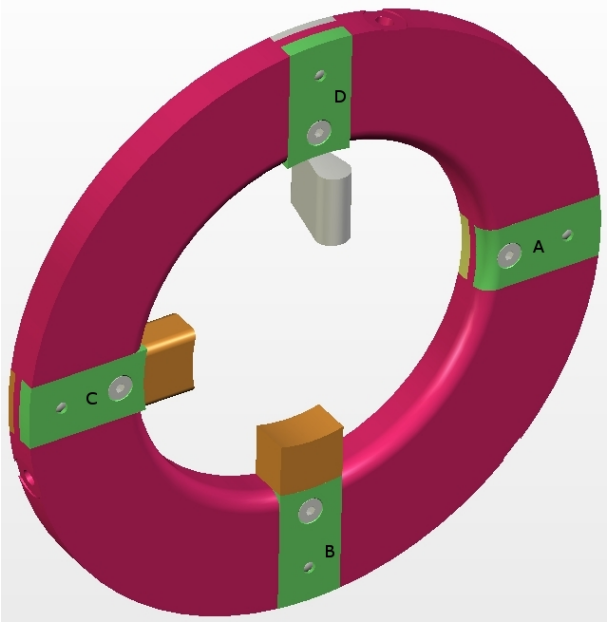

Figure 4.3: Upstream shield and various rib designs. (A) Shield design without ribs, (B) square rib design, (C) rounded rib design and (D) aerofoil-type design

4.6 DIN/ISO 10 microphone sound power tests

The following section outlines the experiments carried out at the ISO test bench. A variety of geometries were tested, based on the reference design shown in Section 1.5. In particular, the aeroacoustic noise effects due to the introduction of upstream ribs is shown, in addition to the types of rib design , clawpole geometry and fan design. Further influence on rib positioning is also investigated. The investigations are carried out on a speed ramp between 1,000 to 12,000 rpm, with detailed spectra analysis carried out generally at 10,000 rpm.

4.6.1 Effect of upstream ribs

Figure 4.3 shows the four rib designs used in order to test rib design effect on noise production, in addition to the end shield used to hold the ribs. Each rib design is tested independently of the others (i.e. test 1 with four ribs of design A, test 2 with four ribs of design B etc). Design A is a design that retains the shape of the shield such that investigations without ribs can be carried out. Design B introduces square shaped ribs. Design C is based on design B, albeit with smoothed edges of radius 2 mm. Design D introduces an aerodynamically smooth profile. The purpose of these various rib designs is to firstly determine the effect of upstream ribs on sound generation, and secondly the influence that aerodynamically favourable surfaces have on improving the downstream flow and thus aerodynamic noise generated. In this section, only the differences between design A and B will be discussed, in order to determine how strong the influence of upstream disturbances is on noise generation. Section 4.6.3 will discuss in further detail the other rib designs.

The effects of removing the upstream ribs (using design A instead of design B) are clearly shown in Figure 4.4, for the case with the standard clawpole fingers (without chamfers) and with a smooth cylinder (see Section 4.6.2 for a description of the clawpole geometries). Both results are shown here, as they show an indication of the noise influence the ribs have on both the fan generated noise in addition to the total generated noise, and thus can be concluded the influence that the ribs have on the clawpole generated noise.

Total sound power without the ribs (Figure 4.4(a)) is reduced by almost 6 dB(A), which is equivalent

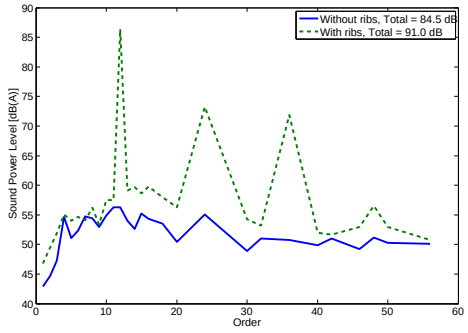

(a) Effect of upstream ribs on noise, without clawpole

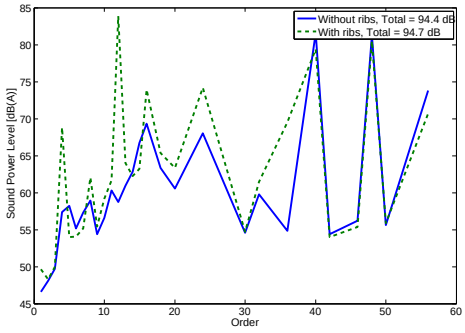

(b) Effect of upstream ribs on noise, with clawpole

Figure 4.4: Effect of ribs on sound propagation at 10,000 rpm

to one fourth the energy of the end shield with design A ribs (a 3dB reduction being a halving of the sound energy). Without the ribs, the surfaces within the rotor undergo a fairly constant pressure as the rotor rotates relative to the stator. Small scale disturbances are in any case present, such as the pressure fluctuations in the turbulent boundary layer. Vortex shedding from the fans due to pressure differentials from the top and bottom surfaces are also present. With regard to the stator holes as a noise source, this is expected to be minimal as the rotor in this case is a smooth cylinder; stagnation pressures generated at the holes of the casing would propagate onto the rotating cylinder, but, given the consistency of the surface, would not change and thus would remain a stationary pressure distribution. This noise generating mechanism will be discussed in further detail in Section 4.6.2, where it will be shown that the effect of the rotor and stator interaction due to these holes in the casing (see Figure 1.1) has a predominant influence on the 40th, 48th and 56th orders. These orders are not present in Figure 4.4(a).

It is also noted from the results without ribs and without clawpoles that there are no dominant orders. Even the 12th order, the first blade passing frequency from the fan blades, is essentially at levels equal to surrounding broadband related orders (for example, the 11th and 13th orders). This suggests that, in this case, broadband noise sources play more of a role in sound generation than the constant pressures on the blades, which would be expected to generate sound at distinct orders (blade passing frequency and harmonics). From the theory of Section 2.4.1, it was shown that steady and unsteady loading can play at least an equal part in noise generation, whereby from the theory of Gutin and Lowson, the noise should only be generated at orders equivalent to multiples of the number of surfaces. Clearly, the constant loading has little influence on the blade harmonics as it's contribution is below that of the broadband contribution. Essentially, any sound generated at frequencies other than the symmetry of the system (in this instance, without clawpoles, the 48holes and the twelve blades yield a 12 symmetry) must be due to random turbulence which reduces the periodicity of the blade loading, or indeed inconsistencies in the geometry itself which undermine the assumption of symmetry and equal blade spacing/shape.

The sound results with the ribs once again highlight the importance that temporal changes in the rotor pressures have. The 12th order, the fundamental blade passing frequency, increases by 30 dB(A) due simply to the upstream ribs and the wake they cause in the rotor. Total sound power levels increases by 6 dB(A). The result also once again confirms the need, as was discussed in Section 2.4.1, of modelling the transients in the numerical simulations. The assumption that the temporal averages of the blade surface pressures do not change significantly with the upstream ribs is not valid, the instationary rotor-stator interaction showing a significant contribution to total and tonal noise.

The results with the clawpole assembly (Figure 4.4(b)) show that the effect of the ribs, at least with respect to total sound power level, are minimal, with a reduction of only 0.3 dB(A) noted with the removal of upstream ribs (design A). It is clear that with the clawpoles, the dominant orders are no longer only

the fan blade orders, taking the fundamental 12th order as an example. The clawpole itself generates significant noise sources at the 40th, 48th and 56th orders, in addition to some contribution at the 4th and 16th orders. These sources will be discussed in more detail in the following chapter, in addition to how these sources change with small changes to the geometry. Clearly, the introduction of the ribs in this system only influences significantly the lower orders; the higher orders, due to the interaction between the clawpoles and the casing holes, are affected only minutely.

Clearly, the upstream ribs, although being closest to the blades, also have an influence on some of the clawpole orders. In particular, a very strong influence is noted at the 4th and 16th orders, with the 8th order being particularly weak. Although the clawpole structure consist of eight equally spaced, equally shaped surfaces, these surfaces do not necessarily share similar pressure distributions. This is due to the placement of the symmetrical 12 bladed fan, which introduces a variation from clawpole to clawpole for every second clawpole (12 fan blades and 8 clawpoles yields a symmetry of 4). Thus, only every second clawpole undergoes similar pressure distributions, the fundamental clawpole order thus becoming the fourth. The influences of the ribs on these lower orders is evident as seen in Figure 4.4(b), but does not necessarily imply a direct influence on the clawpoles; given the proximity of the fan blades to the clawpoles themselves, any variation to the fan blade forces also influences the clawpole pressures, in particular at the root of the clawpole. The variation of the clawpole orders due to the ribs can thus be twofold; a direct influence of the flow impinging on the clawpoles from the ribs, and an indirect effect of the different fan blade forces acting on the local clawpole surfaces. These two effects are naturally coupled and cannot be isolated, as a changing pressure has influences on the local flow.

The influence of the ribs on higher orders is not as significant. Given the dominance at these orders and their small change, the change in total sound power level is minute. It is noted however that for these higher orders, the small influence of the ribs is a positive one; the ribs slightly reduced the higher orders associated with the interaction between the clawpoles and the casing holes. The ribs have the effect of reducing the well correlated, 48th order pressure fluctuations at the clawpole surfaces, and introducing a lower order (predominantly 4th) fluctuation due to the ribs. This effectively shifts some of the energy from the higher orders into the lower ones; this is noted in the results as an increase in lower clawpole orders and a decrease at higher orders.

4.6.2 Effect of clawpole geometries

Figure 4.5 shows the investigated clawpole designs. Design A is a cylindrical surface designed to allow investigation of noise surfaces purely from fan sources. The cylindrical design drastically reduces the noise generation otherwise associated with clawpole/stator interactions. Design B introduces a typical alternator clawpole shape. As discussed in Section 1.5, only half of a typical rotor is modelled in the axial direction. Thus, there are eight clawpole roots and finger-middles modelled, in addition to eight opposing tips. Design C introduces details common to existing alternator rotors; a partial root-chamfer at the leading edge designed to reduce interactions with the stator, in addition to a complete trailing edge chamfer often introduced in alternators for magnetic noise reduction.

The results from Section 4.6.1 will be once again referred to, in this instance with a focus on the differences between the measurements due to clawpole geometries. In addition to a comparison between the cylindrical structure and the clawpoles, a comparison will also be made with the chamfered clawpole. Two comparisons are presented in Figure 4.6, one comparison with the A-side fan geometry in place, the other comparison without the fan blades, in order to segregate orders affected by both clawpoles and fan blades (for example, the 24th order).

It is noted that the addition of clawpole structures to the variant with the fan blade increases the total sound power at 10,000 rpm by up to 3.7 dB(A) for the geometry without chamfers, the chamfered

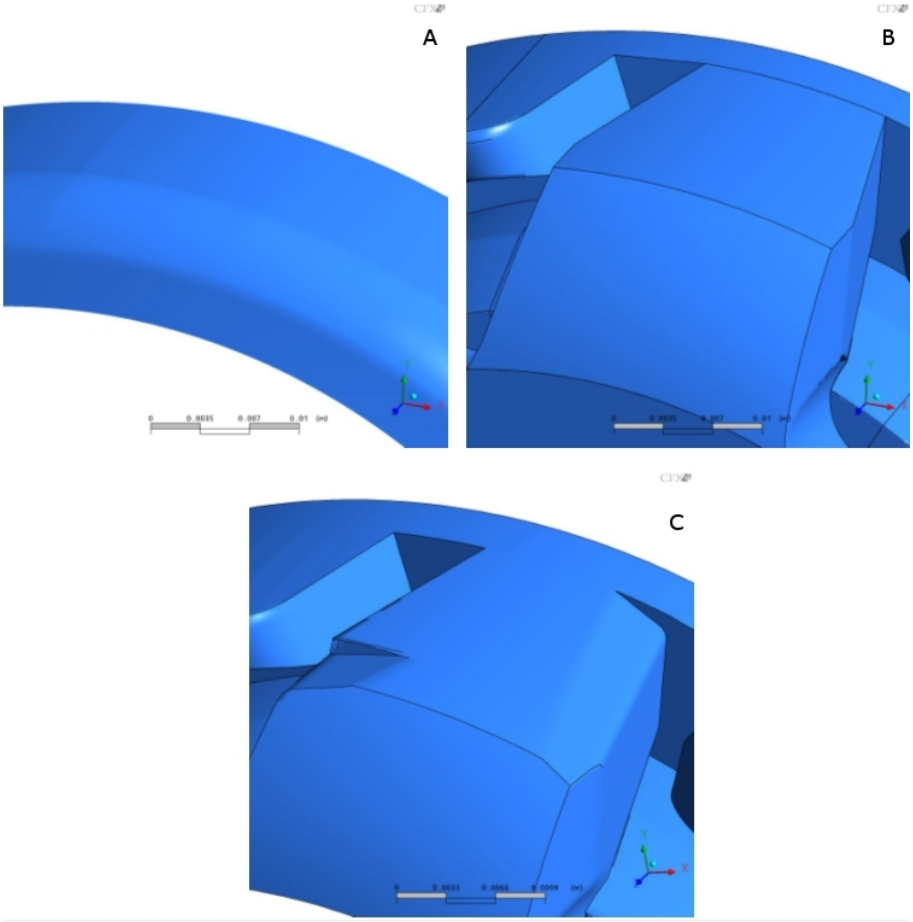

Figure 4.5: Clawpole designs (A) smooth cylindrical surface, (B) simplified clawpole design, (C) clawpole design with leading edge root chamfer and trailing edge chamfer

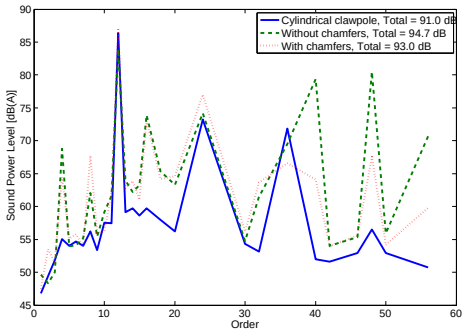

(a) Effect of clawpoles on noise, with A-side fan

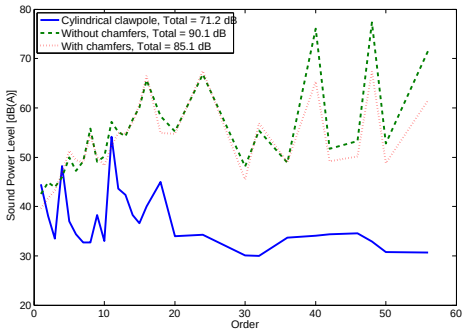

(b) Effect of clawpoles on noise, without A-side fan

Figure 4.6: Effect of clawpoles on sound propagation at 10,000 rpm

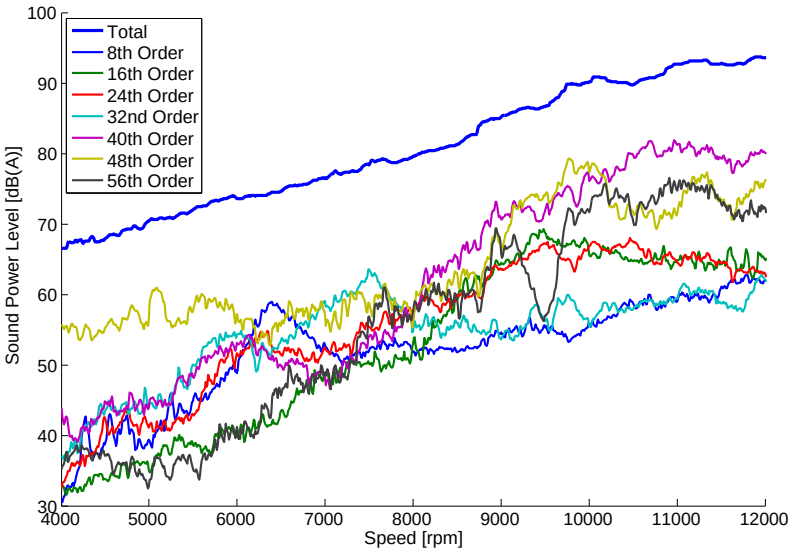

Figure 4.7: Speed ramp of clawpole geometry without chamfers and without fan

clawpole adding less sound energy, 2 dB(A). Without the fan blade, the increase in sound power level is significant, with the chamfered clawpoles alone adding 14 dB(A). An additional 5 dB(A) occurs with removal of the chamfers. Clearly, the added energy is predominantly at the higher orders, in particularly the 40th, 48th and 56th, whose influence from the fan geometries is minimal, at the level of broadband energy. Comparison between the fingers without fans indicates that the additional clawpoles introduce energy predominantly at every 8th order, due to the eight symmetrical, equally spaced claw fingers, with a general concentration of energy at the higher orders. The numerical analysis in Section 3.5 showed how a concentration of energy occurs at the frequencies of the excitation, with energy contributions also at orders corresponding to $\pm n$, where n is the number of symmetrical surfaces, in the case of the clawpoles, this being eight.

Observing further the results without the fan, it is clear that some energy is also focused at the 16th and 24th orders, with the 8th order not being particularly strong. This would come to imply a fluctuating disturbance focused at this 16-24 frequency range, but observation of the speed curve (Figure 4.7) for the normal pole finger shape indicates that the strength of the 16th and 24th orders begins to weaken at about 9,000 rpm and continues to do so up to 11,000 rpm. From 11,000 rpm, these orders are noted to be of the order of the 8th, as expected. Otherwise, the 40th, 48th and 56th orders once again predominate, indicating the presence of a forcing fluctuation centred around these high frequencies, due to the interaction between the clawpoles and the 48 openings. The fact that orders ± 8 are influenced is due to the Doppler effect for symmetrical systems. The general increase in sound power level from the system without fan, even for orders between every 8th, can be contributed to the increase in broadband turbulence due to the addition of the fingers.

4.6.3 Effect of rib shape

The rib designs investigated have been briefly mentioned in Section 4.6.3, their respective cross-sections are shown in Figure 4.8. As previously mentioned, a rectangular rib, slightly rounded rectangular rib, and a streamlined rib are investigated. Studies into the effects of the ribs are carried out on only the geometry with cylindrical clawpoles, as the studies from Section 4.6.3 indicated that the ribs themselves have a marginal influence on the clawpole noise but more so on the fan noise, as in that case most of the energy was centred at the orders caused from the clawpole and casing hole interactions. The results are

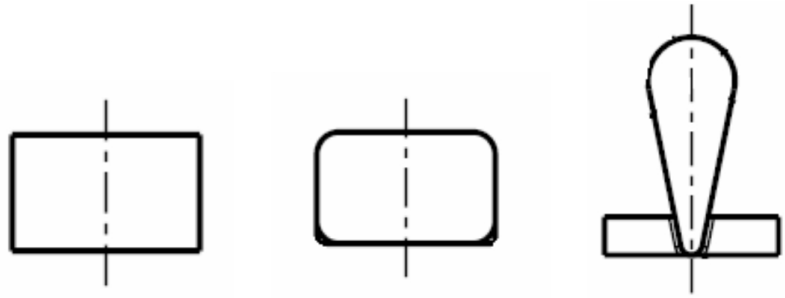

Figure 4.8: Cross section of tested rib designs

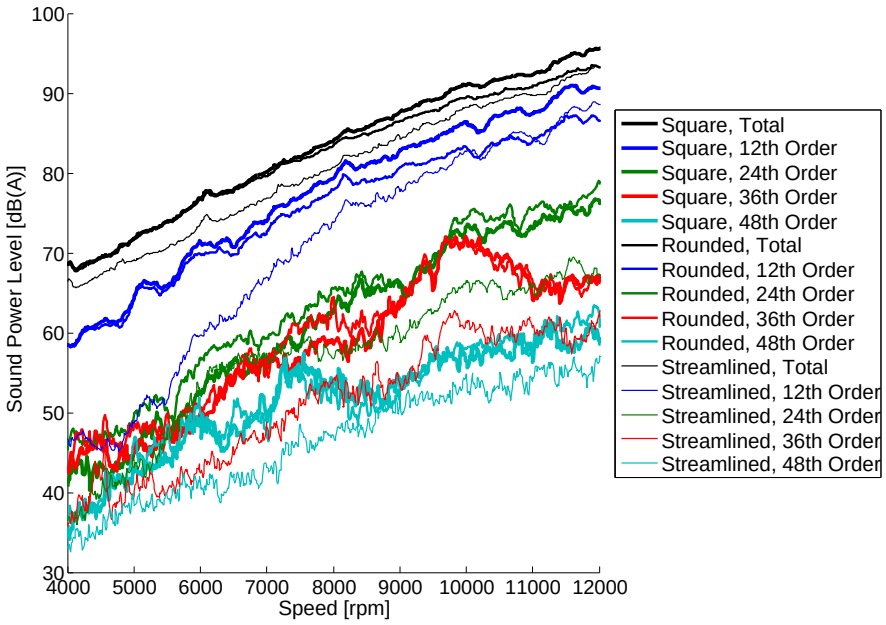

Figure 4.9: Speed ramp of various rib geometries and the effects on total sound power level and particular orders

shown in Figure 4.9 for the entire speed ramp, with the first 4 fan orders displayed. Given that without the clawpole structure only the first four fan blade orders are present, these are also the most considerable sources of sound.

The results indicate quite clearly that across the entire speed range, for all types of ribs, the 12th order dominates. This is due to the fundamental forcing frequency on the blades, caused by the disturbance from the ribs, occurring at a low excitation harmonic; the fact that there are four ribs induces a base 4th order fluctuation. Irrespective of the frequency content of the produced vortices behind the ribs, the fundamental disturbance on the blades remains lower order, thus inducing stronger lower order blade passing harmonics. It is expected, as analysed in Section 3.5, that a change in the rib number, in particular to a much higher count, would thus in turn produce a subsequent shift in the frequency behaviour, much like the centreing of the energy at higher frequencies that occurs due to the interaction between the high number of holes and the clawpole surfaces.

Given the significant weighting on the 12th order, the total sound power level is strongly dependant on this order. At very low speeds, it is quite clear that the streamlined shape yields very low 12th order noise due to the smaller wake region downstream of the rib. At higher speeds, it is clear that the noise becomes similar to that of the slightly rounded rib.

It is also noted that, in comparing the square ribs and the rounded ribs, the reduction of the main 12th order occurs as expected due to an overall decrease in the downstream wake, however this is combined with a slight increase of the 24th order. This implies a slight increase in the frequency content of the wake impinging on the surfaces. Rounded surfaces generally have higher Strouhal numbers than square cross-sections, which tend to produce a wake of shorter length scale [33]. This is indicative of a higher frequency excitation component from the ribs acting on the rotating surfaces.

At higher speeds, it is noted that the difference between the rounded ribs and the streamlined ribs becomes reduced. This is due most likely to an increase in the flow rate with the streamlined ribs, given that the streamlined ribs have a smaller inlet cross-section presence. The size of the inlet cross-section influences the flow entering the alternator, and from the simple relationship from Mellin and Soufran [28], it is clear that a general increase in flow throughput yields, generally speaking, an increase in total sound power. The benefits of the streamlined inlet disturbances are thus at higher speeds not as clear; the general expectation of lower sound due to reduced wake is not entirely evident due to the subsequent increase in flow rate.

4.6.4 Effect of rib shield positioning

An analysis on the effect of end shield positioning is carried out in order to determine the significance such positioning has on the sound propagation. As can be seen from Figure 1.2(b), the alternator end shield is held up by three rods to the mechanical rear part of the alternator assembly. The three shield rotation positions tested here are essentially the shield rotated in increments of 120 degrees. Figure 4.10 shows the influences of this rotation. The similarity between shield positions two and three are quite evident, with only a 0.1 dB(A) difference in total power. Taking the 12th order as an example, an 0.4 dB(A) difference in results. It's clear from these results that, given the integral over ten microphones and that results are calculated in the far field, the radial rotation of the end shield with respect to the surroundings has a small impact on the sound emission from the generator.

The differences from both these to the shield position 1 results however is more significant. It should be noted that this test was conducted on a different day, and thus the results may be somewhat different due to small variations in the ambient atmosphere. In this case, total sound power level is up to 0.8 dB(A) lower, with the 12th order varying by up to 3.3(A) dB. The 8th order shows variations by up to 6 dB(A).

4.6.5 Effect of rib number

In determining the effect of rib number, the end shield with square ribs was used. The design B ribs were subsequently replaced with design A ribs (see Figure 4.3). For the two rib cases, the remaining two ribs are 180 degrees apart. Figure 4.11 shows the influence of the rib count on the results obtained. The results are shown at 8000 and 10000 rpm, in order to obtain a clearer view of the influenced spectra. It is clear that the higher clawpole orders are not influenced, once again since they are due to the interaction between the clawpole surfaces and the stator holes, this region being only marginally influenced by the downstream conditions. The greatest influence is clearly at the 12th and 24th orders, the first two blade passing frequencies of the fan blades.

From the discussion in Section 3.5, it is expected that a reduction in the number of ribs should shift the frequency concentration to lower orders, thus reducing the influence at the 12th order. Given that the energy of the sound across the frequencies tapers off away from the fundamental forcing order, it is also to be expected that the difference between the first two fundamental frequencies should be smaller when the forcing frequency is reduced. This occurs given that the central lobe is shifted to the left (due

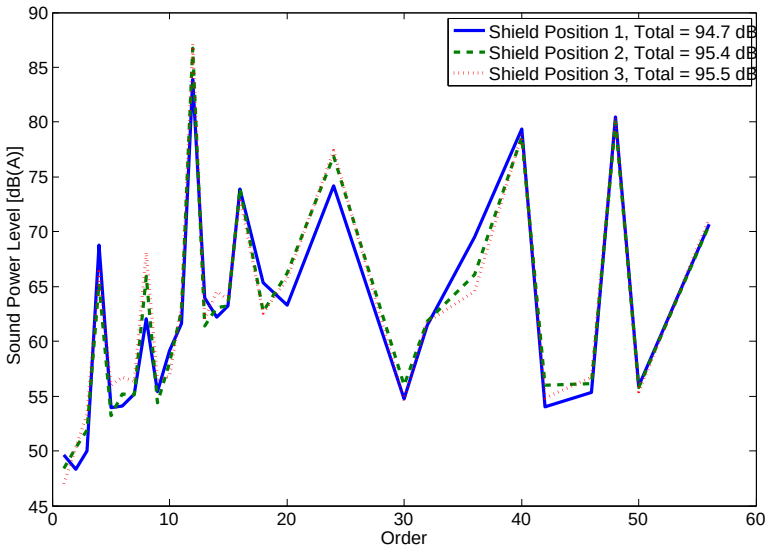

Figure 4.10: Effect of varying shield rotation on sound propagation at 10,000 rpm

Rib count	Speed [rpm]	
	8000	10000
1	6.1	4.0
2	5.2	7.0
3	6.1	8.7
4	10.9	9.7

Table 4.2: Difference between the first two blade passing frequencies (12th and 24th order) with a change in upstream rib count

to the reduction in fourth order excitation from the rib removal), further away from the fan blade orders which uniquely produce sound. This is discussed in detail in Section 3.5.

As evidenced in Table 4.2, this effect is particularly noted at 10000 rpm, where the difference between the first two orders is largest for the case with four ribs, and reduces with fewer amount of ribs. At 8000 rpm, the effect is more subdued, with this shifting tendency most notable for the comparison between the two, three and four ribs cases. What should be noted here is that the one rib case, rather than inducing a forcing akin to a first order harmonic, acts as a type of impulse. Also of note is that the three rib case, although fitting correctly to the theory here, does not truly represent a third order harmonic excitation, as the three rib case is essentially the four rib case minus one rib; the angles between the remaining ribs are still representative of a fourth order excitation (90 degrees). The effect here is more akin to a reduced fourth order forcing with an additional first order, due to the asymmetry at the missing rib.

A general reduction in the total sound power level is also noted, due to the overall reduction in flow disturbances with a reduction in rib count.

4.6.6 Effect of fan size

Two fan geometries were tested in order to determine their influence on sound spectra and power levels, shown in Figure 4.12. Both fan blades are based on typical fan blades used in Bosch alternators; low airflow fan blades used generally on the A-side of alternators, with high-airflow fans generally used on the rectifier side, due to the need to overcome higher pressure losses from the B-side electronics.

The effects of the two fan geometries are shown in Figure 4.13, for the case with no ribs obstructing

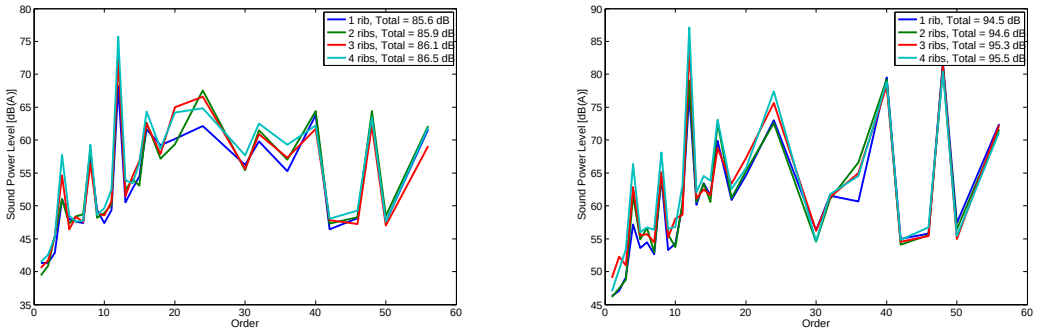

(a) 8000 rpm

(b) 10000rpm

Figure 4.11: Effect of rib count on sound spectra

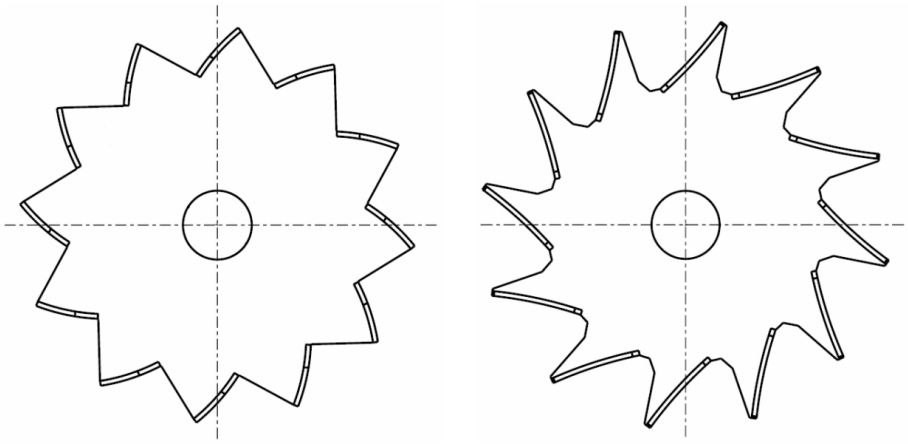

Figure 4.12: Fan blades tested; backward sweeped, low airflow fan (left) and forward sweeped, high airflow fan (right). Rotational direction is anti-clockwise

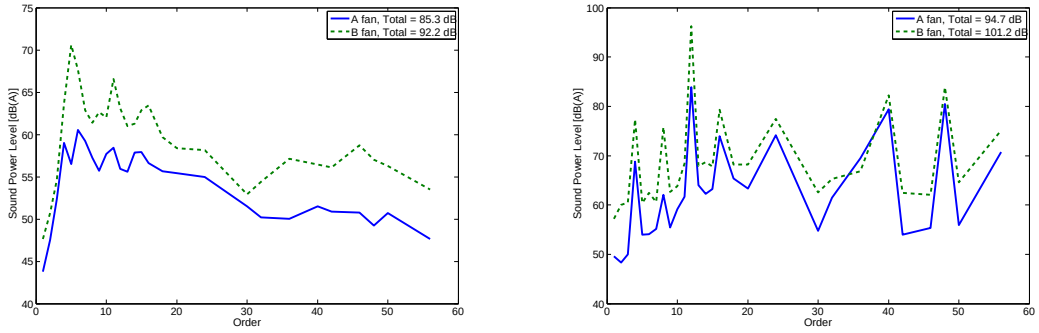

(a) No upstream disturbances, cylindrical clawpole

(b) Upstream disturbances, with clawpole

Figure 4.13: Effect of fan geometry on sound production at 10,000 rpm

the inlet flow and for a case with the total geometry; upstream obstructions in addition to clawpole structure. Quite clearly, the increase of the fan size has the general effect of increasing total noise, across the entire frequency range. There is some concentration of the sound energy of the B-fan at the 5th order when there are no upstream disturbances present, due possibly to incoherent turbulent structures entering the alternator thus causing uncorrelated forcing on individual blades. Much as the case with the smaller fan blades, there is no prevalent blade passing frequency present.

With the introduction of obstructions, a very large difference is noted between the two fan blades at all frequencies. The change in the 12th order is particularly noteworthy, over 12 dB(A), with a total sound power level change of 6.5 dB(A). The lower clawpole orders, the 4th and 8th, are also noted to change quite significantly. This implies, as mentioned in Section 4.6.1, the sensitivity of the clawpole roots to the impinging pressure forces from the fan blades, in addition to the general increase in broadband levels. The variations at the higher clawpole orders are not as significant, once again demonstrating that these local interactions are not very strongly influenced by upstream conditions. The general increase in sound power level over all orders, including minor orders between every fourth, implies additionally a noise increase due to a general increase in flow rate, which increases pressure amplitudes in the system, and also turbulence.

4.6.7 Sound power level dependence on rotational speed

As discussed in Section 2.3, the dominance of particular source types can be determined by observing the sound power level dependence on Mach number, which in turn is proportional to the rotational speed. In order to show this, results from the alternator with design B clawpoles and ribs (the reference geometry) are analysed, as this geometry includes all sources of interest. The logarithm of Equation 2.23 is written below, where the term $L_{W(d)}$ is in this case in the units of $\log_{10} P^2$.

$$L_{W(d)} \propto 6 \log_{10} M \tag{4.7}$$

Figure 4.14(a) shows the average solution of three measurements taken with this geometry. The curve is plotted once again, with the sound power level shown in $\log_{10}(\text{Pa}^2)$ and the speed in $\log_{10}(\text{rpm})$. A linear curve fitting is carried out between 4,000 and 12,000 rpm. The 95% confidence bounds of the gradient of this curve are calculated to be 5.947 to 6.043. This agrees very well with the M^6 dependency of sound power level for dipole sources from the theory discussed in Section 2.3, hence confirming that the aerodynamic sources of the alternator geometry are predominantly dipole in nature.

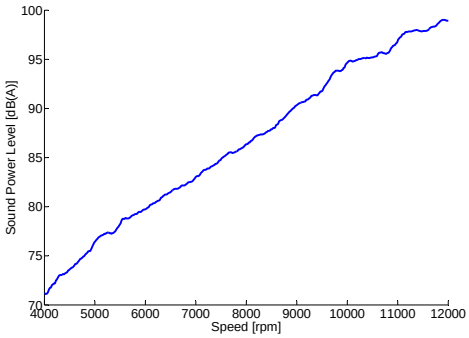

(a) Speed ramp of alternator with clawpole and rib designs B with low airflow fan

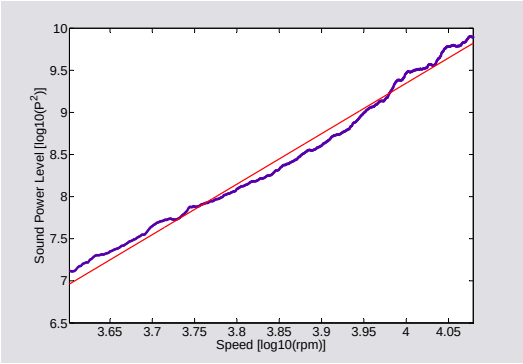

(b) Linear curve fitting of speed ramp

Figure 4.14: Determination of source dominance

4.7 9 microphone sound pressure tests

Further studies were conducted on the 9 microphone test bench at the research facility due to resource limitations at the ISO alternator test bench. Comparisons of results from the two measurement systems will not be carried out, given the differences between microphone positioning in addition to microphone distance to the alternator. Furthermore, the microphone positioning (either in a lateral or longitudinal plane, see Figure 4.2) are not adequate for measurement of sound power levels, such as those from the ISO test bench. For sound power measurements, the positioning of the microphones must be such that an approximation to an enclosed sphere must be represented.

In any case, the experiments conducted at the 9 microphone test bench investigate the effects of certain physical changes in the alternator, and from the theoretical concepts discussed in Section 2 and Section 3.5, provide an initial validation of the theory. Result analysis will be focused on logarithmically averaged values as obtained from the nine microphones used, thus giving a general indication of total sound energy changes. Specific analysis of sound directivity will be carried out in later sections for the purpose of computational comparisons.

4.7.1 Effect of blade number

Figure 4.15 shows typical results from the 9 microphone system. As discussed, an energetic summation is carried out over the 9 microphones in order to determine, as best possible with this microphone layout, a total sound emission spectra. For the purpose of comparing particular frequencies, order calculations are carried out at the main orders by integrating a band equal to 1 order around the corresponding order. For instance, at a speed of 12,000 rpm, the first order corresponds to 200 Hz ($\frac{12000}{60} = 200$), the 12th order corresponds to 2,400 Hz. Thus, the energy content at the 12th order is the integral of the power spectra between 2,300 Hz and 2,500 Hz. Total sound power levels are shown in the results as straight lines across the spectra.

Figure 4.15 shows the influence on the sound at all orders due to a change in blade number from 12 symmetrical to 8 symmetrical fan blades. The fan blade geometry is left otherwise unchanged. The geometry used in these experiments is the full geometry with clawpole structures; the influence from these clawpoles alone is clearly observed at the higher orders where the change in fan blade number does not have a significant impact. This is to be expected from the analysis conducted in Section 4.6.2, where the higher clawpole orders were seen to change only slightly (no more than 3 dB at 10,000 rpm) with the introduction of the fan blades. Results here are analysed at only 10,000 rpm.

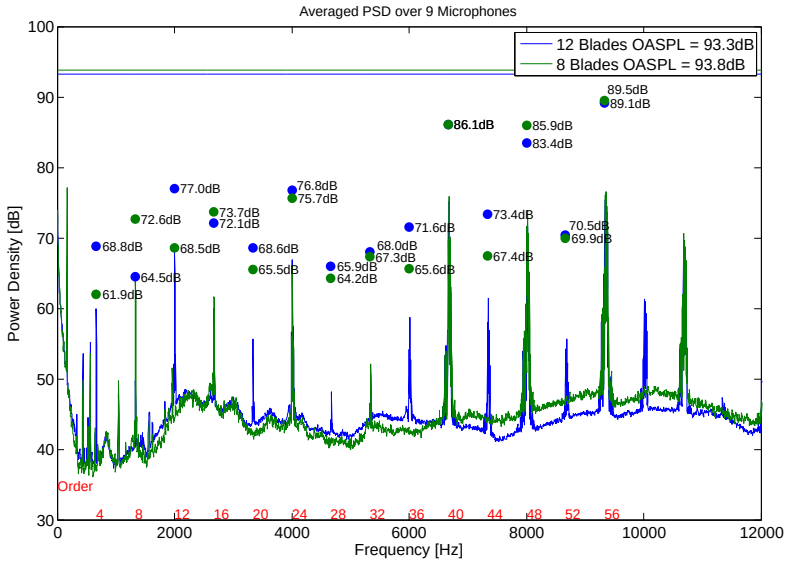

Figure 4.15: Effect of blade number at 10,000 rpm

Due to the change from a symmetrical 12 bladed fan to a symmetrical 8 bladed fan, a clear shift of the blade passing frequencies is evident in Figure 4.15. The change from a twelve bladed fan to an eight bladed fan reduces the 12th order by 8.5 dB to a level representative of broadband noise (the peak in the power density is no longer present at the 12th order); the 8th order rises by a similar level. Changes to other fan associated orders are less evident; the 16th order is only slightly higher with the 8 bladed design due to the dominance of that order from the clawpole geometries (as noted in Figure 4.6), while the 24th order has both an influence from the 12 bladed fan (the second blade passing harmonic) as well as the 8 bladed fan (the third blade passing harmonic). The 36th order, on the other hand, has a strong peak with only the 12th bladed fan having an influence, from it's third blade passing harmonic. Focusing on the spectral density (and not the integrated orders), it is clear that the 12 bladed geometry produces peaks at every 4th order, while the 8 bladed geometry produces strong peaks at every 8th order. This confirms the previously stated theory that the 12 bladed alternator produces an asymmetry at the rotor, thus exciting, even at the higher, clawpole dominant orders, every 4th instead of every 8th order (for example, the 44th and 52nd orders).

The general level of the broadband noise can be clearly seen by observing the spectral density line. Closer observation of the integrated orders at regions without sound peaks indicates the contribution at the harmonics from only broadband noise. For example, integrating the 12th order for the eight bladed system, in addition to other similarly less affected frequencies, for example, the 36th order for the same fan blade. Here, although no peaks are present in the spectra density to signify the onset of a tonal noise, due to the integration of the broadband noise alone, the order is calculated as approximately 65 dB.

4.7.2 Casing holes and the influence of sound

In order to demonstrate the effect of the hole number in the casing, a geometry was constructed that contains half the number of holes as the reference geometry, each hole being twice as large. In effect, the total outlet area for the fluid remains constant, while the number of holes is changed, in order to ensure that the outlet area remains constant, and thus has little effect on mass flow in the region.

Figure 4.16 shows the influence of the sound generation due to the modified number of casing holes, and it is quite clear to see that, whereas with the reference 48 holes geometry the clawpole sound was centred at these higher orders (the 40th, 48th and 56th orders), the 24 hole geometry generates sound

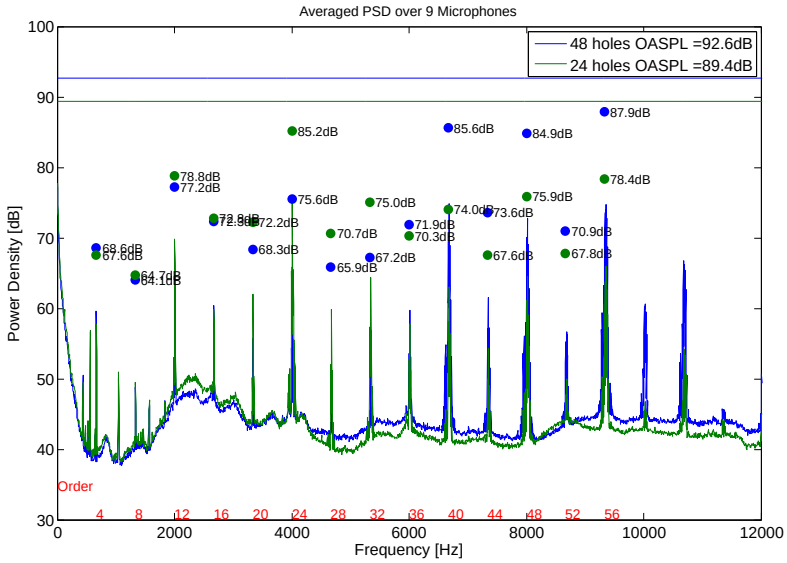

Figure 4.16: Effect of hole number on the sound generated at 10,000 rpm

centred at the 24th order and the clawpole sidebands ±8th orders. A small increase in sound is also noted at the 12th order for the 24 hole stator; this is not due to an increase in the fan generated sound, but is rather due to a harmonic from the 24th order excitation modulated at $\pm 8n$ clawpoles. Once again, this confirms the influence that certain excitation frequencies have on the noise generated, in addition to the harmonics they effect, as was discussed in Section 3.5.

A direct comparison to the main excitement frequency and the two ±8 side orders is shown in Table 4.3. The main excitement order is very similar for both the 24 and 48 hole cases, with only a 0.3 dB difference noted. For the side harmonics, the 24 hole geometry produces much less energy, both the left and right side harmonics being over 10 dB lower in level than for the 48 hole case. Quite clearly, higher excitement frequencies tend to modulate a greater amount of energy onto the side orders. This finding was also clearly demonstrated in Figure 3.5(a). The difference in total sound generated is quite large, the 24 hole stator producing almost 3 dB less averaged sound pressure over the 9 microphones. This was also noted in the theory of Section 3.5.

Stator	Left harmonic [dB (Order)]	Main harmonic [dB (Order)]	Right harmonic [dB (Order)]	Total [dB]
24 holes	72.8 (16)	85.2 (24)	75.0 (32)	89.4
48 holes	85.6 (40)	84.9 (48)	87.9 (56)	92.6

Table 4.3: Influence of stator openings on the main clawpole order and sidebands; the order number is shown in brackets

4.7.3 Effect of selective closure of casing holes

In order to examine the correlation between excitation frequency and noise generated in the alternator further, the reference geometry was used as basis to determine the effects that closing selected openings in the casing has on the sound generation, and, in particular, the sound orders typically associated with the clawpoles. Figure 4.17 shows an example of configuration E, with the closure of every 6th hole in order to excite an 8th order forcing on the clawpole surfaces.

Several configurations were tested with the intention of exciting particular orders generated at the

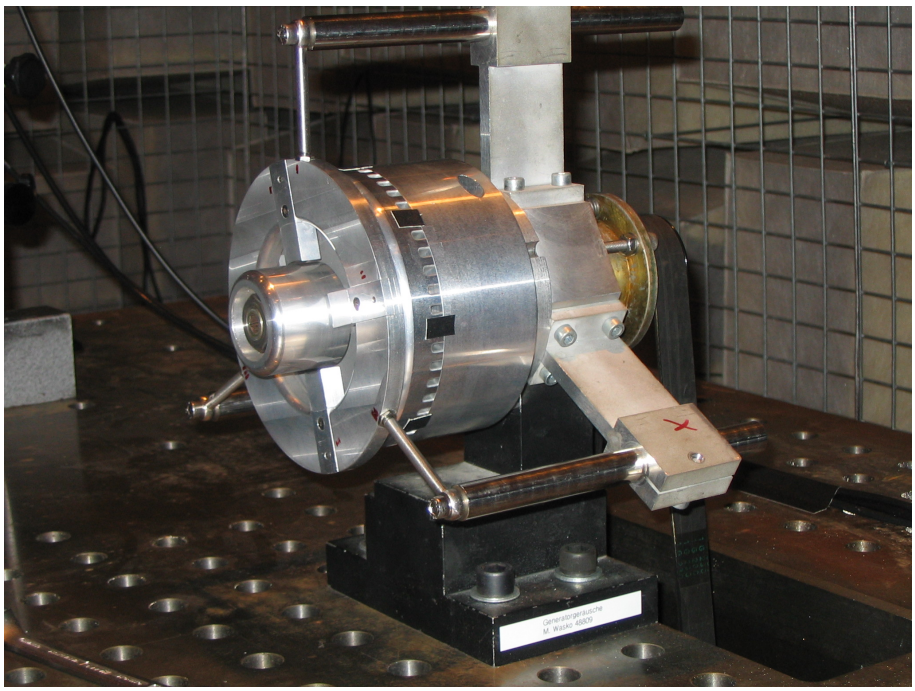

Figure 4.17: Closure of several casing holes to excite lower orders; configuration E

clawpoles.

Configuration A (All open) The reference geometry, with all 48 holes left unchanged.

Configuration B (1 closed) The closure of only one of the 48 holes. This has the effect of introducing a short pulsation at individual clawpoles at the time of passing the closed opening.

Configuration C (3 consecutive closed) The closure of three consecutive holes, which has the effect of closing the holes that constitute a full claw finger width. In effect, during one full rotation, there will be eight instances where a clawpole experiences a closed stator region. This should create a similar physical effect as Configuration B, albeit over a wider region.

Configuration D (3 equally spaced closed) The closure of three equally spaced holes (every 16th hole closed), which rather than introducing an impulse type signal, should introduce a third order fluctuation.

Configuration E (8 equally spaced closed) The closure of eight equally spaced holes (every 6th hole closed), which has the effect that whenever a claw finger is positioned below a closed opening, all clawpoles are positioned under a closed opening. In effect, this produces a rotor/stator symmetry.

Configuration F The closure of all openings

By selectively closing certain holes, it is expected that a certain frequency component can be modified in the clawpole orders, which entail every 8th order. Figure 4.18 shows the results of these measurements, and indeed a very large influence is noted at the first clawpole order, the 8th order, in addition to clawpole orders below the 40th.

With the reference geometry, which has 48 equally spaced and sized holes, it has been shown that the pressure fluctuations on the surfaces will be predominantly of a 48th order, with harmonics at $\pm 8n$ orders. By blocking off three consecutive holes (configuration C), a much lower frequency is introduced into the pressure fluctuations experienced at the rotor surfaces; although not necessarily predominantly first order given the impulsive nature of the disturbance, the frequency content must be, in any case,

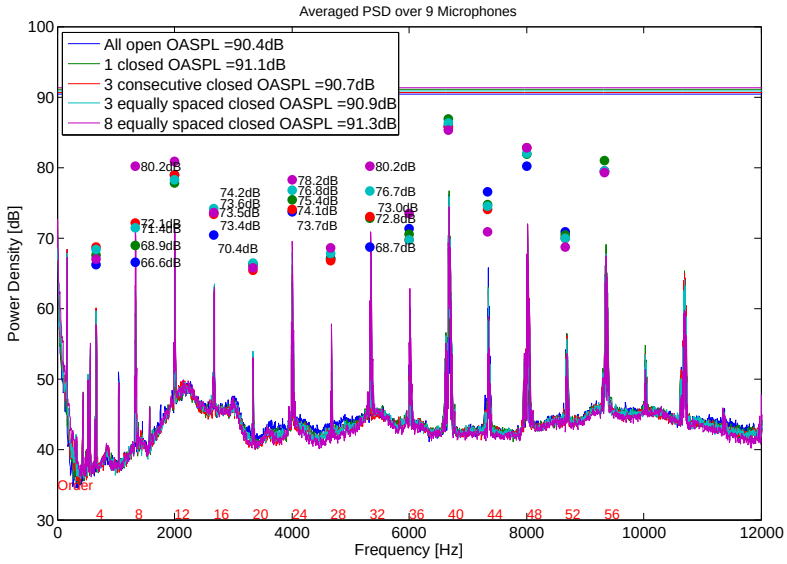

(a) 10,000 rpm

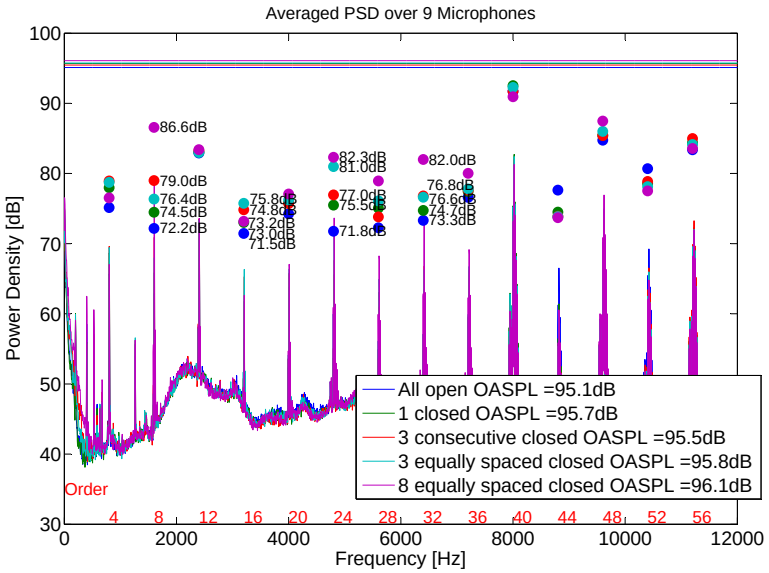

(b) 12,000 rpm

Figure 4.18: Effect of closing a number of holes in varying patterns

lower than that produced by 48 equally spaced holes. This excites lower orders. At both 10,000 rpm and 12,000 rpm, the first three orders of this variant are strong compared to the other geometries (except the 8 equally spaced geometry). Comparing this to the variant with only one hole blocked (configuration B), a similar tendency is noted, albeit slightly subdued.

The closure of three equally spaced holes (configuration D, in effect, a star shaped closure) influences higher orders in comparison to configuration C, as the forcing frequencies on the rotating surfaces are of a higher order (a predominantly 3rd order in comparison to a lower 1st order). This is the case at both 10,000 and 12,000 rpm, where the three consecutive closed holes generally have somewhat more energy up to the 8th order. From the 24th order, the 3 equally spaced closed produces more sound energy.

In essence, it is clear to see that, with respect to the clawpole orders, if the disturbance contains lower spatial orders, so to will the lower sound orders be influenced. For the case where three consecutive holes are blocked off, which in turn will induce a lower forcing order in the region, it is clear that the 8th order will be strong, while the higher orders, such as the 24th and 32nd, will be weaker.

It is however clear that, with the closure of eight equally spaced holes, the total sound power level becomes the greatest as do the majority of the clawpole orders between the 8th and 32nd. From the discussion in Section 3.5, it is clear that the maximum contribution to sound will occur when the harmonic of the disturbance is equal to the number of surfaces. Therefore, the 8th order will be largest when eight surfaces undergo a forcing fluctuation of the 8th order. Given that the forcing frequency will not be of purely 8th order, but also contains harmonic content (a 16th, 24th, 32nd etc), it can be stipulated that those harmonics will also have their strongest contributions to the sound at those orders. Together, one would therefore expect that most of the sound orders will increase significantly when a forcing frequency equal to the number of surfaces is introduced.

Discussion has been focused on the lower orders here, simply because they are the weakest in the reference geometry case, and are therefore more easily excited. It is clear that the higher clawpole orders (40th, 48th and 56th) remain quite unchanged with the various closing of the holes; in any case the differences are not as significant as those, say, by of 8th order. The reasoning for this is that, even with 8 holes closed, a large portion of the holes remain, and those that do have an angular distance to each other still representative of a 48th order ($\frac{360}{48}$ degrees). This ensures that the energy content at the higher orders changes only slightly, while the added energy to otherwise weaker orders are more strongly influenced.

The final comparison in Figure 4.19 shows the sound influence of closing all holes in the geometry. With respect to the rotor/stator interactions, this has the effect of removing high frequency fluctuations on the 8 clawpoles. The effect on the sound generation is significant at higher orders, with the energy content at orders higher than the 40th being strongly weakened. Lower orders however indicate a slight increase, in particular the 8th and 12th orders. By closing all holes, a static pressure rise occurs at the inner casing walls due to removal of a part of the outlet, in essence increasing the local average stagnation pressure at the inner casing, this in turn propagating a higher pressure region onto the clawpoles. CFD calculations have shown that the mass flow coming out of the casing holes can account for approximately 37% of the total airflow. Obstructing this mass flow by closing the outlet is the source of the static pressure rise that increases the lower orders. Overall however, given the dominance of the reference geometry at the higher orders, the removal of the holes reduces the total averaged sound pressure level by almost 8 dB due to the overall reduction in pressure fluctuations in the system. This is akin to the reduction of sound due to the removal of upstream ribs (Section 4.6.1), and once again shows the significance that pressure fluctuations have in the system analysed.

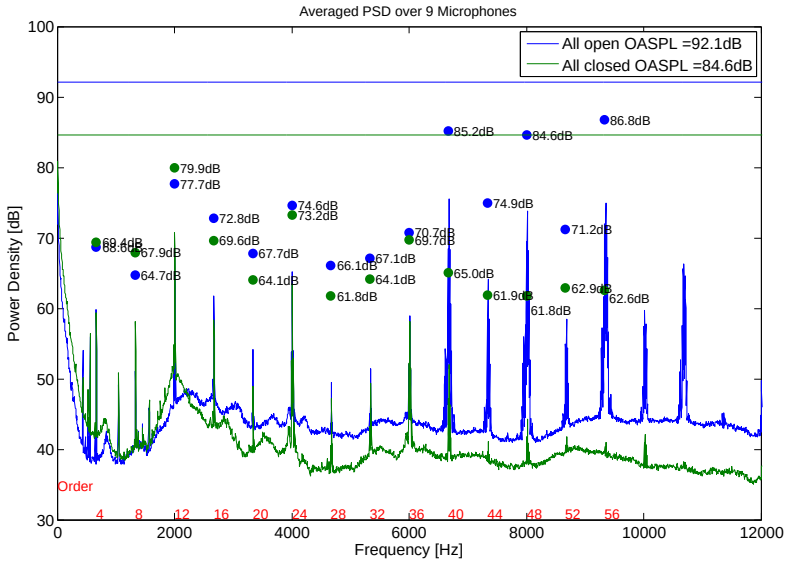

Figure 4.19: Effect of closure of all casing holes at 10,000 rpm

4.7.4 Claw geometry modification and its influence of sound generation

From the previous studies, it has been shown how various geometry changes have the influence on the creation of various clawpole orders. The studies with the closure of casing holes suggests strongly that these clawpole orders can in effect be altered with both the systematic changing of the stator, in addition to small changes made to the clawpole geometries (for example, clawpoles with the leading edge rounding at the root surface); in effect, any geometrical change that has an influence on the rotor/stator interaction.

The intention in this section is to show how, with the creation of a particular sound, other measures may be taken to once again modify that source. Using the closure of the holes as an example, it is quite evident that with selective closure of the holes, lower orders can be stimulated due to the introduction of a lower order forcing on the eight clawpole surfaces. In particular, the strongest interaction occurs in the exact region where the clawpole surfaces are closest to the casing. The theory would then suggest that, if the clawpole surfaces were to be bridged exactly in the region where this low order forcing occurs (due to the closure of selected casing holes), the lower orders influenced by this closure would once again be reduced. A significant reduction would also occur at the higher orders, given that the region producing these higher orders is the same. From a perspective of a rotating frame of reference, in bridging the rotating surface there are no multiple surfaces and thus no particular clawpole orders should exist due to interactions in this region (incidentally, much like the cylindrical clawpoles of Section 4.6.2). This was tested by simply covering the clawpoles in the region where the casing holes are prevalent with masking tape, shown in Figure 4.20(a).

Figure 4.20 shows the influence of this partial closure (labelled in the figure as a band) on the stator with 8 closed holes (configuration E) and the reference rotor. The results clearly show that the creation of lower order clawpole sound is due not only to the stator's influence of inducing a lower order forcing on the surfaces from the closure of every eighth hole, but also the number of surfaces themselves in the region of the predominant forcing; as previously stated, the coupling of an 8th order excitation on eight surfaces. The 8th order, for example, reduces by over 12 dB due simply to the partial closure of the surface. The reduction of the 8th order is not to the level of broadband noise, as the fan blades themselves produce pressures on the clawpole roots, in addition to static pressures on the top clawpole surface. Higher orders are also noted to be significantly reduced by over 15 dB. Although the stator holes are still present in this geometry, the fact that they are interacting with one continuous rotor surface means that those

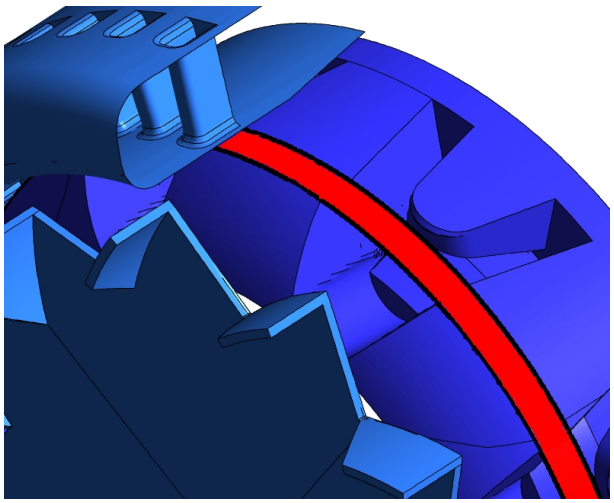

(a) Geometrical modification of clawpoles

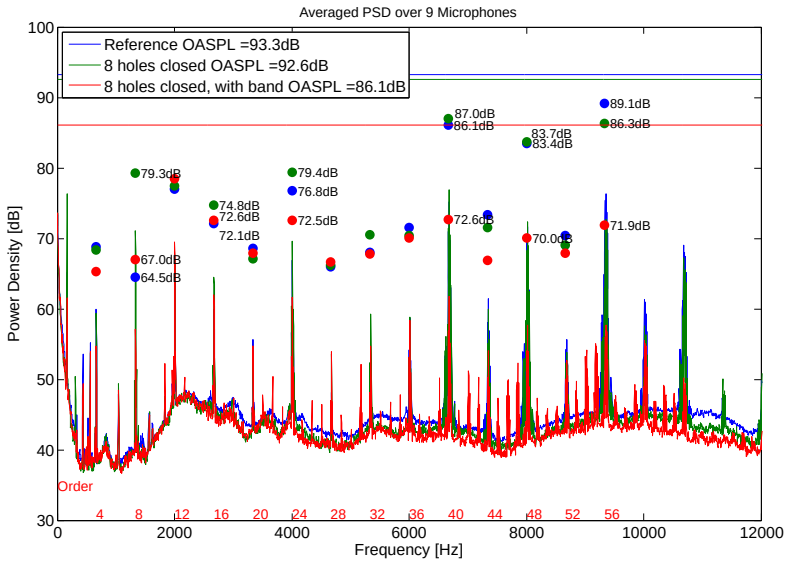

(b) Sound impact

Figure 4.20: Effect of partial closure of the clawpole surfaces

interactions are stationary. Parallels once again can be made with the clawpole cylindrical structure.

Of note however are sharp, but relatively weak, orders occurring at the high frequencies. These have a very small effect on the total sound level, and are due most likely to the fluttering of the masking tape during rotation. In any case, one sees that a simple partial closure of the rotor produces significant results when such a closure occurs in the regions where the largest fluctuations occur; in this instance, opposite the casing openings.

4.8 Summary

The preceding section has outlined the measurement procedure carried out within this work. The purpose of the measurements were twofold. Firstly, as a basis for validation of the code developed for numerical aeroacoustic calculations, which will be covered in the following section. Secondly, in order to determine fundamental interactions in the system, which also can be used to validate the theory of Lowson in a simplified sense.

From the measurements, it was found that the removal of key interactions in the rotor/stator system, which cause pressure fluctuations, had a very significant influence on the total sound energy generated. Removal of the inlet ribs was shown to reduce sound power levels by over 6 dB(A), implying that the pressure fluctuations occurring at the blades can increase the total sound energy by a factor of up to 4. This significant reduction due only to the ribs also implies the dominance of the rotor sources on sound production; the addition of upstream ribs only influences the flow entering the rotor, and hence the pressure changes occurring on the rotor surfaces. For the case of the clawpoles, the pressure fluctuations due to the interactions between the clawpoles and the holes in the casing can contribute up to 8 dB to the total sound energy produced. These investigations once again confirm the need in considering the pressure transients in the alternator system, discussed in Section 2.4.1. Analysis carried out over a typical speed ramp showed also the dependence of the sound on the 6th power of the Mach number, thus proving the dominance of the dipole as a source of sound. This indicates the appropriateness of using a transient method that considers only dipoles as the chosen method for acoustic calculations. Lowson's method satisfies this requirement.

General studies were also conducted in order to determine geometrical influences on spectral distribution of the sound. It was found that, as shown in Section 3.5, the dominance of particular orders is characterised by the forcing frequency acting on the rotating surfaces. The orders that have a significant sound contribution is dependant on the rotor surfaces; if symmetry prevails, than only those orders and harmonics thereof related to the symmetry will have strong contributions that are above the level of broadband noise.

Chapter 5

Numerical results and experimental validation

Having covered the implementation of the technique for the calculation of aeroacoustic sources and their propagation in Chapter 3, focus will now be placed on results pertaining to the actual generator model. These results will have a focus on the CFD calculations carried out, in addition to the sound calculations carried out numerically using the code based on Lowson's equation. The fluid dynamics and acoustics of two configurations will be analysed, these being the full geometry with clawpole surfaces in addition to the geometry without clawpole surfaces. These geometries are most relevant for the alternator application; the full geometry represents well the alternator system and the main aeroacoustic noise sources, while the geometry without fan blades can be used to estimate the noise sources alone from the clawpole fingers. The chapter will conclude with a calculation used from a real application in order to appraise the applicability of the tool in industry.

5.1 CFD simulation details

From Section 2.4.1, in addition to several measurements discussed in Section 4, the necessity to capture transient changes to surface pressures for geometries with even minimal upstream disturbances yields, subsequently, the requirement to model the instationary flow. It has already been shown that these transients can influence total sound pressure and power by up to 8 dB, in addition to being essentially the sole mechanism that produces tones for the simplified alternator geometry. These transient numerical results will be highlighted throughout this section. Stationary simulations will not be thoroughly analysed, as their purpose was to provide an initial estimate of the flow field in order to ensure quicker convergence of the transient simulation. The actual results of the steady state simulations were not always converged to provide an accurate solution, but rather to provide a good initial fluid solution for the transient computations. Given this, analysis will be limited to solutions of the transient simulations, with particular emphasis placed on regions of significant fluctuations. From this, an analysis of the fluctuating surface forces will be carried out, in order to provide the necessary input into the acoustic formulation.

The mesh constructed for the reference model consists of 2.5 million hexahedral elements; of these 2.5 million elements, 1.3 million are used inside the rotor domain. The constructed mesh consists of four separate assemblies: a fan blade assembly together with a clawpole assembly models the rotating domain while separate near field and far field assemblies model the stationary domain. In the stationary domain, the near field assembly models the stationary components while the far field domain was used to mesh the fluid out into the outer opening boundary condition, the size of which is 3 alternator diameters. Figure 5.1 shows the mesh and geometry of the reference one-quarter model. For the model without

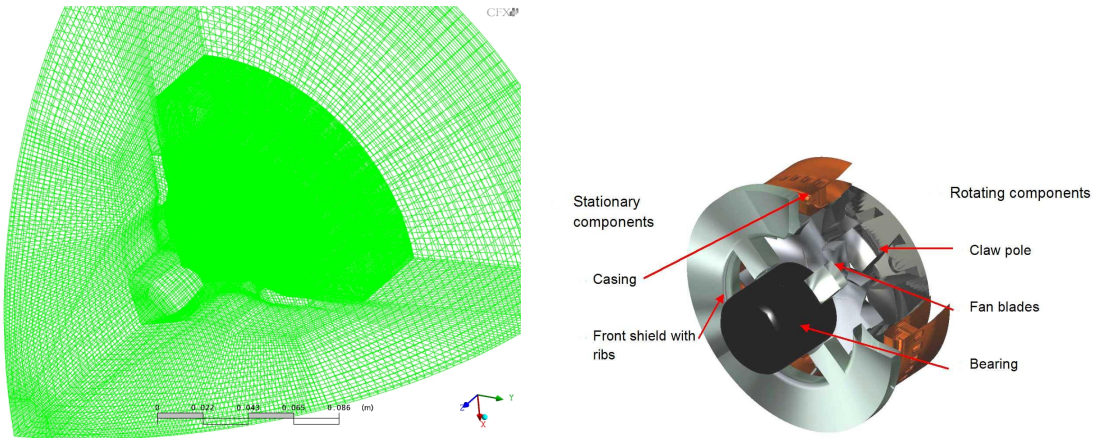

(a) CFD mesh of reference model

(b) CFD geometry of reference model

Figure 5.1: CFD mesh and geometry of reference model

fans, a one-eighth model was constructed, as the fan blade no longer restricted the need for a one quarter model. The mesh constructed consists of 780,000 hexahedra elements. Similar boundary conditions were placed on key surfaces and interfaces for both models.

The fan and claw-pole assemblies are modelled as a rotating domain with a particular rotational speed. The two models discussed herein were carried out at 10,000 and 12,000 rpm. Although experimentally, in particular at the ISO test bench, wider speed ranges were measured, only at these higher speed levels is the aerodynamic noise dominant over possible mechanical noise components, such as bearing noise. Sound curves as shown in Section 4 over the speed were seen in this region to have a well behaved progression, with no resonance peaks noted that would otherwise suggest a non-aerodynamic behaviour.

The stator and environment assemblies are stationary domains. All meshes created for the various geometries are constructed using a hexahedral blocking scheme. This scheme involves constructing each of the assemblies through a number of blocks, each constructed such that it represents the underlying structure. Such a meshing scheme allows accurate control of mesh quality and permits the use of a predominantly hexahedral mesh, which is known to produce more accurate results when compared to a similarly fine tetrahedral mesh [7]. In such a scheme, cells can be aligned in the flow direction, thus resolving velocity and pressure gradients accurately.

In order to connect the several assemblies, domain interfaces need to be defined between assemblies. In regions where two stationary assemblies are joined, a simple fluid to fluid domain interface is used, whereby flow variables are simply transferred between the two assemblies. In this instance, GGI interfaces are used. These connections use an interpolation function in the event that node placement between surfaces is not one-to-one. Periodic interfaces function in a similar fashion, whereby data is transferred across the surfaces defining the interface. Periodic interfaces are used in order to relate one side of the generator mesh to the other; in the quarter model case, this involves the transfer of data at the 0 and 90 degree surfaces, shown in Figure 5.2. This allows a reduction in modelling requirements, as only a symmetrical part need be modelled. Where possible, periodic interfaces were constructed such that one-to-one interfaces, instead of GGI interfaces, were used. This negates the need for interpolation schemes, as a direct connection exists between the relevant nodes.

Domain interfaces between rotating and stationary components are more complex. For the stationary flow simulations, a combination of frozen rotor and stage interfaces are utilised. Stage interfaces generally produce a better approximation of the average flow through a system as the flow variables are circumferentially averaged at the interface thus taking into account time averaging effects [24]. However, they are not appropriate in regions where the circumferential change in flow variables is large compared to the

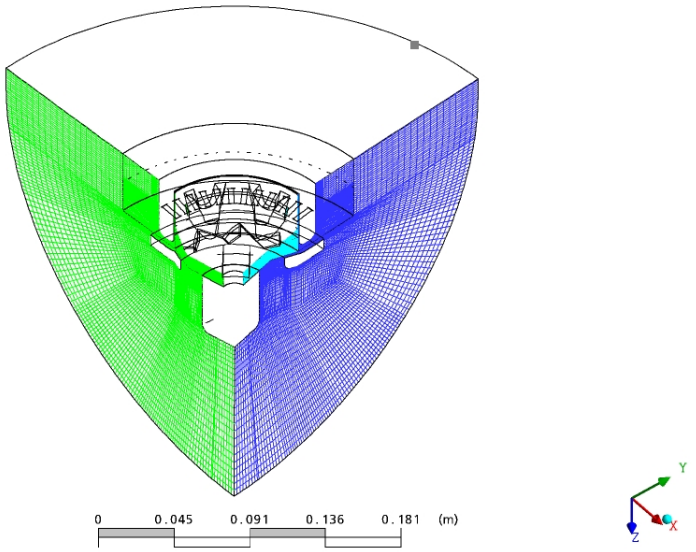

Figure 5.2: Periodic boundary condition mapping the two rotational ends of the alternator (blue and green)

component pitch. This is the case between the clawpole and stator structure, whereby the interactions between the flow and ventilation holes results in a rapidly changing circumferential solution. Attempts at simulating the interface as stage failed, thus the need to use a frozen interface. A frozen interface models the interface at a fixed relative position, thus modelling the interaction between the two structures. However, this produces a poor 'mean' result as transient interactions are not taken account of. For the full transient simulation, a transient rotor-stator interface is used whereby the relative position of the components is updated for each time step and full interactions are modelled.

With regard to surfaces, all surfaces are modelled as non-slip walls. The surfaces enclosing the entire geometry include the two periodic surfaces in addition to the outer surface and that at the rear of the alternator. These two latter surfaces are modelled as openings, whereby only a relative pressure condition is specified. This allows the flow to both enter and leave the boundary.

Given the resource requirements of simulating turbulence structures consisting of a large amount of scales, a turbulence model mated with the Reynolds Averaged Navier Stokes (RANS) equation has been utilised. The RANS equations modify the flow parameters of the Navier Stokes equations in order to include mean and fluctuating components. In doing so, more unknowns are introduced into the set of solved equations. These equations are then solved by utilising certain statistical assumptions in order to model the turbulence quantities.

For this work, the SST (Shear Stress Transport) eddy viscosity $k - \epsilon$ turbulence model has been utilised given its accuracy in predicting separation. An analysis of various turbulence models is not carried out in this work, but literature indicates that the SST turbulence model generally provides an adequate solution to problems that involve complex flows and separation [6]. Experience using the model at Bosch for similar multiple frame of reference applications has also been positive.

Surface forces on key surfaces, such as blade surfaces and claw-pole surfaces, were monitored during the transient runs in order to determine the convergence of a simulation. Once surface forces displayed well behaved periodicity for each quarter rotation (or one-eighth rotation, as the case for the system

without fan blades), the solution was assumed to be converged. This took, in general, between 2 to 4 full rotations (for the quarter model, this means 8 to 16 cycles through the domain). Once converged, the last cycle (one quarter or eighth rotation for the quarter model and one eighth model respectively) was used with the assumption that the force time history is infinitely periodic.

A high resolution advection scheme has been used throughout, in addition to a second order backward Euler scheme for transient computations. For the transient computations, up to ten coefficient loops were required per time step calculation in order to achieve a target residual RMS value (for both the mass and momentum equations) of 1×10^{-5} per time step.

Simulation time for the 2.5 Million element geometry was, using 20 Pentium 4 XEON 2.4 GHz Cores (Quad Core Processors) with 4 GB RAM, approximately 45 minutes per time step; 2000 time steps per full rotation and 2 full rotations results in a simulation time of over 3000 hours (over 4 months simulation time). The 780,000 element geometry (without fan blades) was carried out on 6 cores also at 2000 time steps per full rotation; in this instance, 3.8 full rotations were required for convergence. At approximately 33 minutes per time step, this resulted in a simulation time of over 4000 hours (close to 6 months computational time).

5.2 CFD results and noise generation mechanisms

The following section will focus on the reference geometry, which consists of the lower airflow fan blade, coupled with the 8 finger clawpoles without chamfers. The stator geometry consists of the housing with 48 holes, in addition to the upstream square rib obstructions. From the preceding analysis in Section 4, it was clear that several main noise mechanisms exist in the alternator that account for the aeroacoustic sources discussed in detail in Section 2. It is clear that, for the reference geometry, significant rotor stator interactions occur at both the fan blades in addition to the clawpole surfaces. The fan blade interactions were shown to cause noise predominantly at every 12th order, while the sound energy from the clawpole interactions was predominantly at orders 40, 48 and 56.

Figure 5.3 shows the pressure changes on the high pressure surface of one fan blade over time. Clearly, as the fan blade passes the local obstruction, large pressure changes occur on the surface of the blade. This also occurs on the suction side of the blade. Local to the rib, flow conditions change causing a subsequent change on the pressure induced on the fan blades. Figure 5.4 shows how the inlet obstruction alters the local flow. Flow streamlines in the region indicate changes in the flow direction; an acceleration also ensues locally. These changes in local flow have the effect of causing changes on the integrated surface pressures (the force) as the fan blade passes, shown in Figure 5.4(c). As the fan blade passes directly behind the obstruction, the largest force changes occur.

Figure 5.5(a) shows the pressure contours of the fan blades and clawpoles. In order to clearly show the relative positions of the fan blades and clawpoles, the results are copied and rotated to represent a full 360 degree result. As has been discussed in Section 4, the pressures and local flow generated at the fan blades influences the root surfaces of the clawpole fingers. The fan blades tend to cause a local pressure drop due to the accelerating flow between the clawpoles and the fan blade, seen in Figure 5.5(b). Further away from the fan blades, a general rise in pressure is noted. This is due to two mechanisms; firstly, the high pressure generated at the top surface of the fan blade impinges onto the clawpole roots. Secondly, this is also due to the stagnation region generated at the stator flow exit. Figure 5.5(c) shows how these high pressure regions interact with the clawpoles through manner of pressure iso-surfaces at 400 Pa. A high pressure field is generated at both the leading edge of the fan blades as well as at the stator exit.

Figure 5.6 shows the change in clawpole forces over time. In this analysis, the time steps are smaller than that of Figure 5.3 in order to capture the changes occurring as the clawpole surface moves past the stator holes. On the clawpole surfaces opposing the holes, a pressure rise occurs due to local airflow stagnation at the holes. This stagnation pressure impinges onto the rotor, causing a high frequency, 48th order fluctuation. This fluctuation is of particularly high amplitude at the leading edge of the clawpole, where additional stagnation of the flow occurs. The fact that, as shown in Section 4.6.2, a significant noise reduction occurs when a chamfer is added in this region is due to the chamfer reducing the severity of the flow stagnation in a region where large fluctuations prevail.

Figure 5.7 shows in more detail the stagnation region that occurs at the individual casing holes. Due to the rotation of the clawpoles, a local boundary develops at the top of the clawpole surfaces. This generated flow, upon coming into contact with the casing hole outlets, stagnates and thus generates a high pressure region. This region then influences the pressure distribution on the top clawpole surfaces. At the right of the casing hole, the local flow conversely accelerates, generating a local low pressure region which also impinges the opposing clawpole finger. These two mechanisms generate the high and low pressure regions that occur on the clawpole top surfaces.

As discussed in Section 4, the removal of the casing holes greatly reduces the high clawpole sound orders for the reason that these local interactions do not occur. A similar phenomenon occurs when, rather than the eight clawpole fingers, a cylindrical rotor is used. Although in this instance these high and low pressure regions also occur, they do so on a rotating surface that has no discontinuities. In effect,

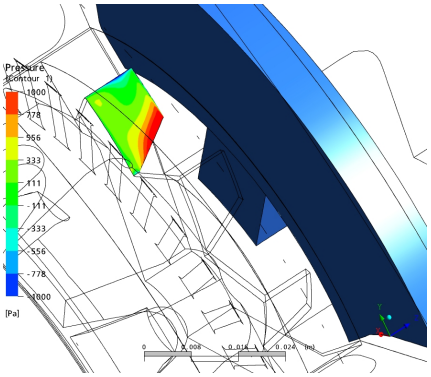

(a) Fan blade pressure, t = 8.7625×10^{-3} s

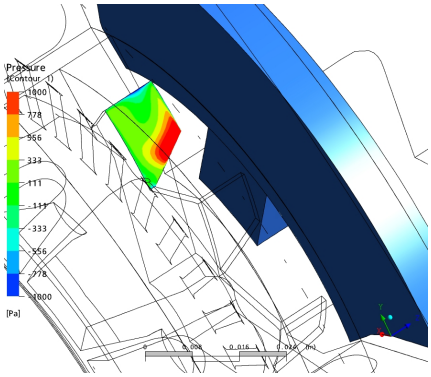

(b) Fan blade pressure, t = 8.885×10^{-3} s

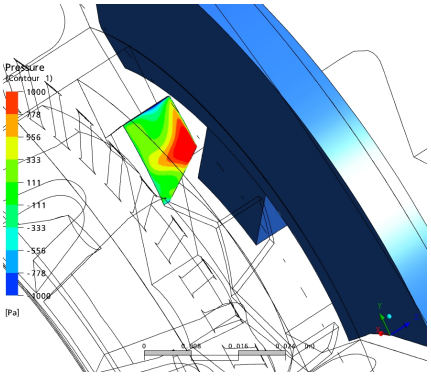

(c) Fan blade pressure, t = 8.9375×10^{-3} s

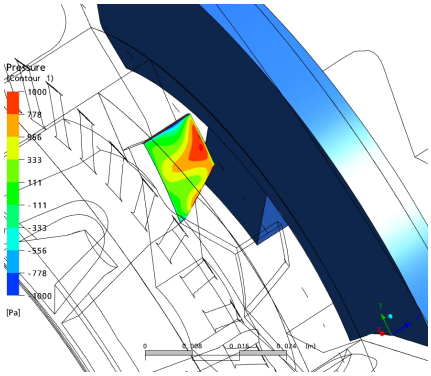

(d) Fan blade pressure, t = 9.025×10^{-3} s

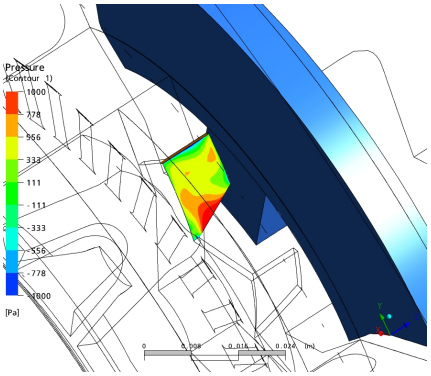

(e) Fan blade pressure, t = 9.1125×10^{-3} s

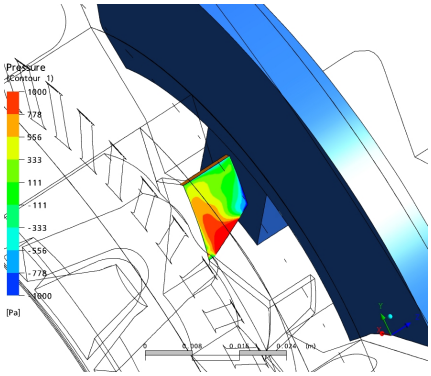

(f) Fan blade pressure, t = 9.2×10^{-3} s

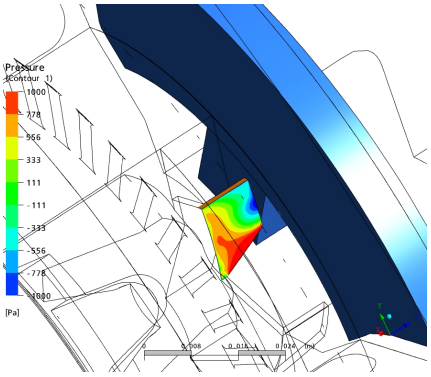

(g) Fan blade pressure, t = 9.2875×10^{-3} s

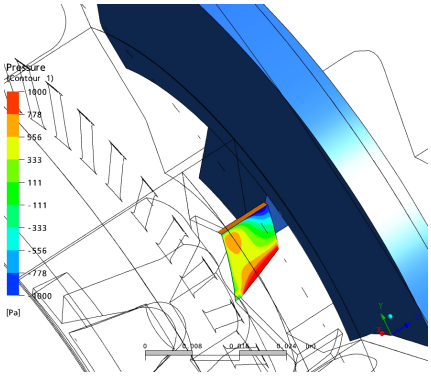

(h) Fan blade pressure, t = 9.3749×10^{-3} s

Figure 5.3: Pressure changes on fan blades over time

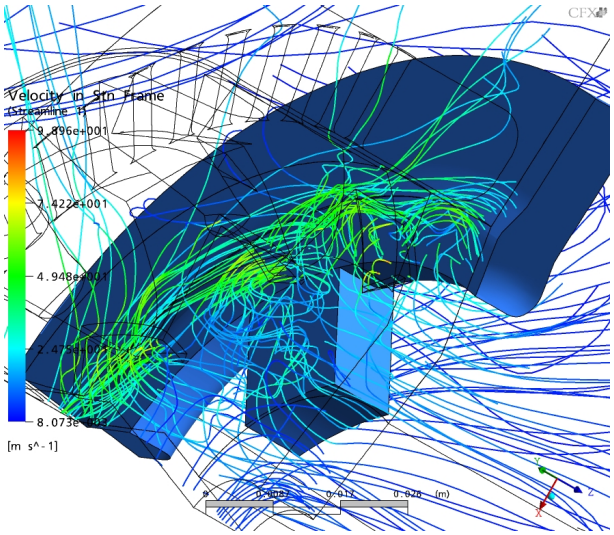

(a) Streamlines of airflow around rib

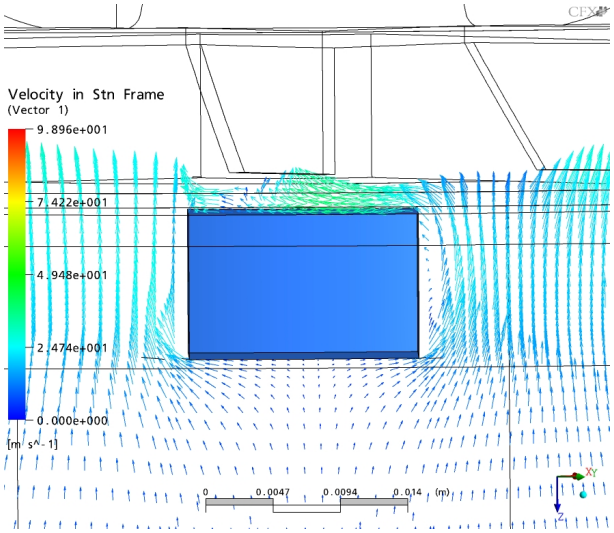

(b) Velocity vectors of inlet flow around rib

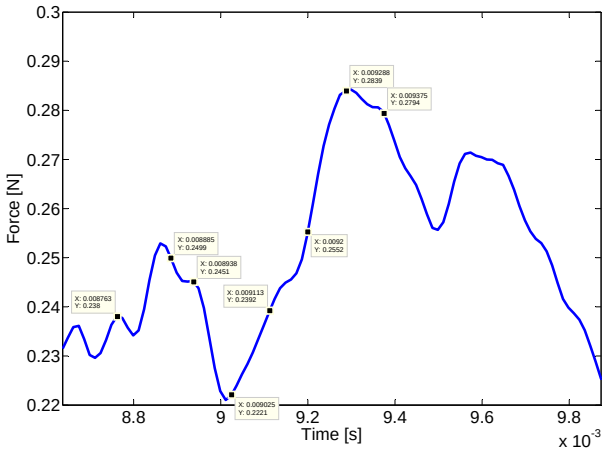

(c) Total force acting on one fan blade over time

Figure 5.4: Local flow effects due to inlet obstruction

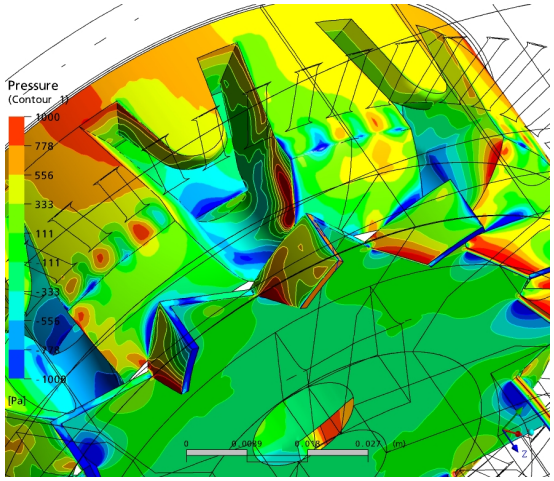

(a) Pressure contours of fan and clawpoles

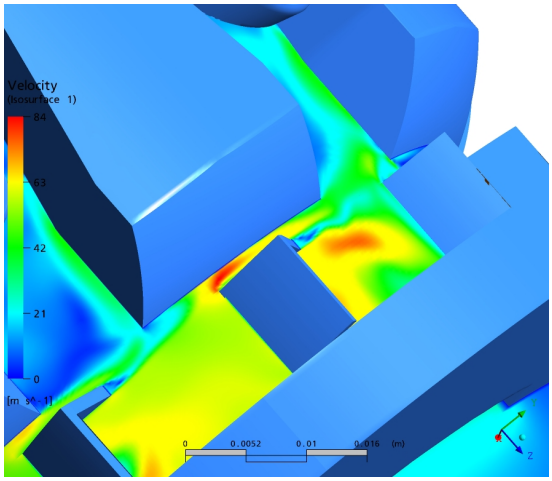

(b) Velocity increase between fan blade and clawpoles

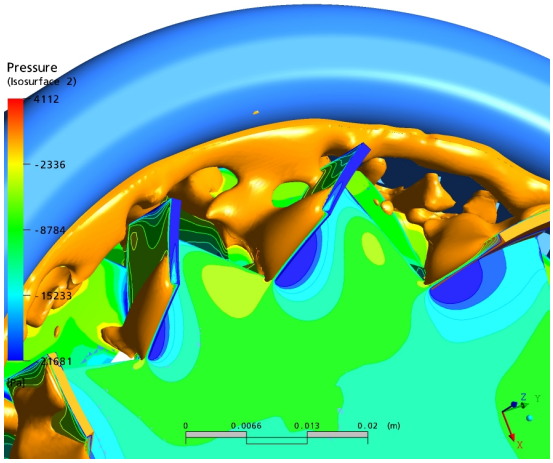

(c) Isosurface of pressure at 400 Pa

Figure 5.5: Pressure distributions on clawpoles and fan blades

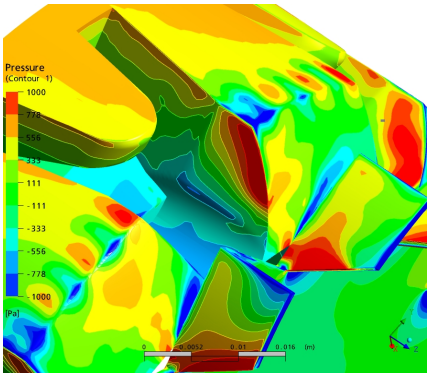

(a) Clawpole pressure, t = 8.7625×10^{-3} s

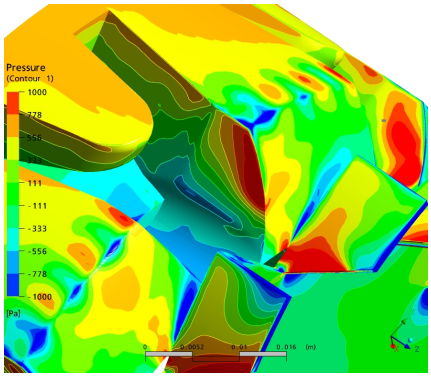

(b) Clawpole pressure, t = 8.775×10^{-3} s

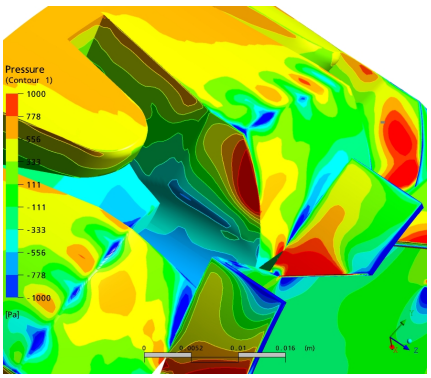

(c) Clawpole pressure, t = 8.7875×10^{-3} s

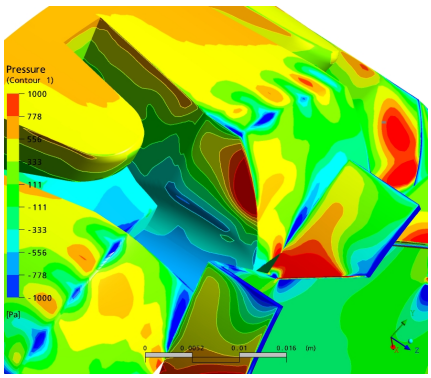

(d) Clawpole pressure, t = 8.88×10^{-3} s

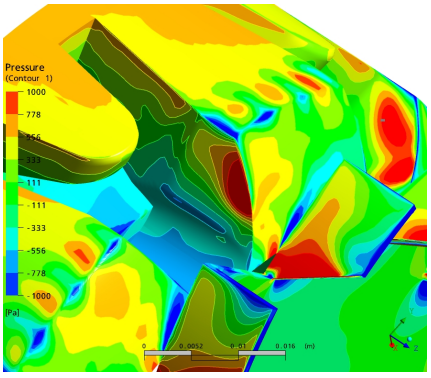

(e) Clawpole pressure, t = 8.8125×10^{-3} s

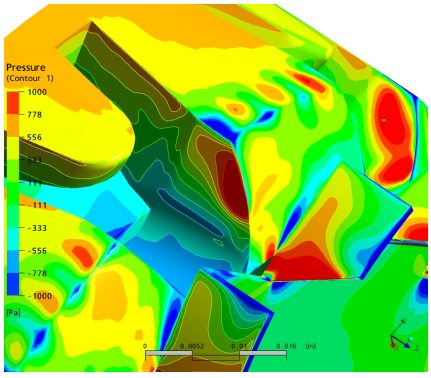

(f) Clawpole pressure, t = 8.825×10^{-3} s

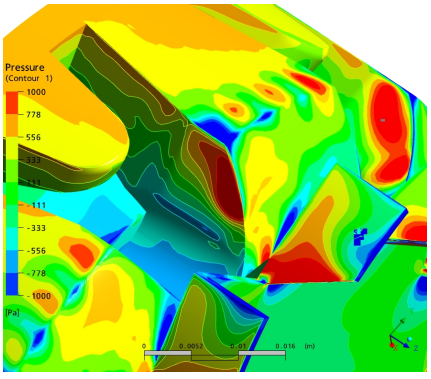

(g) Clawpole pressure, t = 8.8375×10^{-3} s

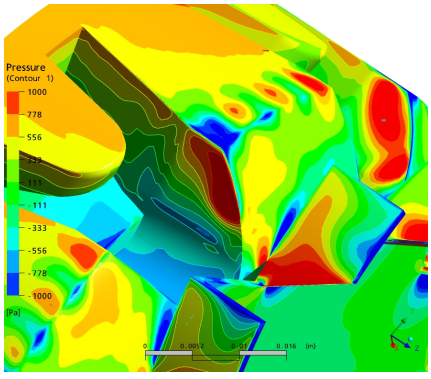

(h) Clawpole pressure, t = 8.85×10^{-3} s

Figure 5.6: Pressure changes on clawpoles over time

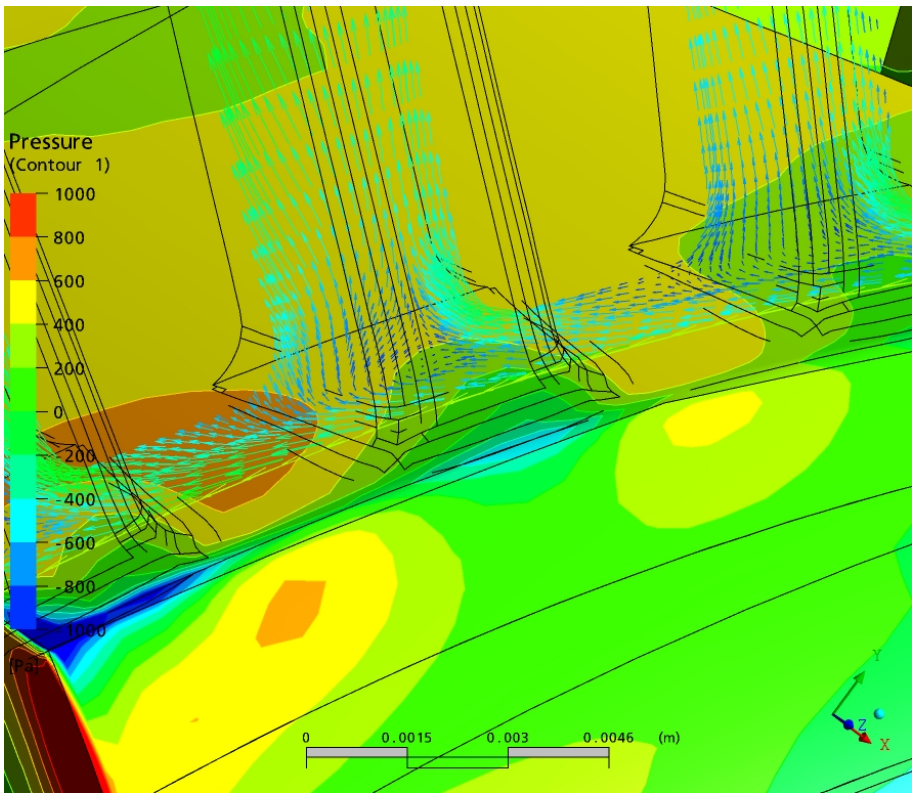

Figure 5.7: Flow stagnation at casing holes

the high and low pressure regions remain, with respect to a stationary observer, stationary. On a surface with discontinuities, any fluctuations occurring on that surface will be modulated over orders pertaining to the number of symmetrical surfaces.

5.2.1 Comparison of stator and rotor pressure fluctuations

Figure 5.8 shows a comparison of the pressure fluctuations occurring on both the rotating and stationary surfaces (the naming conventions are described in Figure 1.2(a)). Pressure fluctuation analysis is carried out by splitting the surfaces into smaller 5mm source surfaces and analysing the average pressure of each source surface over time. It is clear that the largest pressure fluctuations occur on the fan blades, these being significantly greater than those occurring at the downstream front shield. Comparison of the clawpole and adjacent casing shows however that the fluctuations are of a similar magnitude.

As previously discussed, the current form of the Lowson's code only calculates the sound generated by the rotating surfaces. The analysis here shows that, in the case of the fan blades, the fluctuations are much larger than those of the upstream and downstream stationary components. The mechanism of the rotor pressure fluctuations is the downstream generated wake from the ribs. The fluctuating pressure field occurring on the fan blades subsequently impinging the stationary surfaces is of lower magnitude. In the case of the clawpoles and casing, similar fluctuation magnitudes are noted. However, given that rotating pressure field will theoretically generate a higher source strength than a comparable stationary one, as implied by the additional Mach number terms in Equation 2.27, the influence of the rotating pressure field should be higher.

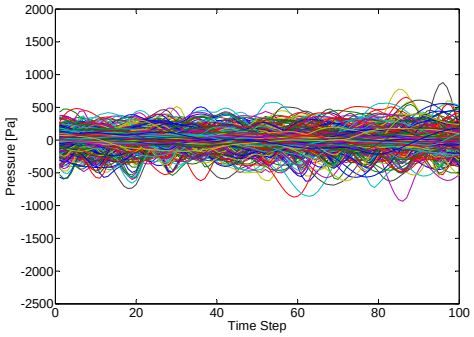

(a) Pressure fluctuations on the casing

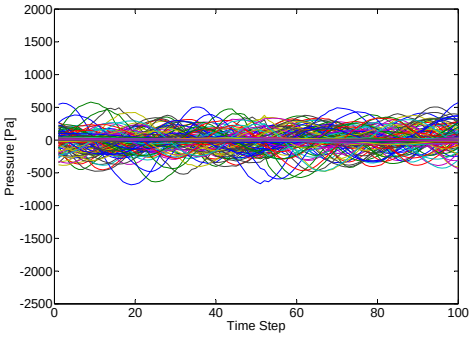

(b) Pressure fluctuations on the front shield with ribs

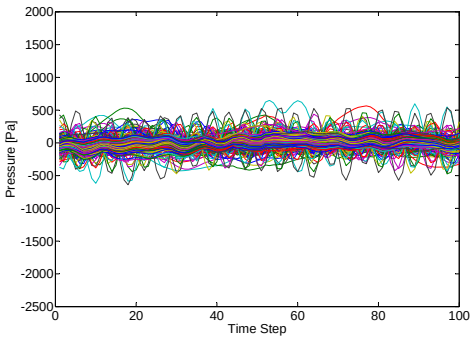

(c) Pressure fluctuations on the clawpole

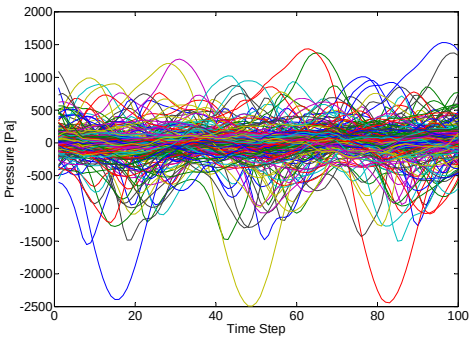

(d) Pressure fluctuations on the fan blades

Figure 5.8: Pressure fluctuations on the stationary and rotating surfaces

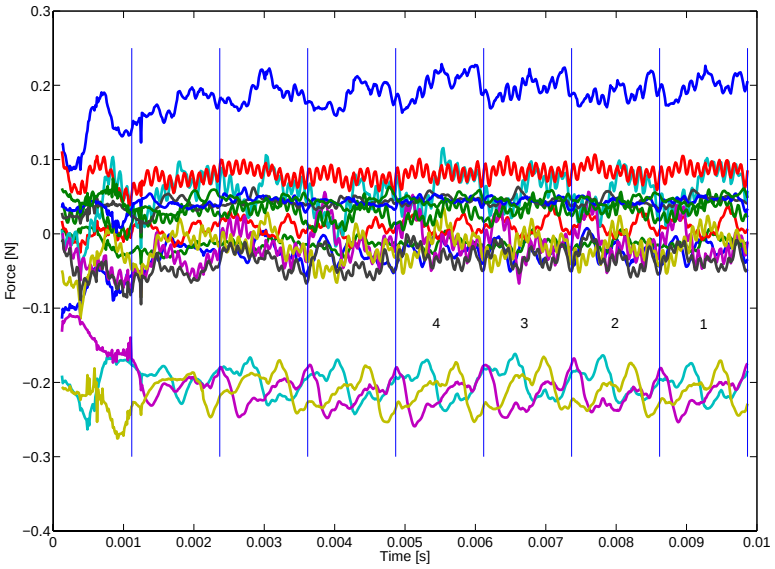

Figure 5.9: Full transient result of reference geometry, two full rotations, with individual surface forces shown for each source

5.3 Aeroacoustic results using Lowson's theory

The well converged computational fluid dynamics calculations from the previous section will now be used in the developed Lowson's Matlab implementations, as per discussion in Chapter 3. Initially, investigations will be carried out on the sensitivity of convergence on acoustic results, whereby several stages of a simulation will be analysed. Additionally, investigations into the influence of microphone resolution on sound power will be carried out, as well as source refinement. Key sources will be highlighted. The influence of a fine, symmetrical mesh will also be shown.

5.3.1 CFD result sensitivity

In the following, results extracted from a transient simulation are compared. The S-Mesh (discussed in greater detail in Section 5.3.5) at 12000 rpm is used for the comparison. A comparison is made between the acoustic results and their variation with respect to the temporal stage of the transient simulation. Referring to Figure 5.9, four acoustic simulations are conducted using in all cases a 16 source model. Two sources are used for each of the fan blades (high and low pressure sides modelled separately), with 10 sources used for the clawpole fingers. 10 microphones are used to reconstruct the sound power, corresponding to the ISO specifications. Results from the CFD simulations are extracted for the last full rotation (segments 1 to 4 in Figure 5.9). Each quarter rotation is then used in the Lowson's code, with the assumption of periodicity for the forces during that quarter. The results are compared in order to indicate whether convergence, from a numerical acoustic perspective, has been reached. Additionally, an analysis is also carried out using the last full rotation, segment 1-4, thus negating the need to assume $\frac{1}{4}$ force symmetry.

Referring to Figure 5.10, a fairly significant variation is noted at several harmonics dependant on the section of CFD results used to define the sources. This indicates that the solution is not entirely converged or simply does not posses the periodicity assumed. In any case, the strongest orders are predicted fairly similarly for all four time segments, these being the 12th order (the blade passing frequency) and the 40th, 48th and 56th orders, which are due to the aerodynamic interactions between the clawpoles and

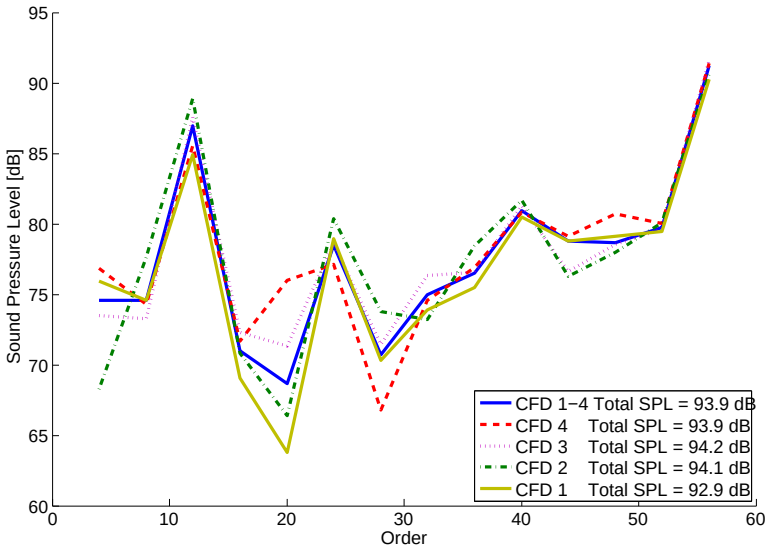

Figure 5.10: Comparison of Lowsons solution for varying 1/4 CFD results

the stator holes. The other orders, that occur predominantly due to asymmetry in the rotor (such as that due to fan/clawpole asymmetry, as previously discussed) show significant variation between the time segments.

5.3.2 Refinement of surface model

Taking the surfaces used in the previous section, a refinement of the source distribution is carried out. A script is used to in CFX-Post to split specified surfaces into a user defined minimum size. A comparison is made using the last quarter of the results shown previously, with several distributions of sources: 1) using the 1 source per surface solution shown previously, thus in total 16 sources (maximum surface size equivalent to the depth of the clawpole finger, 24 mm) 2) using a maximum source size of 10 mm, which produces a total set of 121 sources, 3) using a specified source size of 5 mm, producing a total set of 327 sources and 4) using a maximum source size of 2.5 mm, producing a total set of 1000 sources. Referring to Figure 5.11, which shows the source distribution using 1000 sources, the selected surfaces are split into square elements, the maximum length of a side of each element being regulated by the maximum source size specified.

The forces used in the Lowson's implementation for particular sources are the integrated pressures acting on those source segments. So, for example, when 16 sources are used to reproduce the 16 selected surfaces, only 1 source is used per surface. The pressure on the entire surface is integrated with respect to the area of that surface to determine the input force. For the one thousand source case, the integration is carried out over the surface partitions, thus providing a more accurate representation of localised effects.

The influence of the source sizes is shown in Figure 5.12. It is noted that, up to an including the 24th order, results vary very little with source refinement. For the 12000 rpm case shown, the 24th order corresponds to 4.8 kHz, a wavelength of approximately 7 mm. The 121 source model begins to deviate from the solution at the 40th order (8 kHz, 4.25 mm wavelength) while the 327 source model accurately represents the acoustic solution up to and including the 56th order (11.2 kHz, 3 mm wavelength). In any case, we note that for the frequencies of interest, a maximum source size of 5mm is sufficient to take into account localised source interactions.

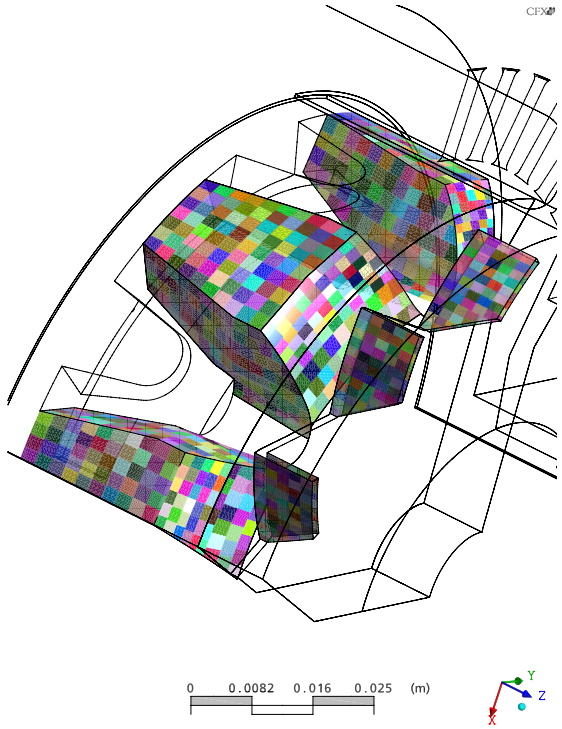

Figure 5.11: Source distribution for the 1000 source case

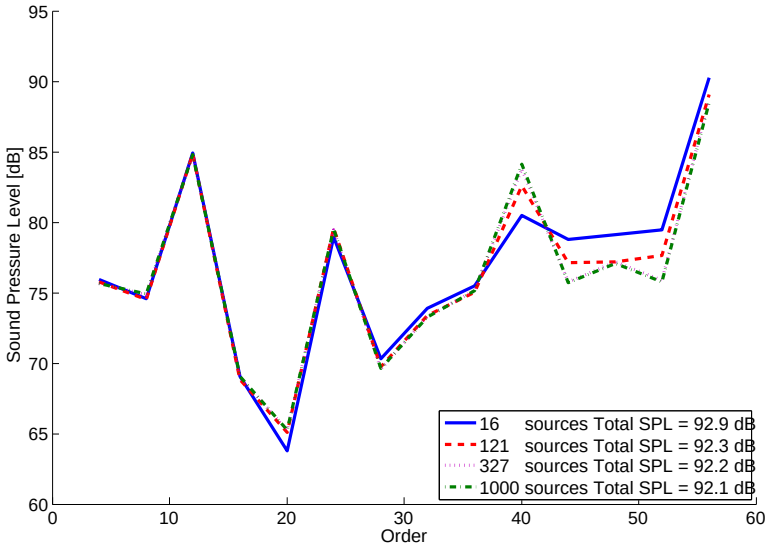

Figure 5.12: Effect of source refinement on acoustic results

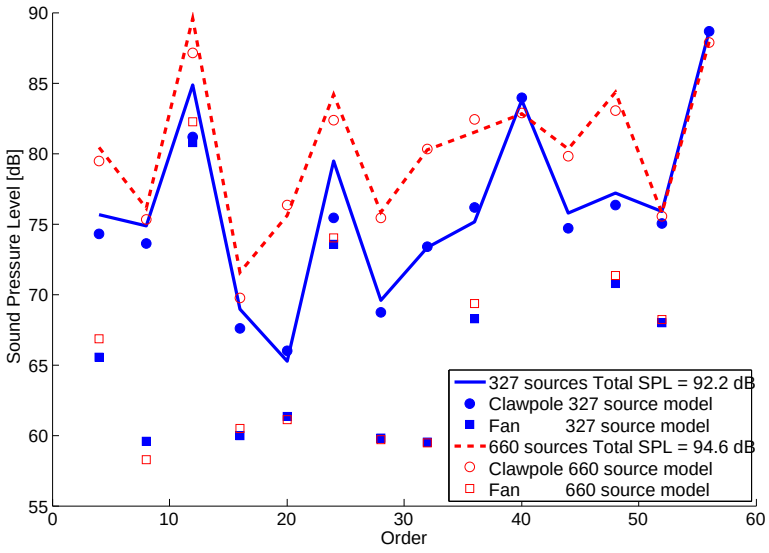

Figure 5.13: Effect of source increase, rear clawpoles included

5.3.3 Inclusion of all rotating surfaces

In this simulation, further surfaces are included in the calculation using sources of 5 mm. Essentially, all rotating surfaces are hereby taken into account, including the rear 'half fingers' of the clawpole and the radial plate of the fan blade. This is in order to give an indication whether the sources considered as the main sources of sound (fan blade top and bottom surfaces, front clawpole surfaces) are in fact enough for an accurate acoustic calculation. This is compared to the 327 source model used previously. Although the source count is largely increased with the inclusion of additional sources from rear clawpoles, it is important to note that the source density remains unchanged, thus the comparison here is to determine the influence of the entire clawpole structure on sound propagation.

Figure 5.13 shows the results from the use of all rotating surfaces for the calculation (327 sources compared to 660). The variation to the acoustic result is due primarily to the additional clawpole surfaces modelled, clearly seen by the separation of clawpole and fan effects on the sound power level. The addition of the radial plate adds very little sound energy. The clawpoles on the other hand clearly influence essentially all the orders, and not only the ± 8 orders, due to the asymmetry caused by the relative positioning of the fan blades and clawpoles.

5.3.4 Microphone resolution analysis

In this analysis, a comparison is made to determine the influence that the number of microphones has on the far field sound field. An accurate solution of the sound power spectra is considered one that does not change with the use of more microphone points. The comparison will be conducted using two different microphone setups: 1) Setup corresponding to a planar analysis, in both lateral and longitudinal directions, which will allow comparison to the 9 microphone test bench from Section 4.7 in order to determine how well resolved the configuration is and 2) a setup corresponding to a sphere at a radius of 1 meter, corresponding to the experimental study conducted at the ISO test facility. For the study, both cases use the 660 full rotor source model as the basis; the source sizes were shown to predict the sound energy well, and should capture any influence microphone number has on the average far field sound propagation.

Figures 5.14 to 5.16 illustrate the variations in the results when the number of microphones is changed

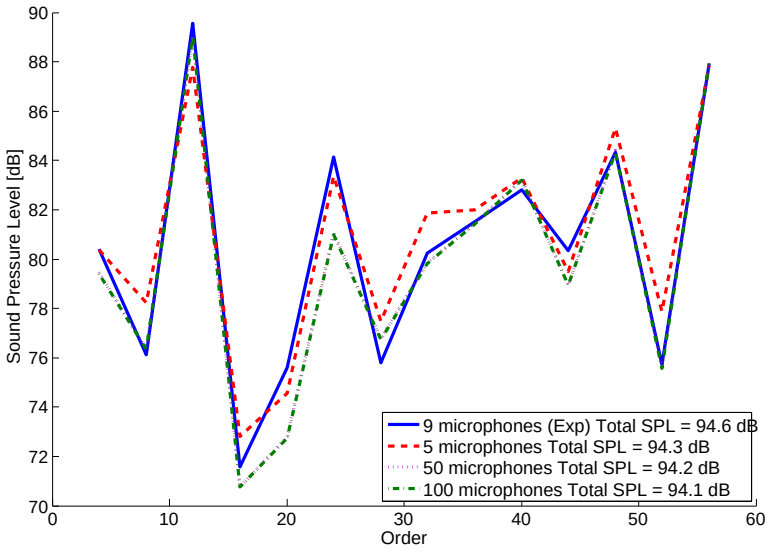

Figure 5.14: Influence of microphone count on total SPL spectra in the plane of rotation $r = 0.6m$

in both the planar cases, in addition to the spherical measurement. It is clear that in all instances, a microphone count of roughly 50-60 provides a resolution accurate enough for the higher frequencies. It is clear that for lower frequencies, a smaller number of microphones suffices given that the measurement resolution is smaller than the corresponding wavelength. Higher resolutions are affected somewhat more. The spherical microphone configuration, Figure 5.16, shows significant variations with the solution due to an increase in microphones. Here, similarly to the other cases, the energy converges with a microphone count above 50.

5.3.5 Mesh variation analysis

The reference geometry is compared to see how variations in the mesh quality and blocking strategy influence the results. In this instance, a reduced number of sources are used in order to determine in a general sense, the reasoning for any differences. In both cases, each surface is modelled as one source. The sources used for the comparison are the top and bottom surfaces of all three fan blades. The top of both main clawpoles, in addition to the leading edge of both clawpoles, are not used in the calculation; essentially the comparison seeks to find the difference in sound generation from the fan blades between the two meshes. The microphone positioning is parallel to the plane of rotation, using 50 microphones at a distance of 1 meter from the centre of the alternator. This measurement plane is chosen to ensure the highest direct influence from the fan blades.

Figure 5.17 compares the force fluctuations on the suction side of the blades, with the force histories time-shifted for easy comparison. All three blades are shown, for both the M-mesh and the S-mesh. It is clear from the figure that, in general, the forcing fluctuations acting on the blades show a similar form for both meshes. The force fluctuation is evident as the blade passes by the upstream rib. More importantly, however, is the differences occurring from blade to blade. There is a notable difference in the amplitudes on the M-mesh, whereas the S-mesh shows only a slight variation.

The difference between the two meshes is one of symmetry and mesh size (the asymmetrical M-mesh has 3.3 million elements in the rotor, the symmetrical S-mesh has 1.3 million), seen in Figure 5.18. The S-mesh was constructed such that only one blade was blocked and meshed, with the mesh rotated and copied two times, giving a total of three blades in the quarter model. Much the same procedure was carried out with other parts of the geometry; one clawpole finger was meshed, with one copy made to

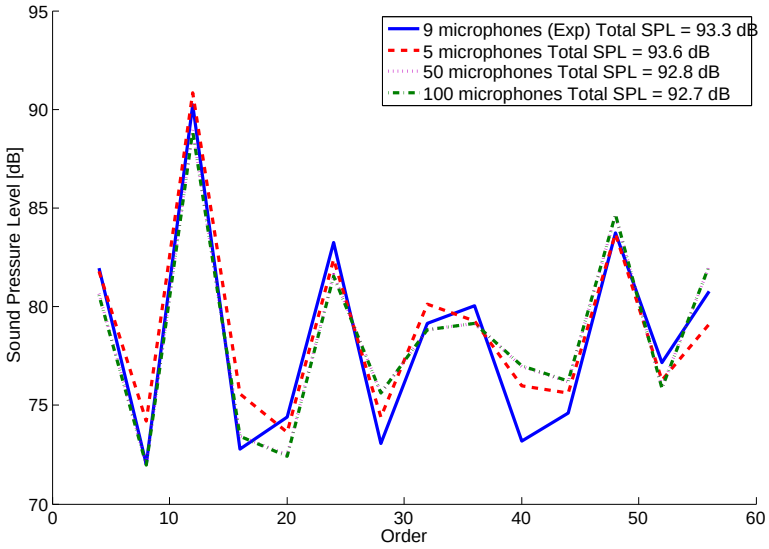

Figure 5.15: Influence of microphone count on total SPL spectra in the plane perpendicular to rotation $r = 0.6m$

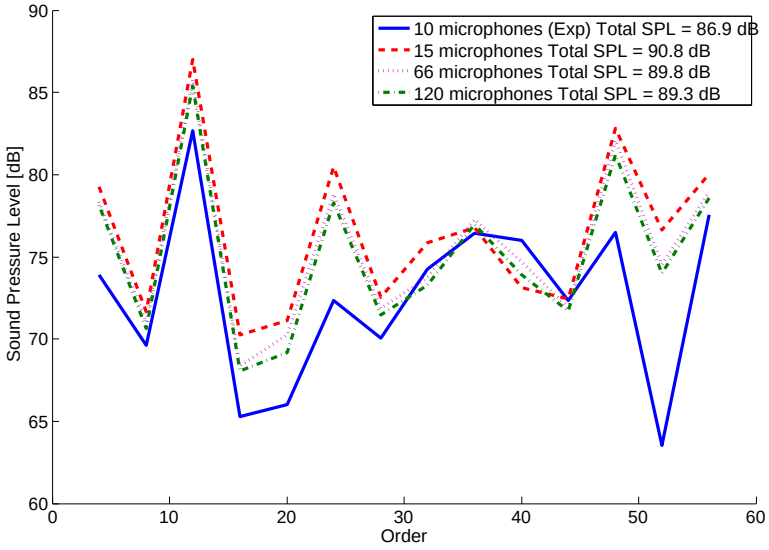

Figure 5.16: Influence of microphone count on total SPL spectra in a spherical plane $r = 1m$

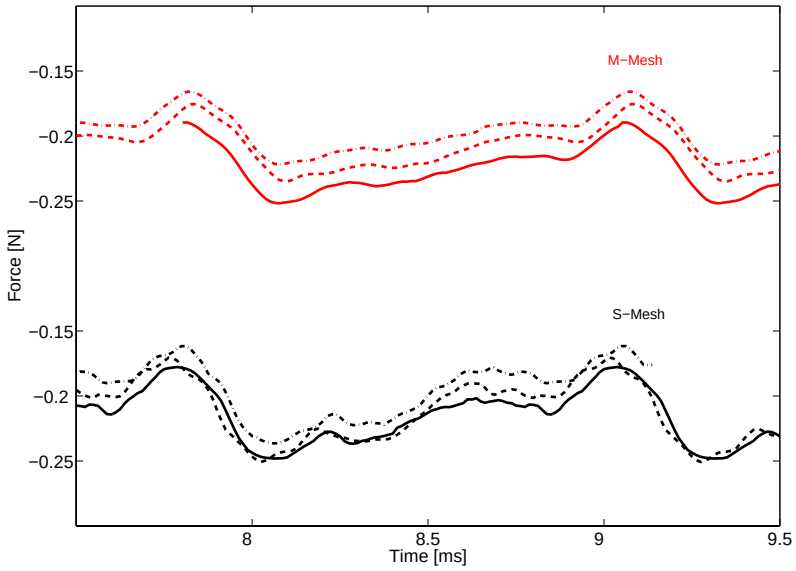

Figure 5.17: Comparison of blade forces for different meshes

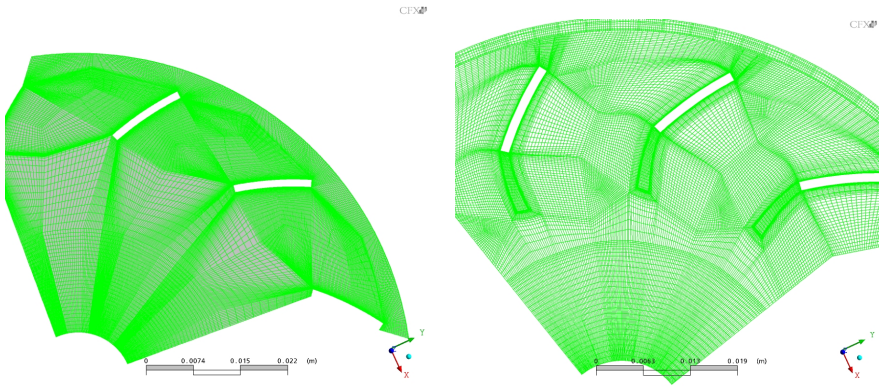

(a) M-mesh (b) S-Mesh

Figure 5.18: Comparison of mesh quality and influence on the individual fan forces

create two clawpole fingers. Furthermore, the casing holes were also constructed once, and copied eleven times. This ensures a perfect symmetry between the consecutive blades and geometries, ensuring that no numerical asymmetry is present. The M-mesh, on the other hand, was constructed such that each of the three blades was meshed independently of one another. In doing so, mesh symmetry is not guaranteed. Furthermore, whereas the periodic boundary conditions are placed evenly in the fluid in the S-mesh, in the M-mesh, given the orientation of the blades, the periodic boundary condition was placed along the suction side of one of the blades.

Table 5.1 indicates the influence of the varying forces on the blades on the acoustic propagation, calculated using Lowson's equation. The variation in the first 3 harmonics is significant. In this numerical trial, only the fan blades (6 sources extracted from the 6 fan blade surfaces; three fan blade surfaces, suction side and high-pressure side) were used as source terms.

The reasoning behind the variation, given that the forcing fluctuations are not significantly different, can be related to the theory of Section 2.4. This theory indicates that, if a set of surfaces are equally spaced in the radial direction, and that their pressure distributions are identical, albeit phase shifted by Δt (defined in Equation 5.1, where ω is the rotational speed and n the number of symmetrical surfaces), then only the order equivalent to n will be influenced i.e. 12 equally spaced blades with equal force histories

	4th Order	8th Order	12th Order
M-mesh	72.1	68.3	72.6
S-mesh	66.1	65.3	81.7

Table 5.1: Sound Pressure Level at the first 4 harmonics

	Blade 1	Blade 2	Blade 3	All active
M-mesh	79.6	74.7	80.5	72.6
S-mesh	81.3	82.0	82.1	81.7

Table 5.2: Comparison of the 12th harmonic with loading considered identical on all blades

will only produce a 12th order noise, and harmonics thereof. If, on the other hand, the surfaces are not equally spaced in a radial direction or do not have similar force histories, they will act independently of each other, in essence transferring energy to other orders. This can be clearly seen in the M-mesh results; due to the variation of the forces acting on the blades, no dominant 12th order is produced.

$$\Delta t = \frac{2\pi}{\omega n} \tag{5.1}$$

Table 5.2 shows this effect clearly. The all active column are the acoustic results at the 12th order from the previous discussion. In this numerical trial, each of the three blades is modelled individually with the assumption that all other 12 blades experience an identical, albeit time shifted, force. This assumption results in only every 12th order of sound being produced. For the M-mesh, the results clearly indicate that, if all fan blades have an identical force history, regardless of which force history from the three blades, the sound generated is significantly greater at the 12th order than that produced when the force histories on the blades are different. A similar conclusion can be made with the S-mesh, although the tendency is much weaker given that all three blades already have similar force histories. It is noted that, if Blade 1 is made active across all 12 blades, its 12th order sound output is lower than when all three force histories are active. The reasoning for this is that Blade 2 and Blade 3 are stronger sources of the 12th order sound.

The small variation of the forces acting on the S-mesh is due to the differences of the fan blade positioning with respect to the clawpoles. The flow is unique around each fan blade given that its positioning with respect to the clawpole surfaces is different, discussed in detail in the previous section.

5.4 Experimental and numerical comparison

The following will compare the results obtained using the implementation of Lowson's theory to the measurements carried out. Comparisons will be conducted using high resolution source models as those determined sufficient in the preceding discussion. Two main geometries will be compared; the fan blade geometry with the eight finger clawpole and the isolated clawpole model.

5.4.1 Reference geometry

Figure 5.19 shows a comparison between the results from the experiments conducted at the ISO test facility and the numerical simulation carried out. For the simulation, the prediction is also separated into the sound produced by the sources placed on the fans, and those placed on the clawpoles. For this comparison, the detailed 660 source model is used, with ten virtual microphones used for calculation, corresponding to the microphone distribution from the ISO 3745 specification. This acoustic model applies sources to the entire rotor.

As can be seen, a majority of the orders are predicted within an accuracy of 5 dB(A), in addition to the total sound power level calculated from the energetic summation of the individual orders. This does not correspond to the total measured sound power level. The measured total sound power level is 99.2 dB(A); this is the total sound energy emitted. The energy summation of the orders, calculated using Equation 5.2, is 93.0 dB(A) in the experiment, where L_{W_O} is the contribution at the orders $i = 1$ to n. For the simulation, the energetic summation of the calculated orders is 94.5 dB(A), a 1.5 dB(A) difference. The difference of over 6 dB(A) between the measured total sound power level and the energetic summation of the relevant orders is due to certain minor orders not being included (not measured) in addition to large bands of broadband noise being ignored in the order calculations. These broadband contributions are due to non-periodic flow phenomena, such as ingestion of turbulent flow, which given the assumption of periodicity in the numerical calculation, cannot be determined.

$$L_W = 10 \log \sum_{i=1}^{n} 10^{0.1 L_{W_O}} \tag{5.2}$$

The main discrepancy is seen at the 24th, 32nd, 36th and 56th orders. The 56th order is consistent with a side band of the higher order clawpole orders, due to the 48th order fluctuation at the casing holes and the subsequent 8th order shift due to the Doppler effect on the symmetrical, eight rotating surfaces.

The contribution to the total results of the fan and clawpole surfaces is here evident. All orders except the 12th are strongly dominated by the clawpole surfaces. The theory and experimental results indicated that any fan blade dominance should occur at every 12th order. The fact that the clawpole also generates a strong twelfth order is due primarily to the fact that the fan blade forces act on the clawpole root sections, and thus impinge a pressure distribution on the clawpoles congruent of the symmetrical fan blades; the influence the fan blades have on the clawpole surface pressures has been discussed in Section 5.2.

Considering for the moment only the fan blade contributions at orders 24, 32 and 36, the discrepancy would be, respectively, 4.4 dB(A), 6.4 dB(A) and 1.9 dB(A). This is a significant improvement over the discrepancies shown in Figure 5.19. Evidently, the error in this region is due to the forces on the clawpole surfaces being poorly predicted.

The extracted forces from the CFD computation are shown in Figure 5.20. The forces here are extracted from the last $\frac{1}{4}$ rotation from the transient CFD, and repeated 4 times to show the total input into Lowson's equation. The rectangle in Figure 5.20 indicates where the first copied set begins. Generally, the assumption of periodicity appears valid, as no sudden step in the results is observed. Only the Fan Top A surface appears to have a small jump in the force. The Clawpole Top A surface, the top surface of the middle clawpole finger, appears to undergo a noticeable low order oscillation.

Figure 5.21 shows the numerical and experimental comparison of the individual microphone total pressure data, where microphone 1 to 10 are numbered as per definition in the ISO specification [3]. Here, it is clearly evident that the relationship between the 10 microphones compares well. In both cases, microphones 2 and 8, both positioned behind the alternator, show minimal sound propagation. The numerical calculations indicate also a minima at microphone 10, this being radially above the alternator. The maxima for both instances occurs at microphone 5, this being located in front of the alternator. Here, sound propagation from both the fan and the clawpole sources is high, given the direction of the surface normals (in particular the clawpole roots). Overall however, the sound pressure is lower numerically than it is experimentally, due to the inability to model non-periodic mechanisms that have an influence on total sound levels.

	Difference [dB(A)]
Total Sound Power Level (energetic sum of orders)	+1.5
Orders	
4th	+4.2
8th	+2.3
12th	-0.2
16th	+1.5
20th	-0.8
24th	+8.2
32nd	+15.7
36th	+13.7
40th	+0.6
48th	0.0
56th	+10.9

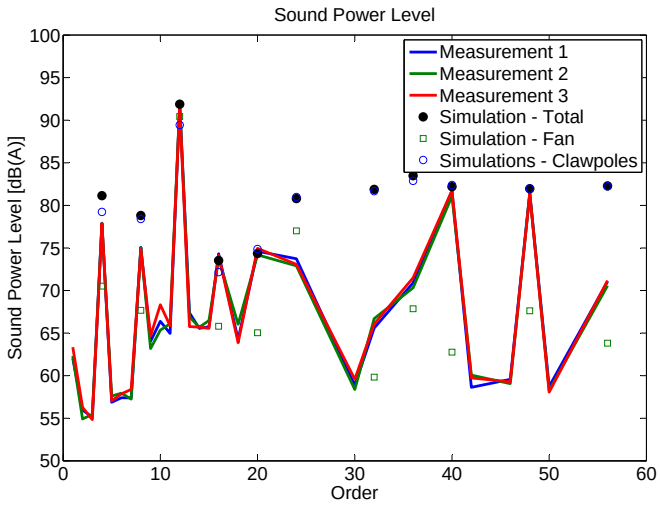

Figure 5.19: Comparison of numeric and experimental results, reference geometry

5.4.2 Geometry without fans

Figure 5.22 shows the comparison between the measurements carried out on the ISO test bench and the numerical calculation of the geometry without fans. The source size used for this calculation is the same, however given the lack of fan blades in the calculation, the total source count is lower at 305 sources. The same ten microphone positions are used as before. The total sound power level measured is 89.6 dB(A); the energetic contribution of the relevant orders is 79.7 dB(A). The corresponding energetic summation of orders from the numerical calculation is 79.1 dB(A), a difference of 0.6 dB(A). Regarding the individual orders, most are predicted to within an accuracy of 6 dB(A), except the 8th order. This high energy is due to a prevalent eighth order fluctuation that occurs on the clawpole surfaces.

Figure 5.23 shows the extracted forces from 3 of the surfaces used in the no fan calculation. In this instance, given that the geometry has a $\frac{1}{8}$ symmetry, the forces are repeated 8 times. The rectangle in the force history shows once again where the first $\frac{1}{8}$th cycle ends. The surfaces analysed are analogue to those in Figure 5.20. Once again, particularly at the clawpole top surface, a significant low order fluctuation occurs that appears to be nonphysical. In this geometry, given that the stator is modelled with the 48 holes and the rib obstructions are not modelled, a low order fluctuation is not expected. This fluctuation appears to be related to the geometrical symmetry; the $\frac{1}{4}$ model appeared to have a dominant 4th order fluctuation, the $\frac{1}{8}$th model a dominant 8th order fluctuation. Rather than a physical phenomena, this appears to be due to an error caused by both the rotor/stator interface together with the periodic boundary condition, given that the root and side clawpole surfaces undergo a much lower amplitude low order fluctuation.

The comparison of the individual microphone sound pressure levels is once again carried out, and as before, the tendencies of the pressure distribution are similar for both the experimental and numerical results, as shown in Figure 5.24. The microphone with the lowest sound pressure level signal is correctly predicted to be microphone 2 (located behind the alternator), while microphones 4 to 8 have roughly

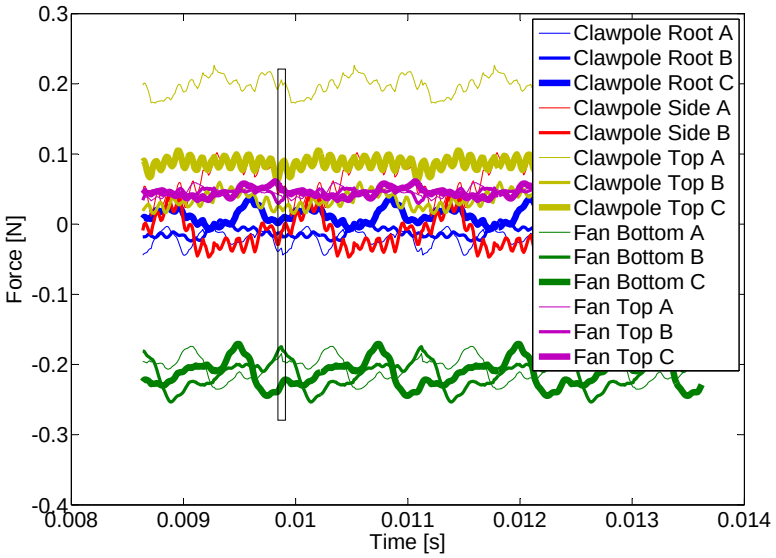

(a) Force time history; $\frac{1}{4}$ rotation repeated 4 times

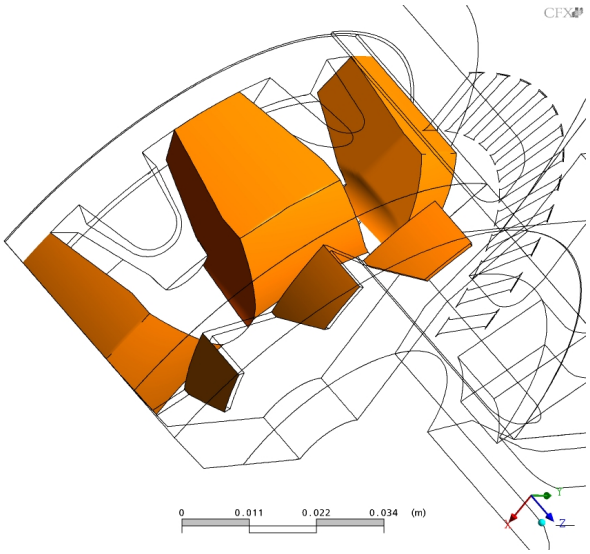

(b) Sources/surfaces used for 14 source extraction

Figure 5.20: Extracted forces from the 14 source resolution

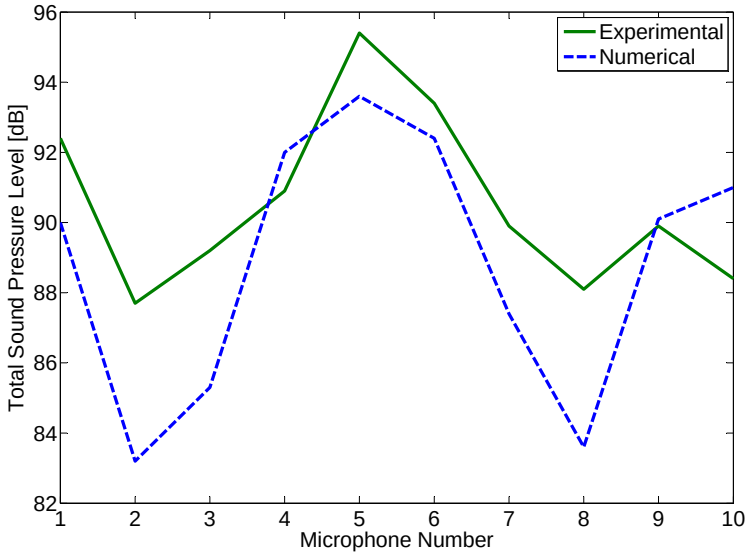

Figure 5.21: Comparison of individual microphone sound pressure levels

	Difference [dB(A)]
Total Sound Power Level (energetic sum of orders)	-0.6
Orders	
8th	+16.3
16th	-6.1
24th	-4.4
32nd	-5.3
40th	-5.2
48th	+1.1
56th	-1.9

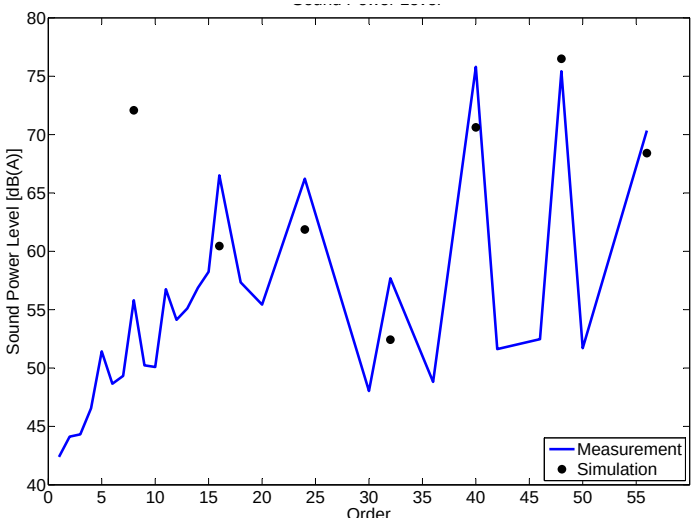

Figure 5.22: Comparison of numeric and experimental results, geometry without fan

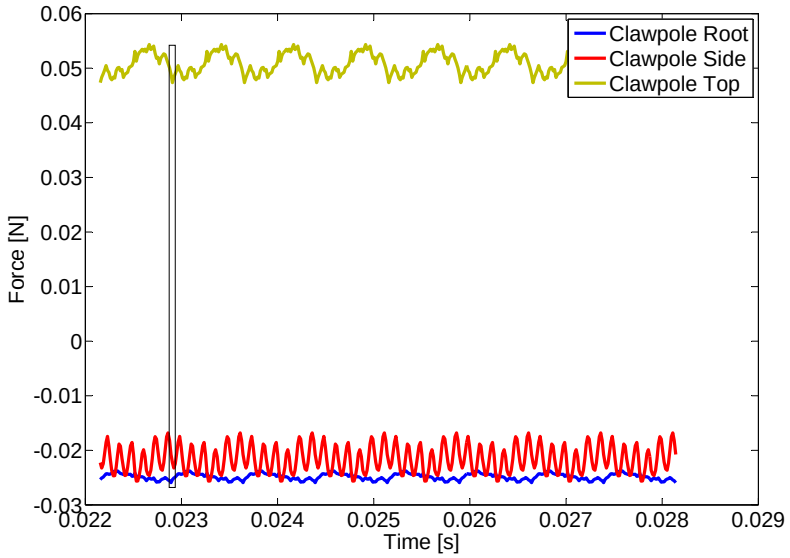

(a) Force time history; $\frac{1}{8}$ rotation repeated 8 times

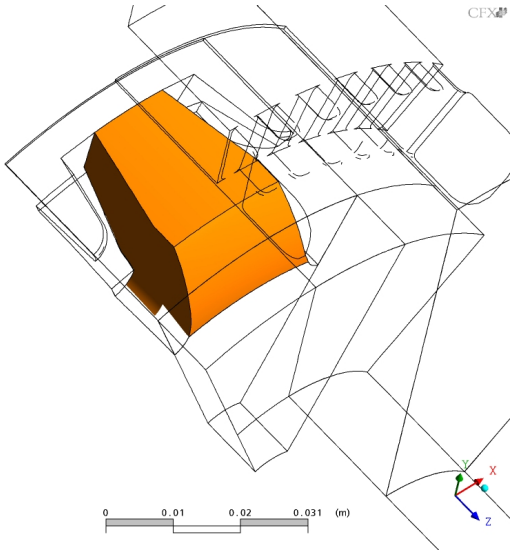

(b) Main clawpole sources

Figure 5.23: Extracted forces from the main sources of the no fan geometry

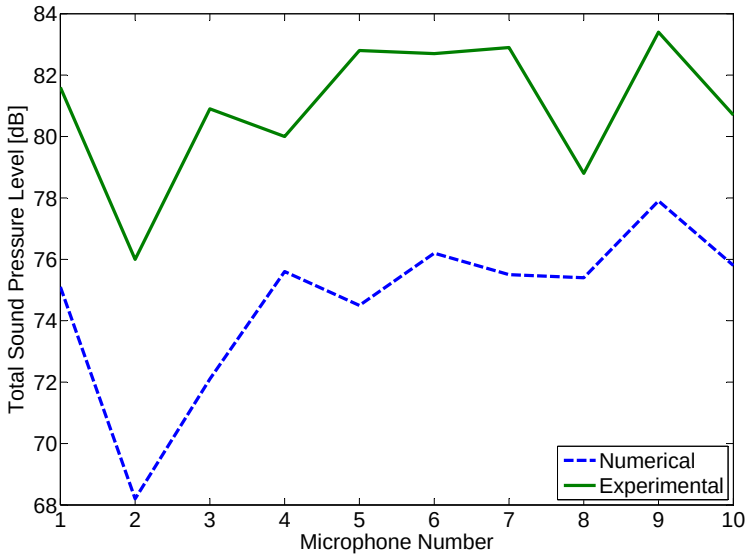

Figure 5.24: Comparison of individual sound pressure levels

similar sound pressure levels. The numerical simulation does however correctly predict the dominance of microphone 9, located radially and slightly in front of the alternator.

5.5 Asymmetrical influences of the reflective plate on sound propagation

An analysis of the asymmetry of sound propagation caused by the reflective mirror plate is carried out. For the purpose of this, measurements from the 9 microphone configuration have been used, in both lateral and longitudinal cases (see Figure 4.2). The reference geometry is used, with the 660 full rotor source model already outlined. Figure 5.25 shows the comparison of total sound pressure level (broadband and harmonics included) between the measured data and calculated data. Once again, as previously discussed, sound pressure is generally lower for the computed cases due to the inability to model broadband noise sources. In the instance of the lateral case, significant asymmetry is noted across the 9 microphones. A large pressure change occurs at microphones 6 to 8. Observing the configuration in Figure 4.2(a), these latter microphones are in a region where the reflective plane ends. In contrast, the numerical calculation assumes an infinite plate. For the longitudinal case, a similar asymmetry is noted. Here however, comparing measured data with the numerically calculated data, the relative strengths between consecutive microphones is similar. Microphone 1, axially positioned ahead of the alternator, experiences the highest noise. This then gradually reduces for the microphones radial and behind the alternator, slightly increasing with microphone 9, axially located at the rear of the alternator. This tendency can be seen both experimentally and numerically

Numerical calculations are repeated on a much finer microphone grid, to capture the interferences causing the asymmetry. A grid of 10,200 microphones is used for this purpose. Given the size of the grid, only the 16 source model is used. The total sound pressure (calculated by summing the energetic contributions from individual orders) is shown in Figure 5.26 for both lateral and longitudinal cases. As can clearly be seen, asymmetrical effects are noted for both the lateral and longitudinal cases. For the lateral case, this is due predominantly to the effects from the reflective plate and the influence it has on sources approaching and moving away from it. This reflective plate is located at a position $y = 0$. The

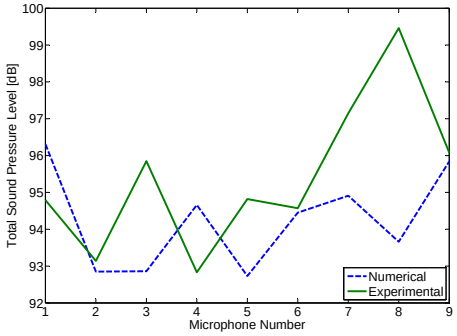

(a) Comparison of numerical and experimental results for 9 microphone lateral configuration

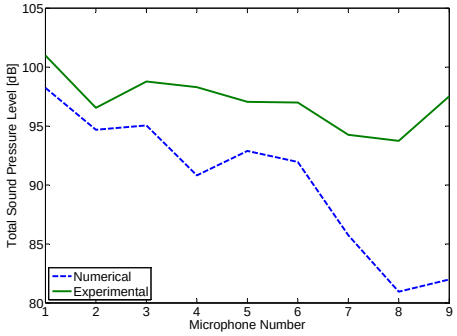

(b) Comparison of numerical and experimental results for 9 microphone longitudinal configuration

Figure 5.25: Asymmetrical sound propagation; 9 microphone configuration results

mirror sources are located below this, and it can be seen that about $y = 0$ there exists symmetry, hence confirming the effect of the mirrored sources. The pressure distribution at $y = 0$ agrees well with the well know solid wall boundary condition in acoustics, which stipulates a zero pressure gradient across walls. For the longitudinal case, the asymmetry is also due to the directionality of the sources; they predominantly act radially and in the positive z- direction.

In order to show the influence of the reflective plane, computations are repeated without taking into account the reflective plane and assuming complete free-field radiation. Results are shown in Figures 5.26(c) to 5.26(d), whereby the alternator is in this case centred at $y = 0$. Quite clearly, the pressure distribution in the lateral plane is significantly more symmetric, with slight asymmetries in the far field due to localised effects from disturbances (analog to the analysis shown in Figure 3.2). In the case of the longitudinal plane, asymmetry is still present due to the majority of sources acting radially and in the positive z-direction.

5.6 Full model simulation in product development

The final comparison shown is one relating to a complex geometry representative of a full alternator model. The geometry comprises of 26.3 million elements, and is a 360 degree full-model; it therefore contains no periodic boundary conditions. The fan blades in this case are asymmetrical and, due to this, generate energy at side bands of the blade count (12 blades on the pulley side, 10 blades on the rectifier side). The components of this model are shown in Figure 1.1(a).

Given the size of the model, the chosen time step size was relatively large; 120 time steps per full rotation. At a speed of 10,000 rpm, this is $5 \times 10^{-0.5}$ seconds. Computation time for 2.3 full rotations using 16 CPU cores (AMD Quadcore 2.8 GHz) was 276 hours, with each time step requiring 1 hour of calculation time. After 2.3 rotations, results from the last full rotation were extracted, in total from 2,727 sources covering the entire rotor. Microphone positions used for the calculation are equivalent to the ISO microphone distribution used for the measurements.

The results are shown in Figure 5.27. The measurements taken are from 10 alternators. The numerical simulation is carried out using two different time regions; the first at time steps from 75-194 (black dotted line), the second from time steps 156-275 (red dotted line). This is in order to demonstrate the level of temporal convergence. The differences shown in the ten alternators is due to tolerances in the production.

It is clear to see that the relationship between the orders 6-15 are represented well in the numerical calculation. The calculated power levels at the strongest orders are within the variation of the ten

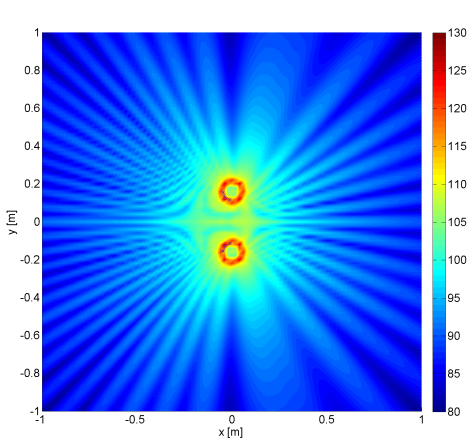

(a) Lateral plane, with reflective plane

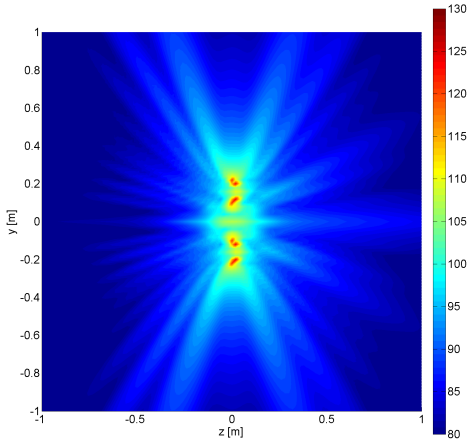

(b) Longitudinal plane, with reflective plane

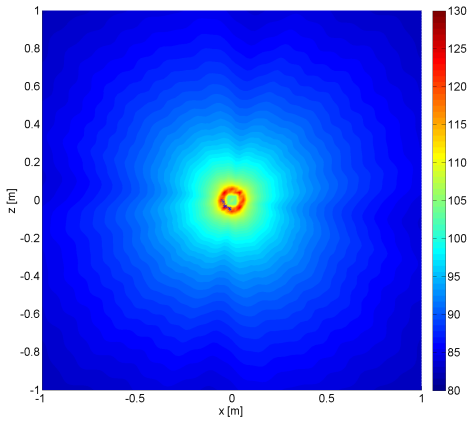

(c) Lateral plane, without reflective plane

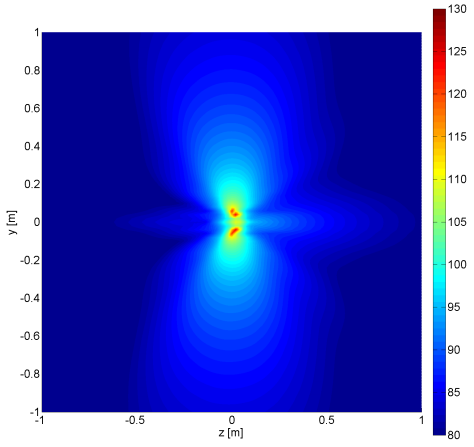

(d) Longitudinal plane, without reflective plane

Figure 5.26: Detailed plane analysis of asymmetrical sound propagation effects

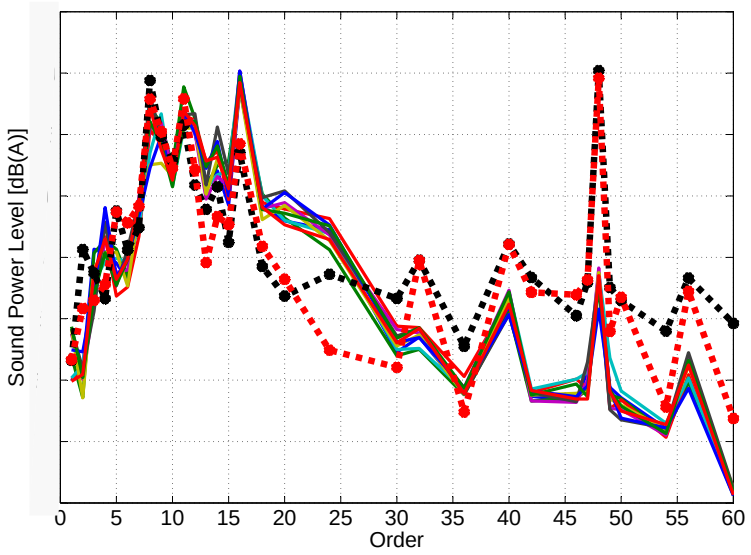

Figure 5.27: Comparison of numerical (dashed line) and experimental (solid line) results of a real alternator product

measured alternators. As of the 16th order, the differences are noted to be much higher. In particular, the 16th order is under predicted, while the higher clawpole orders are significantly over predicted. The reason for this is the copper winding geometry of the actual alternators; in the numerical calculation, this is modelled as 48 equally spaced and sized holes in a cylindrical casing. In the actual geometries, these holes are constructed in an irregular fashion from copper windings (see Figure 1.1). The irregularity of the holes removes energy from the higher clawpole orders, existent in the numerical model due to the regularity of the holes, and shifts the energy to lower clawpole orders, in this case the 16th.

The total energy calculated is very close to that measured. The total sound power level measured ranged from 91.2-91.5 dB(A). The total sound power level calculated using only the orders which are explicitly calculated during measurements ranged from 84.6-86 dB(A). The energetic summation of these orders from the numerical calculation produces a total sound power level of 85.8 dB(A); within the tolerance of the measured alternators.

5.7 Summary

Throughout this section, the CFD calculations that were used to obtain the transient surface pressure data were discussed, including important parameters for the model construction. The importance of using a symmetrical mesh for symmetrical parts was shown. Asymmetry in the mesh was found to cause slight asymmetry in the force data, which falsified the calculated orders.

Studies were also carried out using the numerical acoustic software to determine the effect of several variables on calculated results. It was found that the number of microphones used in the experiments was not necessarily enough, given that numerical convergence occurs only with a higher count of microphones. For a spherical microphone plane, up to 66 microphones were required in order to obtain convergence for the frequencies of interest. Source size calculations were also carried out in order to show the optimal source size for acoustical convergence.

Once these studies were carried out, direct comparison was made with experimental studies carried out at both the ISO test bench and the 9 microphone test bench. Although the total sound power level

was not calculated accurately, with a deviance from experimental results of up to 11 dB(A) noted, this was due to the underlying assumption of periodicity in the alternator. Non-cyclic fluctuations due to broadband turbulence were not simulated given the resource restrictions, whereby both resource intensive turbulence models would need to be used in addition to calculations carried out over more rotations in order to calculate for non-cyclical (lower than first order) fluctuations.

The comparison of total sound power level was thus carried out by calculating the energetic summation of orders common to both the experiment and numerical calculation (every fourth order for the quarter model, every eighth order for the eighth model). Here, the results were very good, with differences to the ISO test bench being no more than 1.5 dB(A). Order calculations differed on average between 5.3 to 5.7 dB(A) compared to the ISO test bench. Finally, comparison of the distribution of sound pressure level across the ISO configured microphones was very good , with the loudest and quietest microphones being correctly predicted. The 9 microphone configuration showed slightly worse results due to the smaller size of the reflective plane on the test bench; here, the numerical assumption of an infinite reflective plane is not an accurate one. In any case, comparison of the data yielded the presence of asymmetries; laterally, these were due predominantly to the reflective plane, while longitudinally, these were due predominantly to the asymmetry of the alternator and it's sources in the z-direction.

The ability of the code to function well with highly complex geometries representative of real products has also been shown, with an accurate representation of the frequency distribution caused due to asymmetrical blade spacing. Although some of the clawpole orders were not well predicted, this was due to simplifications made in the CFD model which caused a strong 48th order symmetry that does not occur in the real product.

Chapter 6

Casing effects on sound propagation

The Lowson's implementation used in Section 5 ignores effects of the casing, assuming rather that the spinning modes produced by the rotor propagate outwards in a free-field towards the observer. Additionally, stationary sources due to pressure fluctuations acting on the casing are also ignored. In order to determine the influence that a casing may have for a simplified alternator geometry, further analysis is carried out on casing effects using two numerical tools.

1. Boundary Element Method. The aim is to use Lowson's equations to calculate the rotating sound pressure field in the near field (located between the rotor and stator) and use a BEM solver (LMS Sysnoise) to propagate the solution outwards past the casing. In this case, sound waves reflecting from the casing cannot return into the rotor as there is no two way coupling between the Lowson's solution and the BEM solver. The Lowson's solution is required to provide the spinning modes from the rotor. These cannot be obtained from the BEM solution alone due to it's inability to model two frames of reference (rotating and stationary).

2. Finite Element Method. Given the added resource intensive calculations in the FEM solver utilised, the problem will be kept modelled in 2D. Using the COMSOL Multiphysics solver, only the acoustic creation and propagation will be considered, although it is technically feasible to couple a CFD solution with the solver, albeit only for a two-dimensional problem. Here, variations to Lowson's solution, in addition to comparisons of the propagation between solutions without casing and those with, will be shown. The benefit of this particular FEM solver is the ability to model several frames of reference.

6.1 Boundary element methods

The following section will provide a brief overview of the general theory of Boundary Element Methods, essentially focussing on the use of the Green's functions in the derivation of the surface integrals used for BEM formulation. The fact that BEM solutions require only the use of surface integrals for the calculation (or collocation) of matrix coefficients highlights immediately it's benefits and weaknesses (calculation of solutions at microphone points is more akin to a post-processing step: the coefficients of the matrix are used to solve a set of equations). Although the method only requires a mesh and subsequent calculation on surfaces (be they obstacles or source surfaces), this fact prevents the fluid medium itself from being treated as inhomogenous. From a physical perspective, this means that scattering due to flow regions and changing velocities are not considered. Sound sources due to similar effects are also not considered.

6.1.1 Theory

The following discussion will focus on the solution of the boundary integral for an external problem, given that it is indicative of the alternator problem. The reader is referred to [43, 16] for details of the derivation.

The formulation of the integral BEM equations begins with the use of Green's second identity. The second identity is derived from vector derivative identities and essentially provides a relationship between the volume integral of two variables and their derivatives in a domain to a corresponding surface integral, as shown in Equation 6.1. For the case of a direct BEM calculation, the two functions are the pressure, p, and the fundamental Green's solution, G.

$$\int_V \left(G\nabla^2 p - p\nabla^2 G\right) \mathrm{d}V = \int_S \left(G\frac{\delta p}{\delta n} - p\frac{\delta G}{\delta n}\right) \mathrm{d}S \tag{6.1}$$

It is of importance to note that solving for the pressure and pressure gradients restricts the solution to either an external, unbounded calculation or an internal , bounded calculation. Where the solution to both an internal and external problem is sought, an indirect approach is required, whereby the solution variables are the pressure change and the pressure gradient change across the boundary surface (e.g. a membrane). The following focuses on the solution to only an external domain for the application to the alternator problem.

For the application of BEM, two solutions are sought to the problem. The first solution, often referred to as the collocation step, assumes that the equations of interest are being solved on the surfaces itself. This is in order to solve the solution variables on the surface. The second solution assumes that the point representing the fundamental solution is located inside the domain of interest, an observer point. The calculation of these field point variables is often the less resource intensive calculation, given that it involves the solution of surface integrals related to individual field points through the Greens' functions. The collocation stage, on the other hand, assumes that, at boundaries, either the pressure or gradients are known. As an example, for a non vibrating wall, such as a scatterer, the boundary condition is specified as $\frac{\mathrm{d}p}{\mathrm{d}n} = 0$ thus leaving the pressure at the wall as an unknown.

An important principle in BEM is that of reciprocity, which stipulates that the Green's function is unchanged when source and listener locations are exchanged, and is proven in [35]. This essentially allows the source, mathematically defined by the Green's function, to be placed arbitrarily in the fluid, say at an observer's location, rather than on the surface where the source is acting. Solving for this location yields the solution at the observer.

Given that Equation 6.1 relates integration of a finite volume to a corresponding surface integration, by default the BEM equations need to be solved in an enclosed physical system. Although the problem is an external problem, the enclosure is assumed to be in the far field, $\lim_{r\to\infty}$. When assuming that the far-field sound has some particular form, the volume terms can be cancelled out. The assumption in BEM is that as the observer approaches infinity, the sound takes the form of the general Green's solution, i.e. a point monopole.

6.1.2 Limitations of Lowson's methodology and motivation of the BEM implementation

The Lowson's methodology and it's derivation has the inherent disadvantage of modelling sources that depend on only local conditions; these sources being solely dependant on the local force fluctuations. Essentially, the creation of each source is irrespective of others sources. Contrasting this to the boundary element method, the entire field is calculated in order to ensure boundary conditions at all surfaces are

satisfied. This has the inherent advantage of modelling not only simple, outward propagating waves (like the Lowson's technique), but also waves obstructed by surfaces.

The software package LMS Sysnoise is used in order to take into account the effect of the casing and other stationary obstructions on the propagation of the waves. The following section describes the implementation used, in addition to the initial validations carried out. As will be shown, a detailed alternator model was not constructed given an inherent inability of the BEM solver used to correctly model the boundary conditions required.

6.1.3 Implementation

The inability of the Synoise implementation of the Boundary Element method to model rotating and stationary surfaces in the one problem poses a need to couple a technique to the BEM method which allows the modelling of rotating sources. For the case of the rotating alternator, the proposal is to calculate the sound pressure and pressure gradients on a mesh surface lying between the rotating and stationary parts of the system. In effect, the proposal is similar to the technique implemented by Jeon and Lee, discussed in Section 2.5.

Given the nature of the problem, whereby propagation is calculated only outwards of the surfaces, the direct collocation method is suitable. The collocation method, in a general BEM formulation, has the undesirable property whereby either pressures or pressure gradients on selected surfaces can be defined; both cannot be restrained. For most applications, it is arguably inaccurate to define both variables, for example when the surfaces can be defined as either pressure boundary conditions or vibrating structures (or, as the case may be, a stationary solid structure). Such cases, given the nature of the BEM routine, assume that the source (with the singularity omitted) lies on the surface. For the intended case however, the surface is a 'virtual' surface. This virtual surface should be considered not as a boundary with defined source terms, but rather as a part of the fluid domain on which the domain results are known, the sources being at some arbitrary position inside of the enclosed virtual surface. The actual sources to the problem lie either within this virtual surface (the rotating sources from the Lowson's formulation) or outside of the virtual surface (static scattering surfaces, such as the casing), but not on the surface (the underlying assumption of the collocation method, which uses the Greens function kernel at the surface).

The collocation routine, given one of the variables, then solves for the other variable on the surface panels, as discussed in Section 6.1.1. The Sysnoise solver does allow the specification of an impedance on a surface (a ratio of pressure to pressure gradients), however the implementation is limited in that the impedance can only be specified as a constant value across the surface, rather than individually across mesh points. In general, only one of the variables can be specified with the other calculated assuming the source lies on the surface.

6.1.4 Validations

In order to show the potential problems stated earlier, calculations are carried out by using Lowson's method to calculate the propagation of a single unit magnitude dipole into the far field, up to an observer located 1 meter away. These results are then compared to an alternative, whereby the Lowson's technique is used to calculate the solution at a surface mesh at some distance from the source (between the source and the observer). Results on this surface mesh are then used in the BEM solver, and are propagated out into the far field. Ideally, a comparison between this solution and the solution consisting of only Lowson's method should yield the same results.

The following test method is carried out:

1. A simple dipole is specified in the Lowson's formulation of unit magnitude. The rms pressure

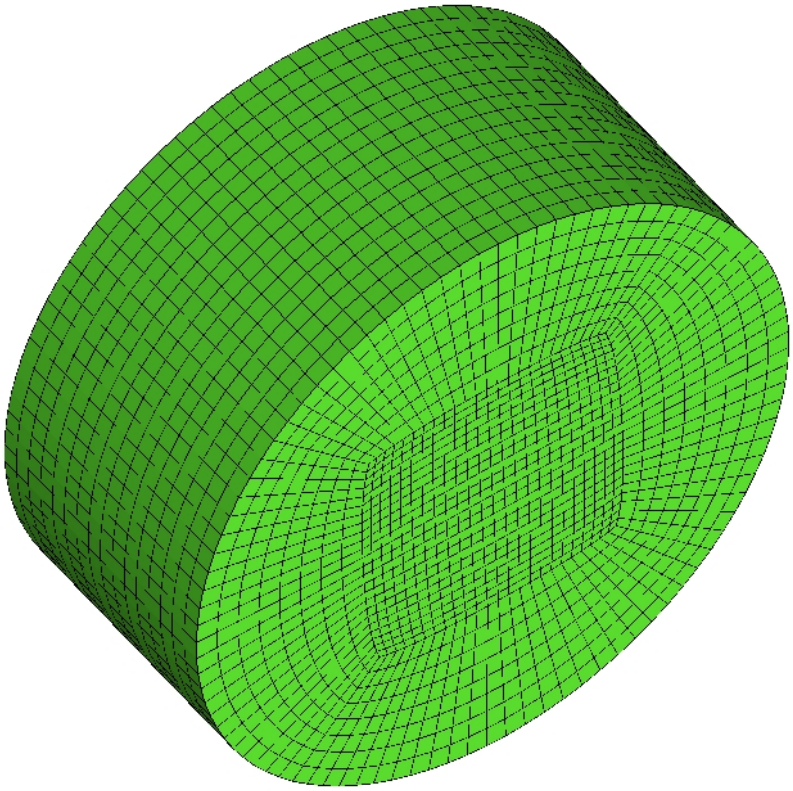

Figure 6.1: Grid used as interface between Lowson's solution and BEM input

distribution is calculated on a set of microphones acting normal to the dipole i.e. in the direction of the dipole's fluctuation.

2. The dipole is once again specified using Lowson's formulation, however in this case pressures and pressure gradients are determined on a surface mesh enclosing the dipole. Pressure gradients are determined by specifying an offset to all three coordinate locations of each mesh point and determining the gradient. The reference surface used is based of the surface separating the rotating and stationary domains in the actual generator. It's radius is approximately 0.05 meters, as is it's thickness. This cylinder mesh encloses the single dipole, positioned in the middle, and consists of 4,226 nodes, shown in Figure 6.1. Equation 2.5 is used to determine the normal velocity component. In addition to the reference surface, two other test surfaces are used based on the reference surface. These are essentially a surface scaled by a factor of 10 (each dimension is ten times larger) and a surface scaled by a factor of 0.1.

3. Two separate simulations for each surface location are carried out: one with the pressures calculated on the surface mesh as a boundary condition, the second using the velocity boundary conditions as the boundary condition.

6.1.5 Results

The comparison of results yields that a solution to the problem is seldom obtained which relates to the analytical (Lowson's) solution. For the case where pressures are specified on the surface, as in Figure 6.2, it is noted that in the BEM solution, the pressures correspond only at the interface, where they are specified as a boundary condition. For the cases where the interface is at $r = 0.05$ and $r = 0.005$ meters, it is evident that the gradients calculated in the collocation step are much larger than those obtained

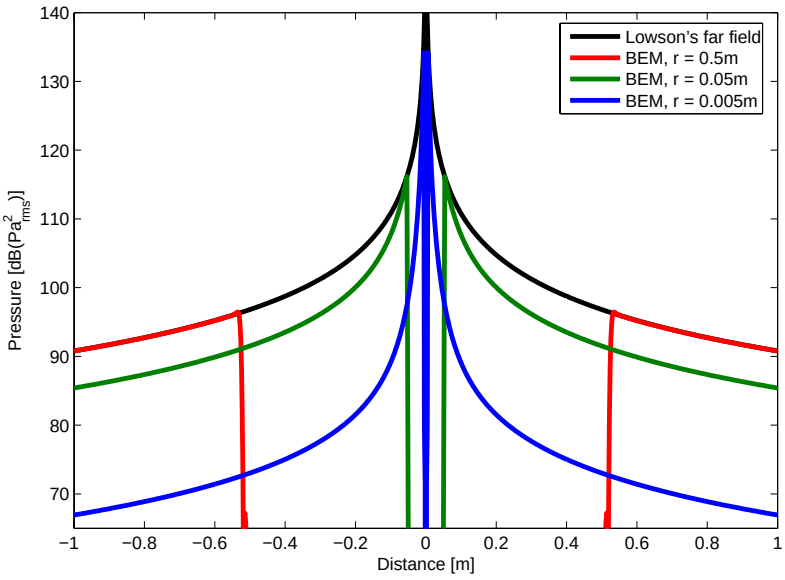

Figure 6.2: BEM solution using a pressure boundary condition as the coupling surface

analytically. This causes the far field solution to diverge from the analytical. The case where $r = 0.5$ meters shows results that are comparable to those of the analytical solution. This is due to the pressure gradients being weaker in the far field, thus ensuring that the pressure alone boundary condition is sufficient.

With the specification of pressure gradients, or as is the case with Sysnoise, velocity boundary conditions, yields the results indicated in Figure 6.3. The results, once again, vary with those of the analytical solution. Results inside of the virtual surface should be disregarded (for example, the results at $-0.5 < r < 0.5$ for the $r = 0.5$ interface). Unlike the case with the pressure as a boundary condition, here it is evident that gradients generally conform to the results of the analytical solution. The pressures on the other hand are incorrectly predicted at the interface during the collocation routine.

It is clear from these tests that a proper transfer between results using the code based on Lowsons equation and the LMS Sysnoise BEM solver is not possible given that, even for a stationary source case, far field solutions do not correspond. The BEM code used does not allow the specification of both pressures and pressure gradients, as may be required for such a virtual surface, the purpose of which is to simply restrict the acoustic variables at a certain location in space. This is generally the case with BEM methods, as typical boundary conditions seldom are virtual surfaces where results are already known. Rather, the specification of either pressure or pressure gradients corresponds to, physically, either some manner of controlled opening, or a vibrating structure. Neither is the case when the solution is being carried over from a separate computation.

6.2 Finite element methods

The software package COMSOL Multiphysics is used to construct a two dimensional model of the alternator. The package itself provides the user with an environment that allows solution of user-defined partial differential equations in addition to a set of standard physics based models, including fluid dynamics and acoustics models. The package provides three ways in constructing the partial differential set of equations defining the system of interest; in the case of this work, the coefficient form is used, where a general partial differential equation is defined through setting constants and/or variables as the

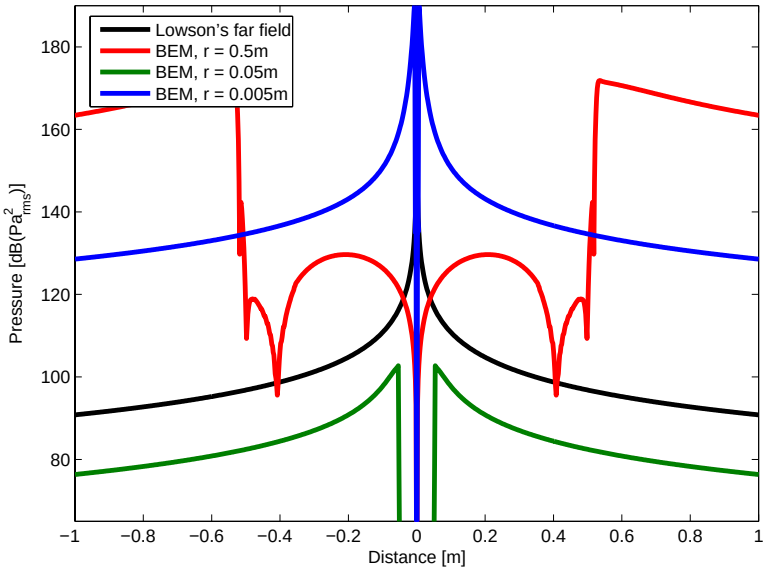

Figure 6.3: BEM solution using a velocity boundary condition as the coupling surface

coefficients. The general form of the PDE defined in the package is shown in Equation 6.2, with u being the variable of interest (e.g. the acoustic pressure, p).

$$e_a \frac{\partial^2 u}{\partial t^2} + d_a \frac{\partial u}{\partial t} + \nabla \cdot (-c\nabla u - \alpha u + \gamma) + \beta \cdot \nabla u + au = f \tag{6.2}$$

Additionally, two general boundary condition equations can be used, shown in Equations 6.3-6.4. For the acoustic problem, these can be respectively treated as the Neumann and Dirichlet boundary conditions, whereby the Neumann boundary condition can specify a gradient variable on the boundary, governed by the ∇u term, and the Dirichlet boundary condition simply sets the variable u to a value on the boundary.

$$\vec{n} \cdot (c\nabla u + \alpha u - \gamma) + qu = g - h^T \mu \tag{6.3}$$

$$hu = r \tag{6.4}$$

The following section will discuss how the FEM model was defined in COMSOL Multiphysics, highlighting the main characteristics of the model, including the modelling of the domain, modelling of interfaces between the moving and stationary domains, modelling of the surface boundary conditions (both source and obstructions) and modelling of the far-field in order to prevent non-physical reflections back into the domain. At each stage, validations will be shown. To conclude, the modelling of a simplified two-dimensional alternator will be shown, highlighting the physical significance of casing effects.

6.2.1 Governing equations for the acoustic problem

The modelling of the homogeneous wave equation shown in Equation 2.8 by substituting the required coefficients into Equation 6.2 would yield the coefficient set of $e_a = 1, c = a_0^2, \{d_a, \alpha, \gamma, \beta, f\} = 0$. For a stationary domain, this set is possible to model. However, COMSOL's implementation of the arbitrary Lagrangian-Euler description in order to model a moving mesh (required in the modelling of a rotor and stator domain) is unable to resolve the equations governing the domain that consist of higher (greater than first) order time derivatives. In order to overcome this limitation, the domain model was constructed using a two equation set, shown in Equation 6.5. The variable R in this case acts to define the first time

derivative of the acoustic pressure, thus allowing both equations to be solved in COMSOL's moving mesh formulation.

$$\begin{aligned} \tfrac{\partial R}{\partial t} - {c_0}^2\left(\tfrac{\partial^2 p}{\partial x^2} + \tfrac{\partial^2 p}{\partial y^2}\right) = 0 \\ \tfrac{\partial p}{\partial t} - R = 0 \end{aligned} \tag{6.5}$$

This set of equations is modelled in the form of Equation 6.2 in matrix form, whereby the coefficient set is defined in Equation 6.6 and the solution variable u is given in Equation 6.7.

$$\begin{aligned} d_a = \begin{bmatrix} 1 & 0 \\ 0 & 1 \end{bmatrix} \qquad c = \begin{bmatrix} 0 & {a_0}^2 \\ 0 & 0 \end{bmatrix} \qquad f = \begin{bmatrix} 0 \\ R \end{bmatrix} \\ e_a = a = \begin{bmatrix} 0 & 0 \\ 0 & 0 \end{bmatrix} \quad \alpha = \beta = \begin{bmatrix} 0\,0 & 0\,0 \\ 0\,0 & 0\,0 \end{bmatrix} \quad \gamma = \begin{bmatrix} 0 & 0 \\ 0 & 0 \end{bmatrix} \end{aligned} \tag{6.6}$$

$$u = \begin{bmatrix} R \\ p \end{bmatrix} \tag{6.7}$$

It is important to note that these variables are also used to define the boundary conditions, in particular the Neumann boundary condition (Equation 6.3). The Neumann boundary condition can thus be restated as show in Equation 6.8, where the standard Neumann condition has $q = 0$.

$$\begin{aligned} \vec{n} \cdot a_0^2 \nabla u = F \\ a_0^2 \tfrac{\partial}{\partial n} \begin{bmatrix} R \\ p \end{bmatrix} = F \end{aligned} \tag{6.8}$$

Validation of the two-equation set

The validation of the two-set model was carried out using the geometry shown in Figure 6.4. A small cylindrical surface is constructed in the middle of the fluid domain, whose radius is 1 meter. A pressure sinusoid boundary condition is applied to the surface in order to generate a monopole-like pressure distribution in the domain, both cosine and sine pressure waves are tested. The outer boundary has a non-reflective boundary condition applied, discussed in Section 6.2.3. This model is constructed using both the original wave equation, with it's second time derivative, in addition to the two-equation set. Given that the entire domain is stationary, the original wave equation can be modelled. The pressure solution is analysed at the blue point over time, and also along the red line at $t = 2.75 \times 10^{-3}$, a time step large enough to ensure that the entire wave has propagated to the outer boundary. The comparison of the two results is shown in Figures 6.5-6.6.

As can be seen in Figure 6.5, both the standard and advection (2-set) forms of the wave equation generate the same pressure distribution on the line analysed. Figure 6.6 shows similar positive results in the temporal domain. In this case however, the impulsive nature of the cosine pressure source causes a small perturbation at $t \approx 0.7 \times 10^{-3}$ seconds.

Figure 6.7 shows a comparison of the spatial solution across the line to the Green's solution of both the three-dimensional wave equation (Equation 2.15) and the two-dimensional wave equation (Equation 2.16). The solutions essentially dictate the rate at which the pressure reduces away from the source. The comparison here is made by using the first peak in the advection equation solution as the reference point, and setting the two analytical solutions at this reference point. Quite clearly, the pressure drop calculated using the two-set advection form of the wave equation relates well to that predicted by the 2D Green's equation. The 3D pressure drop is more rapid compared to that of the 2D solution due to the dispersion of energy in three dimensions, instead of only two.

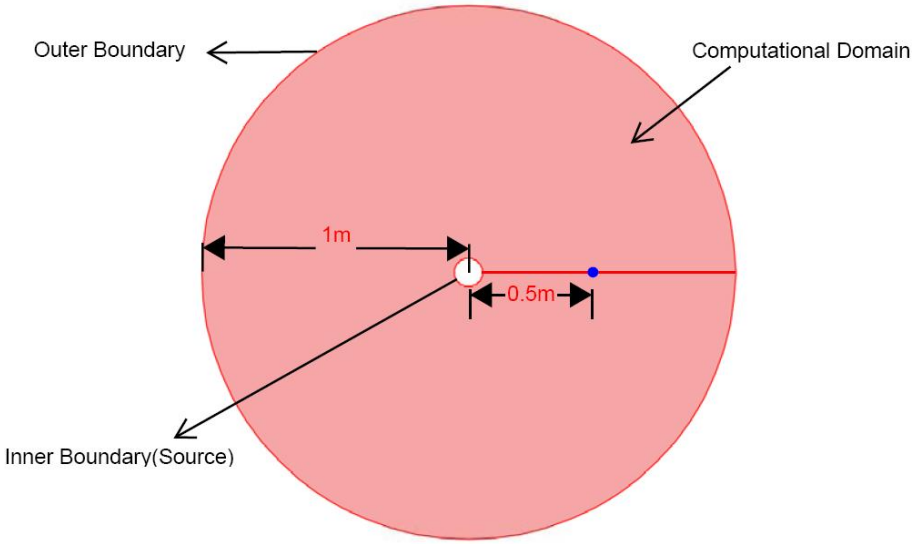

Figure 6.4: Model used for the two-equation set validation

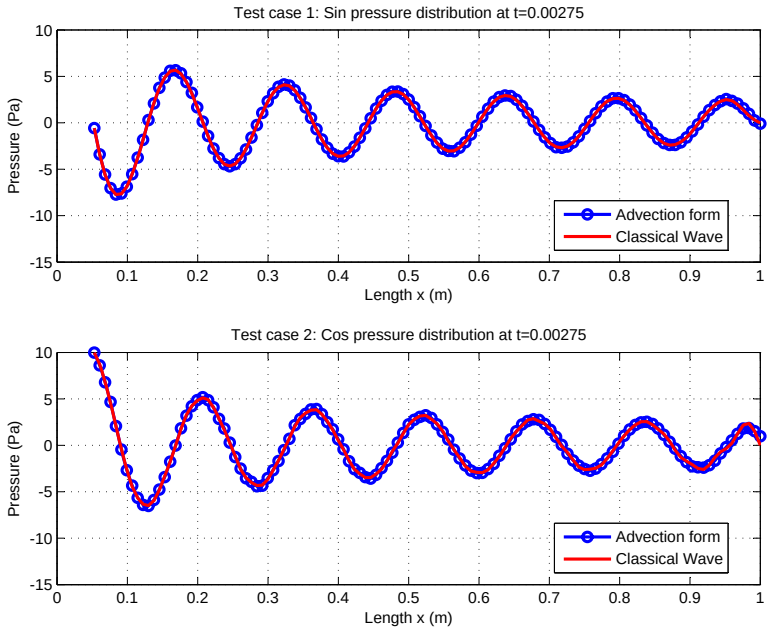

Figure 6.5: Comparison between one-set and two-set wave equation along line at $t = 2.75 \times 10^{-3}$

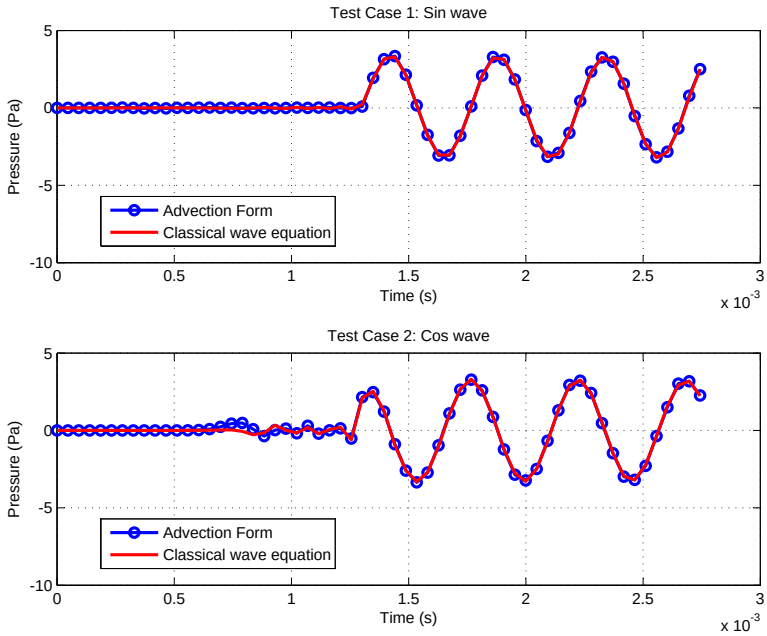

Figure 6.6: Comparison between one-set and two-set wave equation at point over time

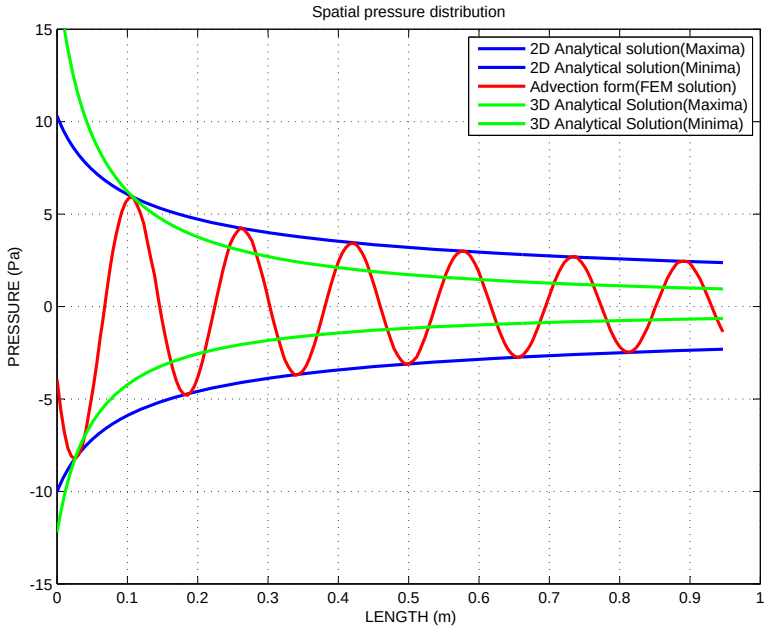

Figure 6.7: Comparison of the two-set wave equation to the analytical spatial pressure drop of the 2D and 3D wave equation.

6.2.2 Source surface boundary condition

In order to close the solution of the acoustic problem, appropriate boundary conditions need to be imposed on the key surfaces. Interface and far field boundary conditions will be discussed in the following sections, the following discussion will highlight the choice of appropriate surface boundary conditions. For surfaces that act as only obstacles, and themselves are not sources of sound, setting a hard wall boundary conditions suffices, whereby $\frac{\partial p}{\partial n} = 0$. This states simply that the pressure gradient across and normal to the surface is zero; physically, sound is perfectly reflected.

For the surfaces that act as both aeroacoustic sound source as well as reflector (the clawpole surfaces, for example), the Dirichlet pressure boundary condition does not suffice. In forcing the pressure distribution to be that of the source at the source surface, an incorrect modelling occurs when waves approach that surface. Rather, the waves reflected back onto the surface will either be weaker or stronger in order to maintain the surface pressure as defined by the boundary condition.

Conversely, the Neumann boundary condition can be used to define, for the case where $\frac{\partial p}{\partial n} = 0$, a hard wall, and for other values some given vibration, as $\frac{\partial p}{\partial n}$ is proportional to a hard-wall velocity boundary condition [38]. In doing so, the source becomes both a sound producer in addition to obstruction. In order to define some pressure input as both a hard wall vibration as well as pressure fluctuating source, it is proposed in this work that a simple convection-type equation be used to define the Neumann boundary condition. Essentially, this equation defines that any temporal variation of pressure be propagated outward from (and normal to) the surface at the speed of sound, shown in Equation 6.9. Given the tendency of the outgoing wave to travel perpendicular from the surface (from the $\frac{\partial p}{\partial n}$ term), the required dipole shape should also be evident.

$$\frac{\partial p}{\partial t} - a_0 \frac{\partial p}{\partial n} = 0 \tag{6.9}$$

Validation of the surface source boundary condition

In order to determine whether the surface acts well as both a sound generator as well as a sound obstacle, three test cases were carried out using two models, shown in Figure 6.8. The main tests were carried out using the above described Neumann boundary condition, calculated from the convection-like equation. Boundary condition data on the source surface is shown in Tables 6.1-6.2. The three cases tested are as follows:

1. Using model (a) from Figure 6.8, the forcing on the surface is defined using the Dirichlet boundary condition from Table 6.2. The surface enclosing the domain to the right is modelled as a hard wall, with $\frac{\partial p}{\partial n} = 0$. All other surfaces are modelled using the non-reflective boundary condition defined in Section 6.2.3.

2. Also using model (a), this time the forcing is defined using the Neumann boundary condition from Table 6.2. In this instance, the surface acts as both a hard-wall but also as a source.

3. Using model (b), the left geometry is modelled as a hard-wall while the right geometry is modelled as the third case; a Neumann boundary condition. In this instance, the left geometry acts as only an obstruction.

The results of all three cases are analysed at a point behind the left geometry. The comparison of test case 2 and 3 is of most interest here; both cases should yield similar results. In case 2, the reference point should not receive any direct signal from the source, but rather receive the reflected signal from the right wall in addition to the diffracted signal due to the surface. In case 3, the hard-wall of model

Variable	Value	Description
a_0	343 m/s	Speed of sound
p_0	20 Pa	Pressure amplitude
ω	47123 rad/s	Frequency
Δt	$4e^{-5}$ s	Time step
t_{fin}	0.00675 s	Total time

Table 6.1: Model data for Neumann with surface pressure condition

Test case	Pressure (Dirichlet)	Time derivative	Surface Pressure BC
1	$p = p_0 sin(\omega t)$	$p_t = p_0 \omega cos(\omega t)$	$p_n = -a_0 p_0 \omega cos(\omega t)$
2	$p = p_0 cos(\omega t)$	$p_t = -p_0 \omega sin(\omega t)$	$p_n = a_0 p_0 \omega sin(\omega t)$

Table 6.2: Source boundary condition with surface pressure condition

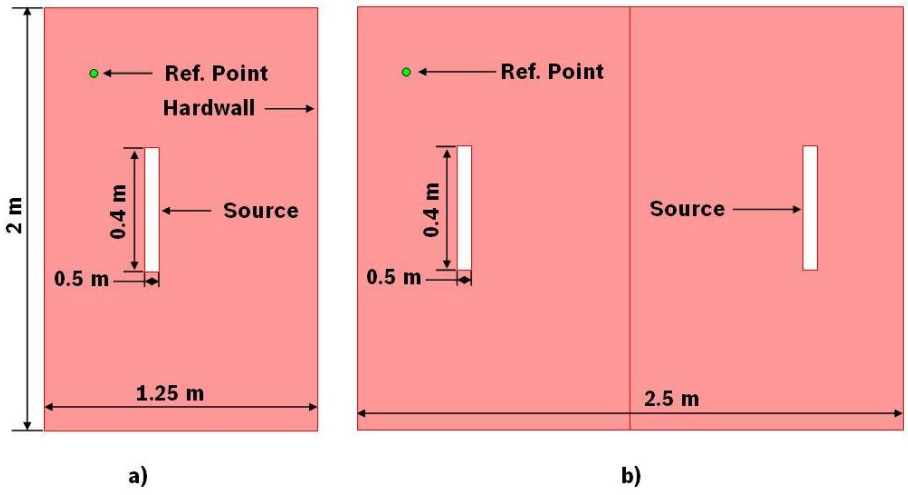

Figure 6.8: Two models used to test surface source boundary condition. Model (a), as a single source panel with hard wall at the right most of the domain and model (b), as a source at right with obstruction at left of the domain

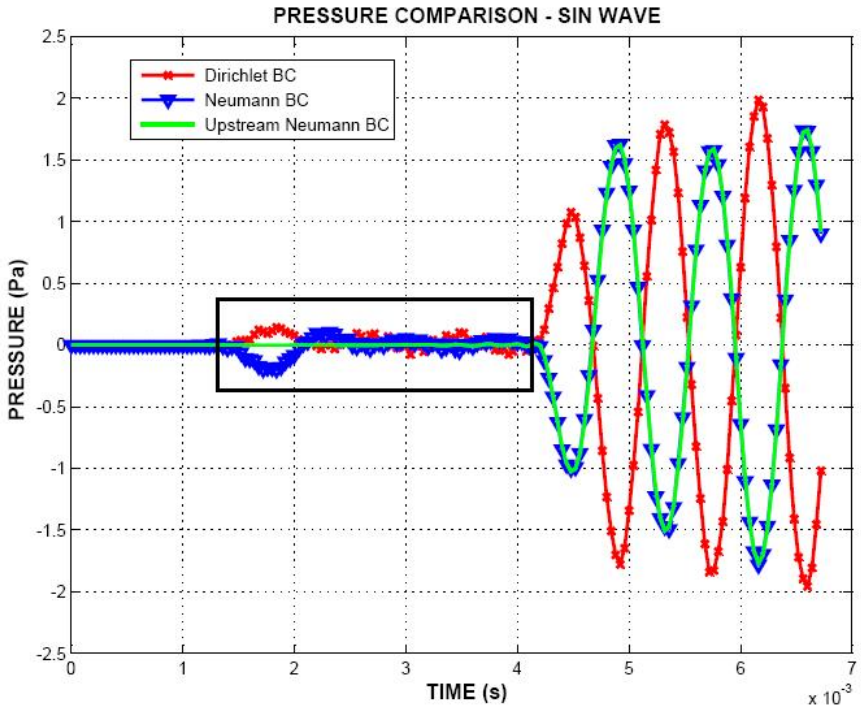

Figure 6.9: Source surface boundary condition using a sine pressure forcing

(a) is replaced by using an acoustic mirror source. The reference point should receive a signal due to the diffraction of the right surface.

For each test case, both a sine and cosine signal are used. Results of the sine wave as the forcing are shown in Figure 6.9. As can be seen, case 2 and case 3 share identical results, showing that the Neumann boundary condition acts as both a sound source as well as diffractor. The Dirichlet boundary condition is somewhat different; firstly, it is 90˚opposed, due to the negative sign of the Neumann boundary condition (Table 6.2). At early time steps, shown as a box in Figure 6.9, time perturbations are noted that are not existent for case 3 (the upstream Neumann boundary condition). These are due to small numerical errors, whereby the reference point receives some of the initial signal from the source. Given that the upstream Neumann boundary condition case has its source far from the reference point, it is not noted there.

Figure 6.10 shows the results of the cosine case. Once again, case 2 and 3 show identical results at higher time steps, implying the ability for the Neumann boundary condition to treat the surface as both source as well as diffractor. At very early time steps, much like in the sine case, a direct signal occurs at the reference point. This however disappears at higher time steps.

6.2.3 Non-reflective boundary condition

The definition of the outer boundary of the numeric domain poses difficulties as the outer boundary does not have a constant value which may be assigned through the use of a Neumann (pressure gradient) or Dirichlet boundary condition. Figure 6.11 shows the effects of setting the outer boundary to a constant value; in this example, the outer boundary is set by $\frac{\partial p}{\partial n} = 0$. The model used is identical to that used in Section 6.2.1. A significant difference is noted just prior to wave contact with the outer boundary and that just after contact. In order for the given boundary condition to be valid (in this case, zero pressure gradient at the boundary), a wave must enter into the domain, thus causing a numerical reflection. A similar effect would also be present if the outer boundary was defined with a set pressure (Dirichlet) boundary condition; for the wave equation to be valid in the entire domain, in addition to a set pressure

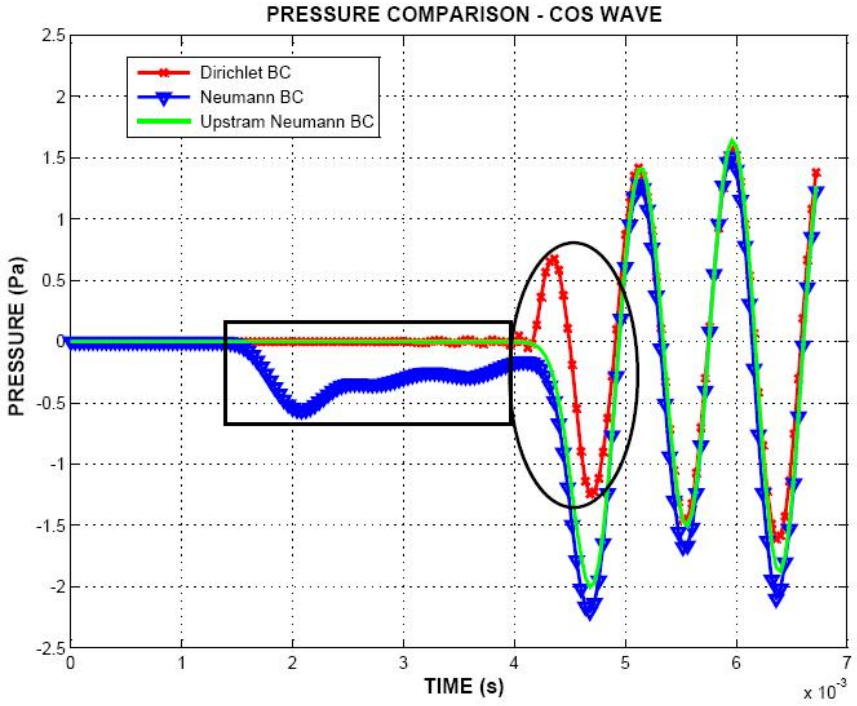

Figure 6.10: Source surface boundary condition using a cosine pressure forcing

on the boundary, a second wave must enter into the domain to allow both wave equation and boundary condition to be respected.

In order to allow a wave in the domain to exit the domain unhindered, the outer boundary must be set with an equation that allows any incoming wave to convect outwards, and this at the speed of the sound, a_0. The equation used for this boundary condition is shown in Equation 6.10. Through this equation, any wave approaching the outer boundary will exit that boundary normal to it's surface at the speed of sound. Note that the equation is similar to Equation 6.9; whereas in the surface source equation it acts as a source propagating sound waves into the domain, in this instance the equations acts like a sink, taking sound energy out of the domain.

$$\frac{\partial p}{\partial t} + a_0 \frac{\partial p}{\partial n} = 0 \tag{6.10}$$

Validation of the non-reflective boundary condition

In order to validate the effect of the non-reflective boundary condition, the comparison shown in Figure 6.11 is repeated, in this case using the non-reflective boundary condition shown in Equation 6.10. Figure 6.12 shows that the pressure distribution before and after wave contact with the outer boundary condition remains identical; the wave is successfully convected outwards without any reflections coming back into the domain.

6.2.4 Interface between rotating and stationary domain

In order to be able to model multiple domains, an interface is required between the two domains to allow coupling. Considering an inner rotor domain and an outer stator domain, the model must be capable of producing sound waves in the rotor, propagating them outwards into the stator, and possibly reflecting the waves back into the rotor. Considering the two domains separately, essentially the interface must act as both a source, when a wave is entering, and a sink, when the wave is leaving. In order to model this, the

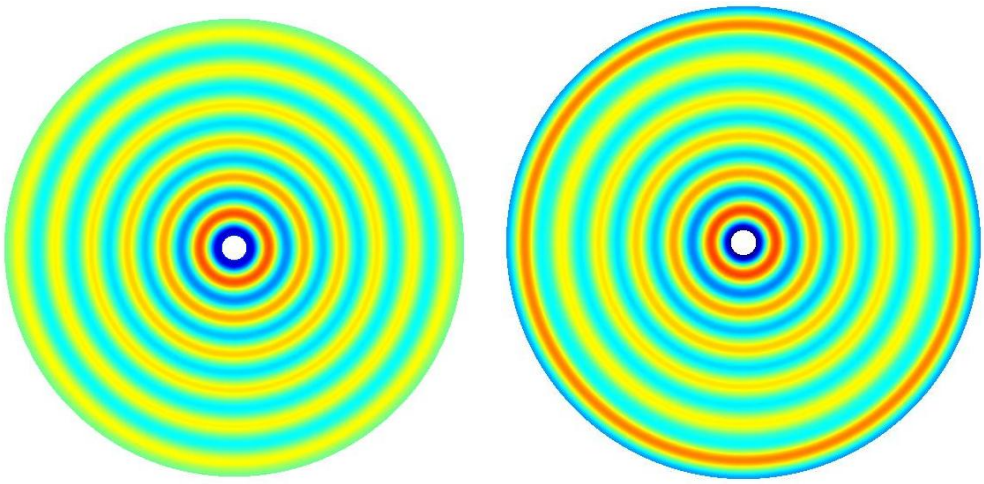

(a) Sound pressure distribution prior to wave contact with outer boundary ($t = 2.697 \times 10^{-3}$ s)

(b) Sound pressure distribution after wave contact with outer boundary ($t = 3.116 \times 10^{-3}$ s)

Figure 6.11: Influence of hard wall boundary condition ($\frac{\partial p}{\partial n} = 0$) on sound propagation and reflection in the domain

familiar equations used for the sound source and far-field boundary conditions are modified. Two pressure variables are required in this instance; one for the stationary domain and one for the rotating domain. The resulting equation is shown in Equation 6.11, where the subscripts r and s denote respectively the two domains, rotor and stator.

$$a_0 \frac{\partial p_r}{\partial n} = -(\frac{\partial p_r}{\partial t} - \frac{\partial p_s}{\partial t}) + a_0 \frac{\partial p_s}{\partial n} \tag{6.11}$$

As a further restriction to the interface variables, it is required that $p_r = p_s$ in order to ensure that there is no jump in the pressure variable across the interface.

Validation of domain interface

Figure 6.13 shows the domain used for the validation of the interface boundary condition. Both inner and outer domains are stationary. A source is placed off-centre in the inner domain with a sinusoidal pressure boundary condition, further details of the main features of the model are given in Table 6.3. The far-field boundary condition, described in Section 6.2.3, is used on the outer boundary of the outer domain. The two obstructions in the outer domain are modelled as hard walls.

Variable	Value	Description
a_0	343 m/s	Speed of sound
p_0	20 Pa	Pressure amplitude
ω	47123 rad/s	Frequency
Δt	$2.75e^{-5}$ s	Time step
t_{fin}	0.00465 s	Total time

Table 6.3: Model data for test case A

Results of the analysis are shown in a series of figures outlining the propagation of the wave away from the source, Figures 6.14(a)-6.14(d). Figures 6.14(a) and 6.14(b) shows the propagation of the wave exiting the inner domain and entering the outer domain. Quite clearly, there are no spurious reflections from the interface, and the wave maintains it's monopole shape caused by the circular source geometry. Figures 6.14(c) and 6.14(d) demonstrate reflected waves from the obstructions re-entering the

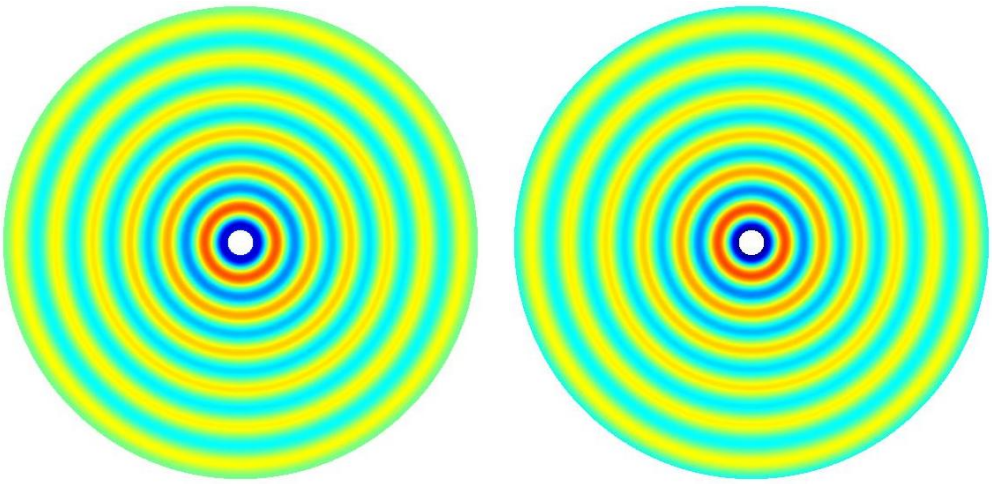

(a) Sound pressure distribution prior to wave contact with outer boundary ($t = 2.697 \times 10^{-3}$)

(b) Sound pressure distribution after wave contact with outer boundary ($t = 4.045 \times 10^{-3}$)

Figure 6.12: Influence of non-reflective boundary condition ($\frac{\partial p}{\partial t} + a_0 \frac{\partial p}{\partial n} = 0$) on sound propagation and reflection in the domain

inner domain correctly. These last two time steps also demonstrate the ability of the far-field boundary condition to prevent spurious reflections back into the domain.

6.2.5 Modelling of a simplified fan blade and clawpole without a casing

For the modelling of a simplified alternator, two two-dimensional models were created to separately model the fan blade geometry and clawpole geometry. The goal here is to model both main rotor sources, the fan blade and the rotor. Given that, in a three dimensional domain, these components are axially separated, in the two-dimensional domain they can only be modelled separately. The goal here, in any case, is to validate the ability of the FEM model to model the rotating modes predicted by the Lowson's code. Both geometries have been modelled based off the three-dimensional geometries introduced in Section 5. In each instance, an active surface, shown in Figures 6.15(a) and 6.15(b) as a blue marking, is given a sinusoidal forcing. The forcing is a standard sinusoidal forcing. For each of the surfaces (12 fan blades and 8 clawpoles), the forcing is phase shifted. This phase shift is implemented given the results of Section 5 and general fan theory; it is known that for rotor/stator interactions and a symmetrical rotor with n surfaces, comparison of the forcing of the n symmetrical surfaces will show a time phase shift given by Equation 6.12, where ω is the rotational speed.

$$t_s = \frac{2\pi}{\omega n} \tag{6.12}$$

The time shift can therefore be implemented into the individual forcing on each of the blades through Equation 6.13, where Q is the forcing order applied to that surface. As will be shown shortly, a fundamental forcing using an 8th order will be used for both fan and clawpole cases, with the clawpole cases also undergoing an additional 48th order to simulate the aerodynamic interactions between the clawpole surfaces and the stator holes.

$$p = sin(Q\,\omega(t + i * t_s)) \quad \text{for} \quad i = 0 \,\text{to}\, N - 1 \tag{6.13}$$

As discussed in Section 6.2.2, the Neumann boundary condition will be utilised for the forcing of the active surfaces in both geometries. This is given as Equation 6.14.

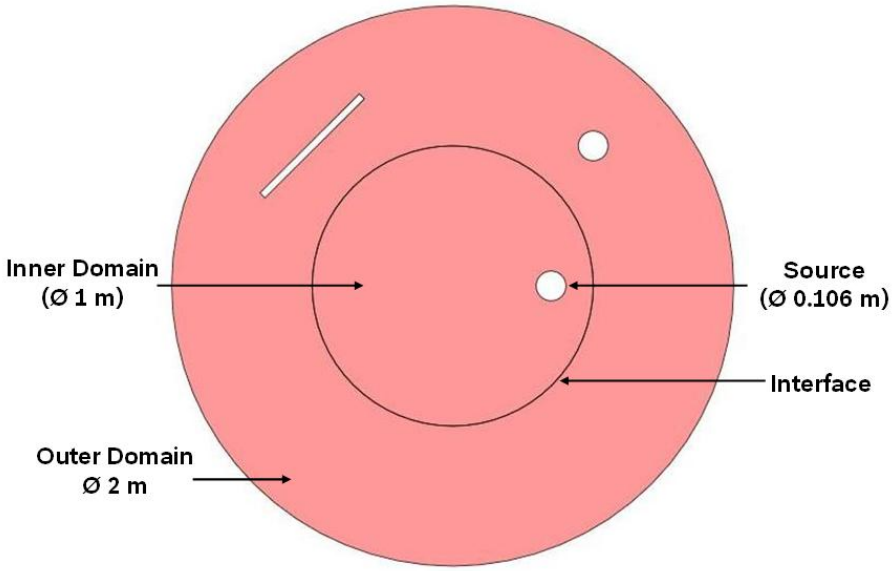

Figure 6.13: Geometry used for validating the interface boundary condition

$$p_n \;=\; -Q\, a_0\, \omega\, cos(Q\, \omega(t + i * t_s)) \quad \text{for} \quad i \;=\; 0 \,\text{to}\, N-1 \tag{6.14}$$

Fan blade geometry

For the fan blade geometry (Figure 6.15(a)), 12 thin rectangular elements are aligned symmetrically in the rotating domain. The active surface is the leading edge of the blades, whereby the rotation direction is anti-clockwise. The applied forcing, using the Neumann boundary condition, is given in Equation 6.15. All other fan surfaces are modelled with the Neumann condition for a hard-wall, $\frac{\partial p}{\partial n} = 0$. The interface between the rotor and stator is modelled as discussed in Section 6.2.4, while the non-reflective boundary condition discussed in Section 6.2.3 is used for the outer boundary of the stationary domain. A rotational speed of 10,000 rpm anti-clockwise is assumed for the rotating domain.

$$p_n \;=\; -8\, a_0\, \omega\, cos(8\, \omega(t + i * t_s)) \quad \text{for} \quad i \;=\; 0 \,\text{to}\, 11 \tag{6.15}$$

Figures 6.16(a)-6.16(b) show a comparison of results from the FEM model at a time step once convergence is achieved, compared to an identical simulation carried out using Lowson's model. A calculation using Lowson's model is carried out, with microphones placed on a plane enclosing all 12 sources, after which an inverse Fourier transform is carried out in order to obtain a temporal pressure distribution. The forcing is identical in both cases. Although the scales show difference between the two results (note that a different scale has been used for both results), the spinning mode is accurately modelled using the FEM model, and appears to have identical characteristics. Both results show 4 very distinct high and low pressure spirals emitting from the location of the blades. The local pressure distribution repeats every 3rd blade for both solutions. This is equivalent to a 90°phase separation. The 8th order forcing applied to the individual fan blades repeats every $\frac{360}{8} = 45°$, while the spacing between each fan blade is $\frac{360}{12} = 30°$. Thus, every 90°there occurs a repetition in the local pressure.

Figure 6.17 shows a comparison of the pressure spectra determined at one-point in the field, 0.35 m away from the centre of rotation (shown in the casing model in Figure 6.20), for both the FEM and Lowson's model. The first harmonic of the blade passing frequency is modelled quite well, with less than a 2 dB difference. Higher harmonics are predicted much higher in the Lowson's code, whereas the FEM code shows that higher harmonics are within the broadband regime, due in this instance to numerical

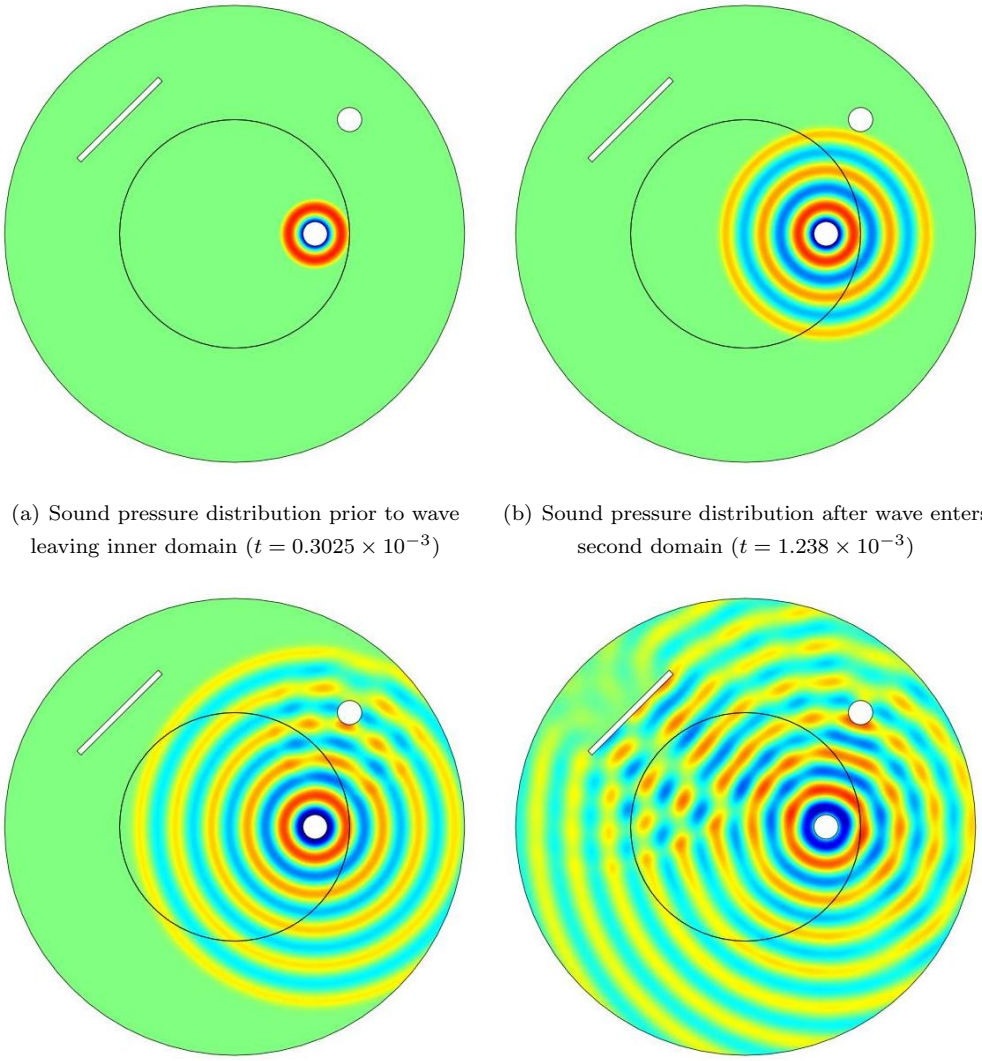

(a) Sound pressure distribution prior to wave leaving inner domain ($t = 0.3025 \times 10^{-3}$)

(b) Sound pressure distribution after wave enters second domain ($t = 1.238 \times 10^{-3}$)

(c) Sound pressure distribution after wave reflects back into inner domain after contacting first obstruction ($t = 2.2 \times 10^{-3}$)

(d) Sound pressure distribution after wave reflects back into inner domain after contacting second obstruction ($t = 4.565 \times 10^{-3}$)

Figure 6.14: Pressure distribution from a wave in a coupled two-domain problem using a convection-type domain interface

errors (for the perfectly periodic case, broadband values between harmonics should be much lower than the harmonics). This can also be due to the inversion of results from the time domain in the FEM solution.

Clawpole geometry

The clawpole geometry (Figure 6.15(b)) consists of a large structure with eight protruding elements close to the rotating/stationary domain interface. For the clawpole model, the active surface is the most radially outward surface of the eight clawpole fingers, shown in Figure 6.15(b) as the blue active surfaces. All other surfaces use the hard-wall Neumann boundary condition, $\frac{\partial p}{\partial n} = 0$. Once again, an anti-clockwise motion is assumed, rotating at 10,000 rpm. Interface boundary conditions and far-field boundary conditions are used from discussions in Sections 6.2.3 and 6.2.4. The forcing on the active surfaces comprises of both an eighth order fluctuation in addition to the 48th fluctuation, designed to model the aerodynamic interactions between the rotor surfaces and the 48 casing holes. Equation 6.16 defines the forcing in terms of the surface source Neumann boundary condition, defined in Section 6.2.2.

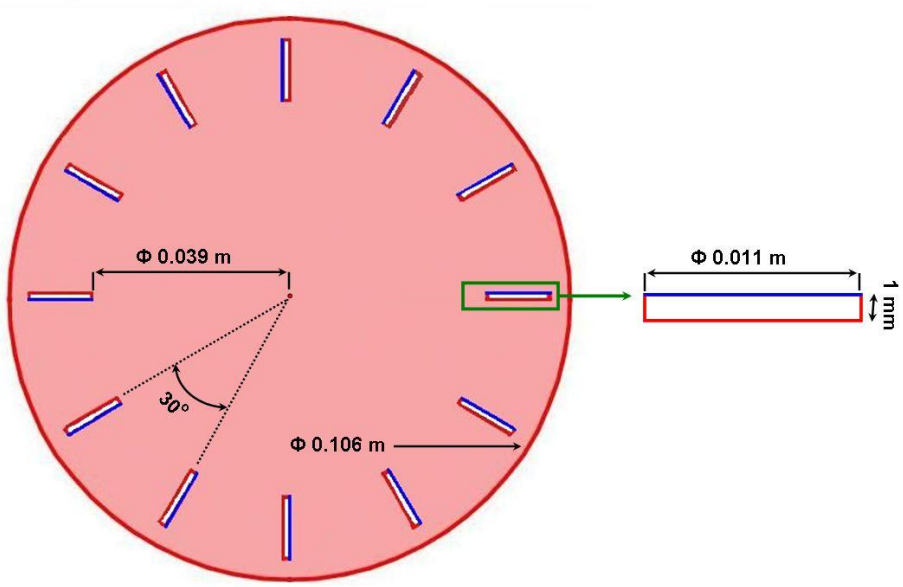

(a) Fan blade geometry

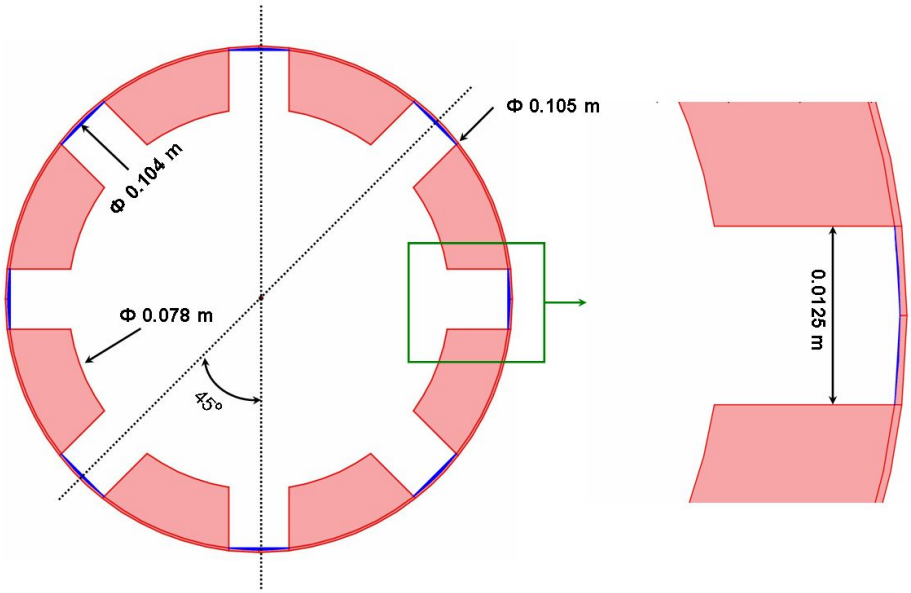

(b) Clawpole geometry

Figure 6.15: Geometry used for the modelling of rotating fan blades and rotating clawpole surfaces, whereby the direction of rotation is anti-clockwise

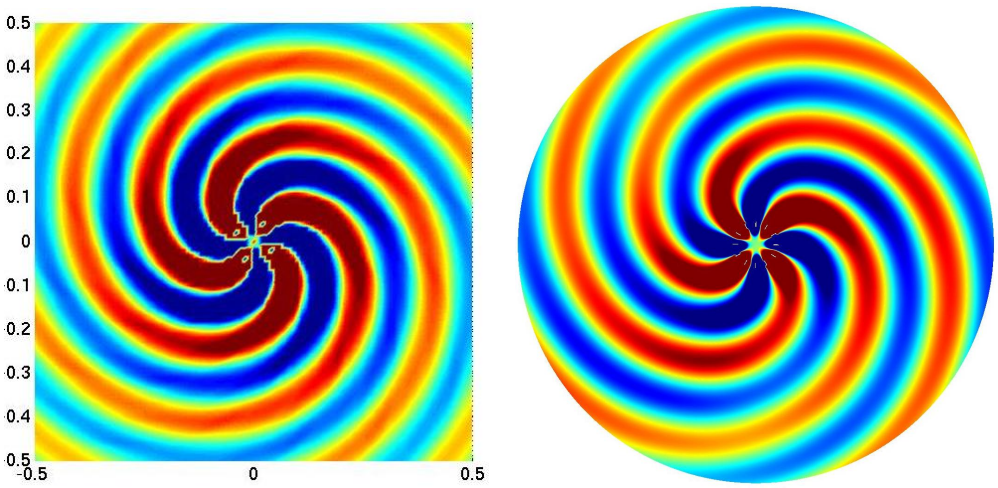

(a) Lowson's solution: Pressure range = ±0.5 Pa (b) FEM solution: Pressure range = ±0.005 Pa

Figure 6.16: Comparison of pressure distributions from the two fan-blade solutions at a single time-step

$$p_n = -8\,a_0\,\omega\,[cos(8\,\omega(t + i * t_s) + 6\,cos(48\,\omega(t + i * t_s))] \quad \text{for} \quad i = 0\,\text{to}\,7 \tag{6.16}$$

Figures 6.18(a) to 6.18(b) show the comparison between the Lowson solution and the FEM solution of the two problems, whereby the Lowson's solution is determined across a plane perpendicular to the axis of rotation and containing all sources. As with the fan blade case, spirals are once again seen in the field, in this case eight. Each surface in this case (unlike the fan case) emits an in-phase spiral, the reasoning being that both the 8th and 48th order forcing is always in phase for each surface. The 48th order fluctuation on the other hand appears to emit much like a monopole, in the sense that it has a recognisable centre at the centre of rotation. In any case, the fundamental pressure distribution at a time step appears to be similar for both cases.

Figure 6.19 shows a point comparison of the sound pressure spectra determined from both the Lowson's solution in addition to the FEM solution. Quite evidently, the main spectral peaks are noticeable in both solutions, where both a fundamental 8th order in addition to the higher order (48th) and sidebands are apparent. In any case, significant energy is missing from the Lowson's solution at these main orders; this is due to Lowson's solution, based on the three-dimension wave equation, dissipating the wave in three dimensions as opposed to two, as in the FEM solution. This yields a more rapid reduction in pressure across a distance. It is unclear why a similar effect has not been noted for the fan model case.

6.2.6 Influence of the casing in the clawpole model on sound propagation

In order to determine the effects of the casing on sound propagation, the clawpole model is used. In the alternator model used throughout this work, it is expected that the casing has the greatest effect on the clawpole noise sources, as indeed the fan blade operates in a region where, in the stator, a gap exists between the casing and endshield that can allow sound waves to propagate away. The clawpole model shown in Figure 6.15(b) is used as the rotor, while the casing geometry, once again modelled from the original three-dimensional alternator geometry, is shown in Figure 6.20. The geometry consists of 48 holes, at a distance of 0.5 mm to the stator/rotor interface and 1.5 mm to the outer surface of the clawpole. The surfaces representing the hole edges are modelled using the hard-wall Neumann boundary condition. A new solution of the clawpole model without stator is carried out again, given that smaller time steps are requided for the simulation with the stator. The reasoning for this is the reduction of the element size near the interface in order to accommodate for the casing holes.

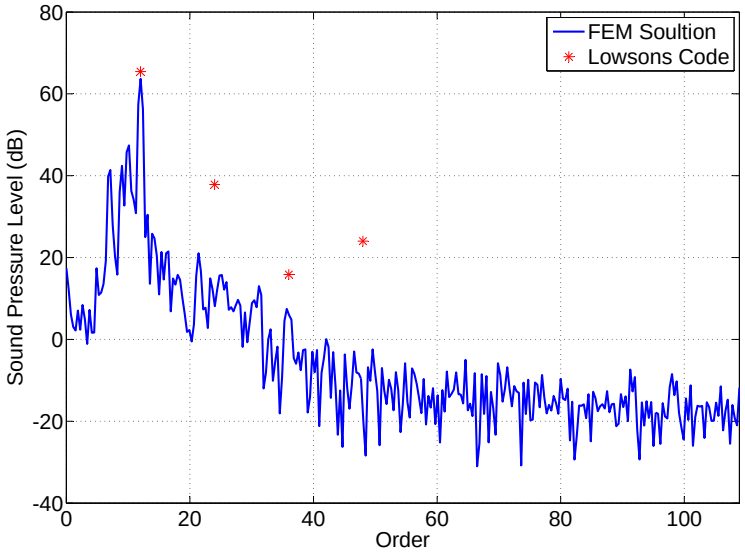

Figure 6.17: Comparison of pressure spectra of the fan-blade solution between the FEM solution and Lowson's code

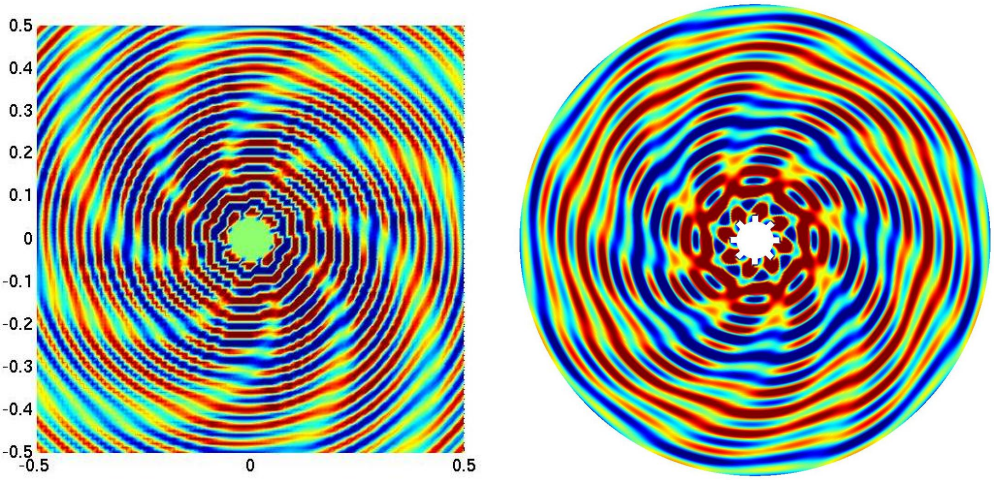

(a) Lowson's solution: Pressure range = ±0.2 Pa (b) FEM solution: Pressure range = ±0.5 Pa

Figure 6.18: Comparison of pressure distributions from the two clawpole solutions at a single time-step

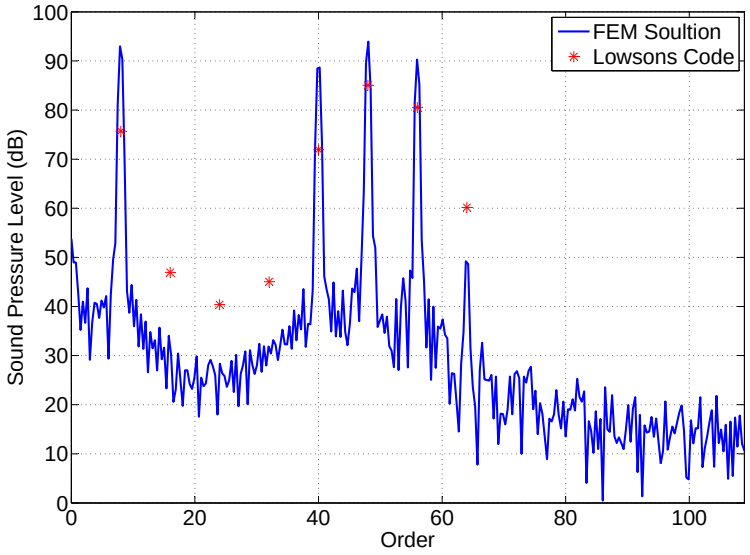

Figure 6.19: Comparison of pressure spectra for the clawpole solution between the FEM solution and Lowson's code

A spectral comparison of the Lowson's and FEM solutions is shown in Figure 6.21 at the reference point shown in Figure 6.20. Quite clearly, the solutions show almost identical sound power levels at the 8th, 48th and 56th orders. The wave length of the sound at these higher orders is of the order of the geometry, where the 56th order at 10,000 rpm has a wavelength of 3.7 cm. Quite clearly, every 8th order at the higher orders (above the 60th) show an effect of the casing. The waves reflecting between the casing and rotor are modulated onto the 8th symmetry, although these effects are in any case not as strong as the first two sidebands (the 40th and 56th orders). It is also evident that an influence is present at the 40th order, approximately 10 dB. Integrating the sound spectra gives the total sound pressure level at the observation point; the influence of the additional spectral orders increases the total sound pressure level by 3.6 dB.

6.3 Summary

The inability to model a two way coupling between the spinning modes generated in Lowson's equation and the boundary element solver Sysnoise was from the outset not possible. A one way coupling was investigated, whereby several solutions (near, mid and far field) where generated from the Lowson's calculation on an arbitrary cylindrical surface. Both Neumann and Dirichlet boundary conditions were investigated in Sysnoise; propagation into the far-field showed results dissimilar to those calculated solely using Lowson's formulation, which agrees well with the analytical solution. In the case of the Dirichlet boundary condition, pressure at the interface of the two solutions agreed, but the disagreement of the pressure gradients at the interface yielded inaccurate predictions of the spatial pressure drop. Conversely, the use of a Neumann boundary condition yielded accurate pressure gradients at the interfaces, but the inability to set the pressure also yielded poor results. An accurate coupling between the Lowson's code and LMS Sysnoise was thus not achievable.

The FEM model created allowed a two-way coupling between rotating and stationary domains, albeit in only two-dimensions. The software was incapable of modelling the wave equation in it's standard form due to the moving mesh ALE (Arbitrary Lagrangian Euler) description's inability of modelling

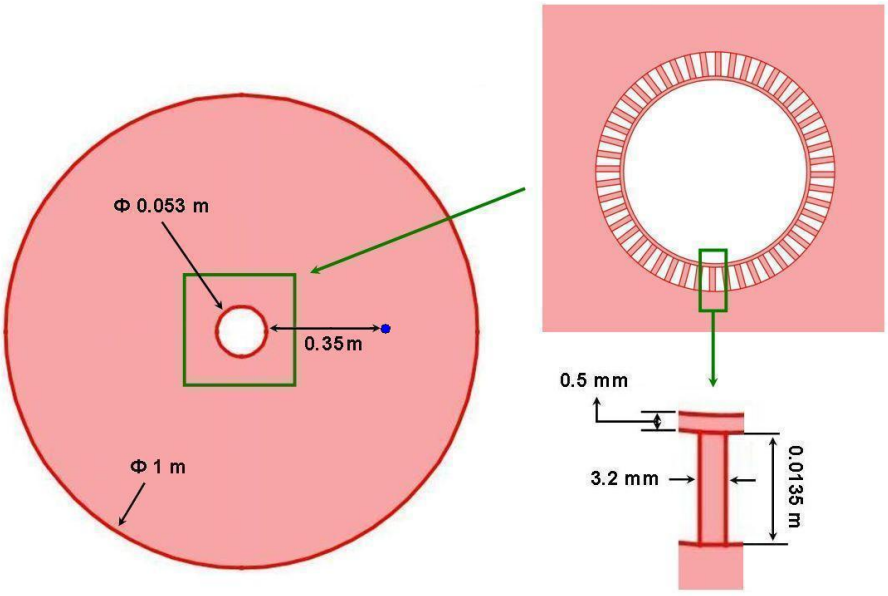

Figure 6.20: Stator casing geometry

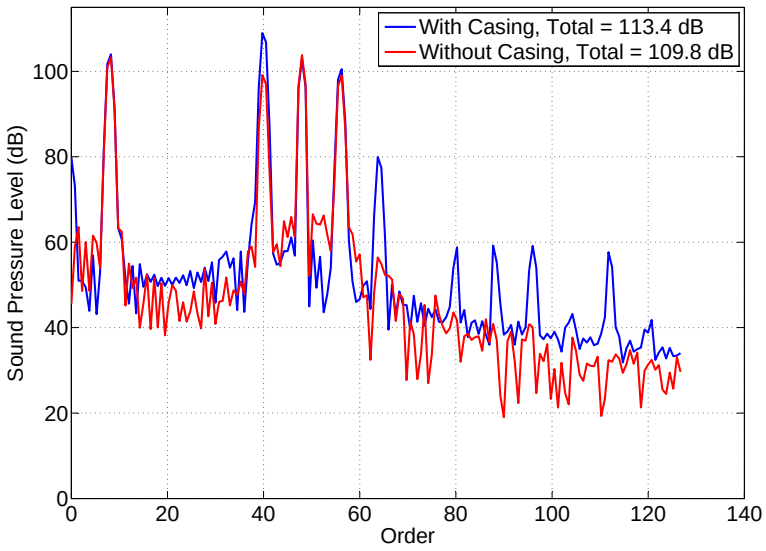

Figure 6.21: Comparison of pressure spectra with and without casing

equations with a second order time derivative. A two equation formulation of the wave equation was thus derived, and successfully validated. Additionally, formulations were derived for a far-field boundary condition, a wall-source boundary condition and the interface between the rotating and stationary domain, all successfully validated using trial models. Rotating models were constructed (both fan blade and clawpole) and both were shown to generate spinning modes very similar to those generated using Lowson's formulation, albeit at different magnitudes. Finally, a trial was made to test for casing effects, and it was found that the casing influences high orders (wavelengths at least smaller than the geometry), in particular above the 60th, and the total sound pressure at a point by 3.6 dB. The findings however show only the influences at a point and to a degree, given the symmetry of the domain used, in the field. The influences the casing has on three-dimensional propagation are uncertain.

Considering the findings of Section 5, it is evident that the non-inclusion of a stationary casing has indeed little effect on total sound generated. This is noted given that simulated and measured total-energy from all orders is within 1.5 dB(A). The fact that some of the higher orders were poorly calculated in Section 5 (the 56th order of the reference model, and the 40th order of the clawpole-alone model) imply from the finding of this section that there is some energy produced at higher orders due specifically to the reflections of waves between the casing and rotor.

Chapter 7

Conclusions and recommendations

The scopes and objectives laid out at the beginning of this work were used as broad guidelines to develop methods that can be used in the development of alternators to ensure aerodynamic noise specifications are met. Particular focus was placed on tonal noise and it's prediction, as tonal noise components are often the most critical due to the concentration of sound energy at single frequencies and orders; such phenomena are often perceived as annoying. In the experimental work, it was shown that this tonal noise has a particularly strong contribution to total sound energy produced; the removal of upstream ribs, which was shown to influence individual orders by up to 30 dB(A), contributed up to 6 dB(A) in total noise; an increase in sound energy by a factor of 4. This not only showed the importance tonality plays in the total sound energy produced, but also highlighted the necessity to analyse the transient pressure variations in the system. With this, the need for transient CFD computations for source input calculation was grounded.

Through an analysis of the literature relating to current aeroacoustic calculation practices, a decision on the methodology to use throughout this work was made. Out of the three types of aerodynamic noise sources (the monopole, the dipole and the quadrupole), the current body of knowledge showed that for industrial, small machines operating at sub sonic speeds, the dipole source was the prevalent one. For the case of the alternator, this was shown to be the case experimentally, with sound power level increase over speed shown to be proportional to the sixth power of the Mach number/rotational speed; the relationship expected from predominantly dipole sources.

These findings set the requirements for the numerical models; the models had to take into account system transients in addition to the modelling of dipole sources. Through further literature studies, the Ffowcs-Williams and Hawkings based Lowson's formulation was found to meet these requirements; a tool in Matlab was subsequently developed to allow the use of CFD transient surface pressure data as an input for the Lowson's based solver. The solver was designed such that it could allow user defined source resolutions to be assigned, with sound pressure and power calculated at user specified frequencies and at user specified microphone positions.

Key modifications were however also required for the solver. In order to model the reflective plane from the test bench, a mirror source calculation was implemented. This involved the mirroring of all source terms under the reflective plate. Validation showed that the model was correct, in that, as expected from the theory, it generated symmetrical results about the reflective plane and, more importantly, produced zero pressure gradients across the reflective plane, this being the well known hard wall Neumann boundary condition. The second modification involved altering the form of the dipole sources, such that over time, they would only act in the surface normal direction. This was in order to overcome sound being generated behind solid sound emitting surfaces. Again, validation showed this modification to work correctly.

Initial measurements taken had indicated main noise generating mechanisms in the system. Through

modification of key geometries, it was experimentally shown that the main fan blade generated noise mechanism was the upstream ribs. Transient CFD studies showed that in this region, the velocity field was altered significantly. For the rotating fan blades, this had the effect of changing the pressure distributions on the fan blades in this local region. These pressure fluctuations were shown both experimentally and analytically to be significant contributors to the sound generated.

For the case of the clawpole fingers, the main sound generating mechanism was shown to be the interactions occurring between the clawpole fingers and the outer casing holes. For the standard geometrical case, the noise generated was concentrated at higher orders due to the high frequency pressure fluctuations on the clawpole fingers from the 48 casing holes. Experimentally, it was additionally shown that by modifying these holes (closing selective holes), significant increases in lower order noise was achieved. Although the clawpoles were constructed of 8 symmetrical surfaces, it was shown numerically in addition to experimentally that they produced noise peaks at every fourth order. This was found to be due to asymmetrical pressure distributions on consecutive fingers due to the different relative positions of downstream fan blades, of which there were 12.

Two cases were numerically calculated and compared to experimental results; a reference alternator with upstream ribs, clawpole fingers and fan blades, and a similar configuration without fan blades. It was found that the dominant frequencies were generally predicted within 6 dB(A) of experimental results. Total sound power levels were not predicted as accurately, with up to 10 dB(A) differences noted. This was due solely to the inability to model broadband noise; the assumption of periodicity allowed calculation of tonal noise at every 4th and 8th orders (for the reference and no-fan case respectively). Broadband noise sources between orders could not be calculated.

Considering however the energetic summation of the sound at the calculated and measured orders, the comparison was significantly better. Differences between the numerical model and experimentally measured sound power were within 1.5 dB(A). Furthermore, comparison of the relationship between the sound pressure values between individual microphones showed very well agreement; the loudest and quietest microphones were well predicted, as was the relationship between consecutive microphones. Detailed computational analysis, using a fine mesh of microphones, indicated an asymmetry in the sound propagation which was also noted experimentally. This asymmetry, through the use of the numerical tool developed, was shown to be due to the reflective plane.

In order to assess the ability for the procedure to function in a development framework, a complex alternator geometry based on a current product was computed and compared to experimentally using 10 alternator samples. Once again, total sound energy was incorrectly predicted due to the inability to model broadband noise components. In contrast however, the energetic summation of calculated and measured orders agreed very well with measured data; the numerical result was within the results obtained from the 10 samples. Orders were also calculated very well, in particular the fan orders and the relationship with one another (in this instance, the asymmetry of the fan blades yielded a wider range of frequency contributions). Errors at the higher orders, in addition to the 16th, were apparent, however this was due to the CFD models simplified stator which assumed 48 symmetrical equally sized holes; in reality, these holes are not equally sized, and thus shift some sound energy to lower orders.

Finally, work was carried out to study the effects of the casing. A coupling between the BEM solver LMS Sysnoise and the Lowsons code was implemented, in order to propagate the spinning modes generated in the Lowson's solution outwards past the casing. This propagation was however not possible given the inability to specify both pressure and pressure gradients on the interface. In specifying one or the other, poor correlations were shown with an analytical solution of a fundamental source.

The FEM implementation in COMSOL was somewhat more successful. Although not coupled to the CFD solution and only a 2D model, casing effects were investigated. Models were created which allowed the solution of the wave equation in a multi-domain (rotating and stationary) while preventing

reflections at the far field boundary. Boundary conditions for the sources were developed, which allowed sound wave creation but also sound scattering. Comparison between a geometry with a casing and one without showed some influence. A 3.6 dB increase in total sound pressure was noted, due predominantly to increased orders above the 60th; additional orders appeared to be created due to casing effects. The 8th, 48th and 56th orders remained unchanged, while a 10 dB increase in the 40th order was noted.

In summary, the tools developed within the framework of this project have achieved the purpose that was set out. The tool has been used on an actual alternator geometry being developed and has predicted most orders well, in addition to predicting very well the energetic sum of orders. Total energy is poorly predicted due to the lack of broadband noise modelling. The ability to separate the sources at will and determine their noise contributions thus allows localisation of noise sources. Finally, the model based on Lowson's equation works quickly; there is no need for added meshing, CFD results need only be imported. The transient CFD calculations, due to their resource requirements, are the main hurdle in obtaining quick turnover of results. Simulation time for the two cases shown was between 4 to 6 months using up to 20 CPU cores. The full model test using the product geometry indicated that larger time steps also yielded good results, with converged calculations taking 14 days using 16 CPU cores. Studies however were not conducted in order to determine whether the larger time steps influenced the poor accuracy of the higher sound orders (in addition to the geometrical assumption of symmetry at the stator).

Recommendations for further work, given the findings of this work, include the modelling of broadband noise sources. Technically, this is also possible using the Lowson's formulation with the use of more extensive time domain results (several rotations). The assumption of a strongly periodic system would need to be relaxed. Additionally, further turbulence models would need to be investigated in order to accurately resolve small scale turbulence. Through the modelling of such sources, and relaxing the assumption of periodicity, it is expected that total sound power values would be higher, closer to those measured.

Further validation using industrial systems is also recommended. The one validation carried out showed very promising results, however it also indicated the importance of modelling small scale asymmetries (such as those in the stator winding) for the proper modelling of clawpole generated orders. This work is currently continuing, and it is hoped that a set of validations for complex geometries will be possible in the near future.

The Lowson's implementation thus far only calculated rotating sources, ignoring pressure fluctuations occurring on the static surfaces. For the fan blade and stator interaction, this appears to have little bearing given the very good prediction of fan blade generated sound in both the simplified case, in addition to the complex alternator model. Analysis of CFD results also showed pressure fluctuation on the fan blade to be greater than that on upstream and downstream stationary components, however clawpole fluctuations were of similar magnitude to the stationary surface pressure fluctuations. The proximity of the clawpole to the casing produces surface pressure variations on the stationary surfaces; the ability to determine their influence on total sound energy and the individual orders needs to be investigated, however given the Mach number components in Lowson's equation, it is expected that the stationary surfaces with comparable pressure fluctuations will have a smaller contribution to sound than the rotating surfaces.

Finally, the FEM based work carried out showed some influence from scattering effects on the casing, with an increase in total sound pressure at a point of 3.5 dB. Orders above the 60th were shown to be influenced, in addition to the 40th order. Given that the trials were carried out in a two-dimensional domain, influences on total sound energy were difficult to determine. Further studies into three-dimensional effects of a casing in the alternator are therefore recommended.

Bibliography

[1] DIN 45635: Geräuschmessungen an Maschinen Luftschallemsission, Hüllflächen-Verfahren Rahmenverfahren für 3 Genauigkeitsklassen, April 1984.

[2] Commission Directive 2007/34/EC, June 2007. Commission Directive in the Official Journal of the European Union.

[3] ISO 3745-1977. Acoustics - Determination of sound power levels of noise sources - Precision methods for anechoic and semi-anechoic rooms, 1977.

[4] ISO 3745-2003. Akustik - Bestimmung der Schallleistungspegel von Geräuschquellen aus Schalldruckmessungen - Verfahren der Genauigkeitsklasse 1 für reflexionsarme Räume und Halbräume, 1977.

[5] J.D. Anderson. *Computational Fluid Dynamics The Basics with Applications*. McGraw-Hill, 1995.

[6] J.E. Bardina, P.G. Huang, and T.J. Coakley. Turbulence modeling validation, testing and development. *NASA Technical Memorandum*, April 1997.

[7] R. Biswas and R.C. Strawn. Tetrahedral and hexahedral mesh adaption for CFD problems. *Applied Numerical Mathematics*, 26:135–151, 1998.

[8] M. Boltezar, M. Mesaric, and A. Kuhelj. The influence of uneven blade spacing on the SPL and noise spectra radiated from radial fans. *Journal of Sound and Vibration*, 216(4):697–711, October 1998.

[9] K. S. Brentner and F. Farassat. An analytical comparison of the acoustic analogy and Kirchhoff formulation for moving surfaces. *AIAA Journal*, 36:1379–1386, 1998.

[10] K. S. Brentner and F. Farassat. Modeling aerodynamically generated sound of helicopter rotors. *Progress in Aerospace Sciences*, 39(2-3):83–120, February-April 2003.

[11] K. G. Bürger. Alternators, 1999.

[12] K. G. Bürger, H. P. Gröter, H. J. Lutz, F. Meyer, and W. Schleuter. Alternators in automotive applications state of the art and development trends (translation of german text. In *Nebenaggregate im Fahrzeug*, Essen, October 1994. Haus der Technik.

[13] R.C. Chanaud. Aerodynamic sound from centrifugal-fan rotors. *The Journal of the Acoustical Society of America*, 37(6):969–974, June 1965.

[14] H.L. Choi and D.J. Lee. Development of the numerical method for calculating sound radiation from a rotating dipole source in an opened thin duct. *Journal of Sound and Vibration*, 295:739–752, 2006.

[15] N. Curle. The influence of solid boundaries upon aerodynamic sound. In *Proceedings of the Royal Society of London. Series A, Mathematical and Physical Sciences*, pages 505–514, September 1955.

[16] O. Estorff, J.P. Coyette, and J.L. Migeot. *Boundary Elements in Acoustics Advances and Applications*, chapter 1: Governing formulations of the BEM in acoustics. WIT Press, Southampton, Boston, 2000.

[17] M. V. Goldstein. *Aeroacoustics*. McGraw-Hill, 1976.

[18] L. Gutin. On the sound field of a rotating propeller. Technical Memorandum 1195, National Advisory Committee for Aeronautics, 1948.

[19] G. Hübner. Sound power related to normalized meteorological conditions. In *Internoise 99*, 1999.

[20] W.H. Jeon and J.H. Cho. Numerical analysis of unsteady flow field and flow noise of a fan system. In *The 33rd International Congress and Exposition on Noise Control Engineering*, Prague, August 2004. Internoise2004.

[21] W.H. Jeon and D.J. Lee. A numerical study on the flow and sound fields of centrifugal impeller located near a wedge. *Journal of Sound and Vibration*, 266:785–804, 2003.

[22] M. J. Lighthill. On sound generated aerodynamically. i. General theory. In *Proceedings of the Royal Society of London. Series A, Mathematical and Physical Sciences*, pages 564–587, March 1952.

[23] M. J. Lighthill. Sound generated aerodynamically. In *Proceedings of the Royal Society of London. Series A, Mathematical and Physical Sciences*, pages 147–182, November 1961.

[24] Z. Liu and D.L. Hill. Issues surrounding multiple frames of reference models for turbo compressor applications. In *Proceedings, 15th International Compressor Engineering Conference*, 2000.

[25] M. V. Lowson. The sound field for singularities in motion. *Proceedings of the Royal Society of London*, 286:559–572, 1965.

[26] M. V. Lowson. Theoretical analysis of compressor noise. *The Journal of the Acoustical Society of America*, 47(1):371–385, 1970.

[27] H. J. Lutz. Noise test bench for measuring sound power from vehicle alternators to ISO 3745-1977 (corresponds to DIN 45635). Technical report, Robert Bosch GmbH, 1996.

[28] R.C. Mellin and G. Sovran. Controlling the tonal characteristics of the aerodynamic noise generated by fan rotors. *The Journal of Basic Engineering*, 92(1):143–154, 1970.

[29] W. Neise. Fan noise - Generation mechanisms and control methods. In *Internoise '88*, pages 767–776, 1988.

[30] W. Neise. Review of fan noise generation mechanisms and control methods. In *International INCE Symposium*, pages 45–56, 1992.

[31] W. Neise. Aerodynamische Geräusche von Ventilatoren Erzeugungsmechanismen und Minderungsmaßnahmen. In *Tagung des Haus der Technik e.V. Aeroakustik - Schallerzeugung, Geräuschminderung, akustische Messungen und Berechnungen in Strömungen*, pages 45–56, Stuttgart, November 2004.

[32] C. Ofria. Alternator stator. `http://www.familycar.com/Classroom/Images/Charging_Stator.jpg`. Accessed 14.05.2009.

[33] M. Ozgoren. Flow structure in the downstream of square and circular cylinders. *Flow Measurement and Instrumentation*, 17:225–235, 2006.

[34] J. Park, J. Kwon, and B. Ahn. Numerical simulations of flow noise in automotive hvac systems. In *JSAE Annual COngress*, pages 21–24. JSAE, 2004.

[35] A.D. Pierce. *Acoustics An Introduction to Its Physical Principles and Applications*. McGraw-Hill, New York, 1981.

[36] A. Powell. Similarity and turbulent jet noise. *The Journal of the Acoustical Society of America*, 31(6):812–813, June 1959.

[37] M. Roger. Noise from moving surfaces. Lecture Series, March 2004. in Advances in Aeroacoustics and Applications Lecture Series.

[38] A.F. Seybert. *Boundary Element Acoustics Fundamentals and Computer Codes*, chapter 1: Fundamentals of linear acoustics. WIT Press, Southampton, Boston, 2000.

[39] H.K. Versteeg and W. Malalasekera. *An introduction to Computational Fluid Dynamics The Finite Volume Method*. Pearson Education, Essex, 1995.

[40] M. Wasko and M. Fischer. The numerical investigation of flow-induced sound generation from a simplified alternator geometry. In *Fortschritte der Akustik DAGA '05*, pages 623–624, 2005.

[41] E.W. Weisstein. Green's function. MathWorld–A Wolfram Web Resource, 2004. http://mathworld.wolfram.com/GreensFunction.html.

[42] J. E. Ffowcs Williams and D. L. Hawkings. Sound generation by turbulence and surfaces in arbitrary motion. *Philosophical Transactions for the Royal Society of London. Series A, Mathematical and Physical Sciences*, 264(1151):321–342, May 1969.

[43] T.W. Wu. *Boundary Element Acoustics Fundamentals and Computer Codes*, chapter 2: The Helmholtz integral equation. WIT Press, Southampton, Boston, 2000.

[44] T.W. Wu. *Boundary Element Acoustics Fundamentals and Computer Codes*, chapter 3: Two-dimensional problems. WIT Press, Southampton, Boston, 2000.